5-2016

Design and Implementation of an Integrated Biosensor Platform for Lab-on-a-Chip Diabetic Care Systems

Khandaker Abdullah Al Mamun
University of Tennessee - Knoxville, kmamun@utk.edu

To the Graduate Council:

I am submitting herewith a dissertation written by Khandaker Abdullah Al Mamun entitled "Design and Implementation of an Integrated Biosensor Platform for Lab-on-a-Chip Diabetic Care Systems." I have examined the final electronic copy of this dissertation for form and content and recommend that it be accepted in partial fulfillment of the requirements for the degree of Doctor of Philosophy, with a major in Electrical Engineering.

Nicole McFarlane, Major Professor

We have read this dissertation and recommend its acceptance:

Jayne Wu, Nathanael Paul, Syed K. Islam, Ramki Kalyanaraman

Accepted for the Council:
Dixie L. Thompson

Vice Provost and Dean of the Graduate School

(Original signatures are on file with official student records.)

Design and Implementation of an Integrated Biosensor Platform for Lab-on-a-Chip Diabetic Care Systems

A Dissertation Presented for the
Doctor of Philosophy
Degree
The University of Tennessee, Knoxville

Khandaker Abdullah Al Mamun
May 2016

Dedicated to

My parents & grandparents
Nasiruddin Khandaker
Umme Sumiya Nargis
Mir. Yousuf Ali
Hafizuddin Khandaker

My in-laws
Begum Nurun Nahar
Rezaul Hossain
Nur Hossain

My wife & son
Ruhina Tasmin
Khandaker Mosabbir Rayed

My sisters
Nahid Akhter Shanta
Tanzina Akhter Ratna

ACKNOWLEDGEMENT

First of all, I would like to express my gratitude to Dr. Nicole McFarlane for giving me the opportunity to work with her during my Ph.D. program. This work would not have been possible without her guidance and continuous support. I am thankful to Dr. Jayne Wu, Dr. Nathanael Paul, Dr. Syed K. Islam, and Dr. Ramki Kalyanaraman for serving on my Ph.D. committee and for their valuable suggestions.

I would like to thank Center for Nanophase Material Sciences (CNMS), Oak Ridge National Laboratory for providing the cleanroom facility used in this work through a user project. Especially, I would like to thank Mr. Dale Hensley, Mr. Ivan Kravchenko, Ms. Bernedata Srijanto, and Mr. Dayrl Briggs for their extensive help during microfabrication. I would also like to thank Dr. Nathanael Paul and Mr. Nate Henry for all the brainstorming sessions in our project. I thank my colleagues Jinlong Gu, Habib Ullah Habib, Yongchao Yu, Chirag K. Tailor, Ifana Mahbub, Farhan Quaiyum, Md. Sakib Hasan, Sanjib Das, Haochen Cui, Terence Randall, Taeho Oh, Tan Yang, Jeremy Langford, Peixing Liu, Mohsen Judy, Kelly Griffin, and Arnab Baruah for all the great times in Lab.

I sincerely thank my wife Doctor Ruhina Tasmin for always being beside me and motivate me throughout the doctoral program. I thank my parents, sisters, son, in-laws and grandparents for always be supportive. I want to thank my mother especially for her great patience and allow me break into her electronic appliances. I still remember the days in my grandpa's house when I first successfully made a car with a shoe box, discovered coils in a radio, experimented with dry cells and dc motors. My father who is a civil engineer took me to his work sites and instilled in me a love for engineering. I would also like to thank my teachers in college who showed me the beauty of math.

ABSTRACT

Recent advances in semiconductor processing and microfabrication techniques allow the implementation of complex microstructures in a single platform or lab on chip. These devices require fewer samples, allow lightweight implementation, and offer high sensitivities. However, the use of these microstructures place stringent performance constraints on sensor readout architecture. In glucose sensing for diabetic patients, portable handheld devices are common, and have demonstrated significant performance improvement over the last decade. Fluctuations in glucose levels with patient physiological conditions are highly unpredictable and glucose monitors often require complex control algorithms along with dynamic physiological data. Recent research has focused on long term implantation of the sensor system. Glucose sensors combined with sensor readout, insulin bolus control algorithm, and insulin infusion devices can function as an artificial pancreas. However, challenges remain in integrated glucose sensing which include degradation of electrode sensitivity at the microscale, integration of the electrodes with low power low noise readout electronics, and correlation of fluctuations in glucose levels with other physiological data. This work develops 1) a low power and compact glucose monitoring system and 2) a low power single chip solution for real time physiological feedback in an artificial pancreas system.

First, glucose sensor sensitivity and robustness is improved using robust vertically aligned carbon nanofiber (VACNF) microelectrodes. Electrode architectures have been optimized, modeled and verified with physiologically relevant glucose levels.

Second, novel potentiostat topologies based on a difference-differential common gate input pair transimpedance amplifier and low-power voltage controlled oscillators have been proposed, mathematically modeled and implemented in a 0.18μm [micrometer] complementary metal oxide semiconductor (CMOS) process. Potentiostat circuits are widely used as the readout electronics in enzymatic electrochemical sensors. The integrated

potentiostat with VACNF microelectrodes achieves competitive performance at low power and requires reduced chip space.

Third, a low power instrumentation solution consisting of a programmable charge amplifier, an analog feature extractor and a control algorithm has been proposed and implemented to enable continuous physiological data extraction of bowel sounds using a single chip. Abdominal sounds can aid correlation of meal events to glucose levels. The developed integrated sensing systems represent a significant advancement in artificial pancreas systems.

TABLE OF CONTENTS

LIST OF TABLES

LIST OF FIGURES

CHAPTER 1
INTRODUCTION AND MOTIVATION

1.1 Introduction

According to the American Diabetic Association in 2012, 9.3% of the entire American population (29.1 million) have suffered from diabetes and diabetes related complications. A majority of the population is still undiagnosed (8.1 million). Diabetes is the 7th leading cause of death in the US [1]. In 2012, 11.8 million seniors had diabetes, while 86 million people showed pre-diabetic symptoms. Each year, approximately 1.4 million people in the US are diagnosed with diabetes. The preventive treatment of diabetes disease costs at approximately $14,000 annually.

Diabetics may suffer episodes of hypo or hyperglycemia, which are blood glucose levels below or above the healthy plasma glucose limit of 80-130mg/dL (4.44-7.22mM) before a meal or less than 180mg/dL (10mM) an hour after a meal [1]. Hypoglycemia can induce comas and lead to death if left untreated, while hyperglycemia can lead to acute health complications. Cardiovascular problems, neuropathy, osteopathy, and short and long term micro and macrovascular problems arise from diabetes [2, 3]. In type 1 diabetes, the pancreas fails to produce enough insulin which is necessary to breakdown sugar for cellular absorption. Insulin therapy is required to treat type 1 diabetes. On the other hand in type 2 diabetes the pancreas fails to adequately regulate insulin in the body and cells are insulin resistant, requiring patients to take preventive actions to maintain normal glycemic levels. Diabetic patients thus need to check blood or urine glucose levels regularly and take preventive actions.

Current preventive actions require manual intervention of patients, while semi and fully automated diabetes management systems have been widely reported in literature and deployed for clinical trials. The clinical results show promising glycemic control in diabetic patients, however, the systems still lack key physiological information to accurately predict day to day glucose levels [4, 5]. In practical implementations, a comprehensive monitoring

system consisting of an accurate glucose monitor with real time predictive feedback of a patient's physiological induced glucose variations is thus required to realize an artificial pancreas. A closed loop automated insulin pump mimicking a pancreas is considered the ultimate solution in preventive treatment for diabetes management.

1.2 Motivation

After the discovery of insulin in 1920 by Fredrick Banting, the first use of insulin in an ambulatory patient was tested in 1970. In 1977, the first commercial closed-loop insulin regulatory system, the Biostator, was launched through the pioneering research of Albisse and Pfeiffer. In 1979, studies by Pickup and Tamborlane *et al.* demonstrated the possibility of using subcutaneous routes for continuous insulin delivery [5]. Applications of the predictive algorithm model opened the path for realizing a true closed loop insulin control [6-7]. Continuous glucose monitoring (CGM) technology has been prevailing for the last 10 years, and significant progress has been seen over that time. Recent CGMs use multiple sensor systems and feed the sensor data to predictive algorithms for insulin control. Clinical trials have demonstrated the usefulness of such continuous glucose monitoring systems [4, 5]. Blood glucose levels are well regulated when a CGM is used. This leads to the development of a complete diabetic management system, an artificial pancreas consisting of a continuous glucose monitor (CGM), process control algorithms, and a continuous subcutaneous insulin infusion (CSII) [6-8]. An artificial pancreas (AP) system, thus, could be the ultimate preventive solution for diabetes mellitus.

The true challenges in implementing an AP system lie in real life scenarios. Current AP algorithms need to use nonlinear feedback correlating physiological variables, exercise, meal intake, type of food, and sleep pattern [8]. These variables cause significant perturbations in a patient's blood glucose level. Until now, commercially available automated CGMs required manual intervention for physiological data, and can at best trigger alarms in case any such event is detected [8]. No robust solution has been demonstrated that can provide physiological feedback with high confidence.

Portable CGM systems are required to be flexible for use in ambulatory patients. One of the main challenges in a portable system is that it demands power efficient operation and compact implementation to ensure longtime use and less chip real estate. Digital circuit techniques do not always give a low power solution, as evident in power hungry digital signal processors, however, an analog processor can reduce the operating power by many times. A key problem associated with the current glucose sensor front end is that they use bulky sensor front ends and are not suitable for long term insertion. Recent advancements in nanotechnology offer microsensor solutions that can benefit users as they cause less cell trauma, use biocompatible materials for long term insertion, and offer better sensitivity, thus becoming a potential candidate for replacing current macrosensors.

1.3 Research Goals

My hypothesis is that traditional glucose sensor systems lack electronic readout that allows realization in a Lab-on-a-Chip or in an implantable platform which I propose can be met by developing new circuit topologies and inclusion of microfabricated nanostructures on the same chip. The current insulin pump system cannot predict the physiological events related to meals intake. This is important because any mismanagement of insulin intake with meal events can cause fatal consequences. The diabetic patient's security can be improved by providing a forensically aware insulin pump system which can detect meal events without manual intervention. This work develops an integrated CMOS glucose monitoring system using vertically aligned carbon nanofibers (VACNF) which offers low power implementation in a compact chip space, enhanced sensor sensitivity in the microscale, and continuous physiological information relating to meals events using bowel sounds. The proposed systems consist of four parts: 1) a compact VACNF micro-electrode sensor, 2) a power and area efficient sensor readout and signal transmitter, 3) bowel feature extractor and count block, and 4) low power CMOS solution for sensing continuous physiological data. While this work focuses on developing a total integrated CGM system, and introduces an onchip bowel detector, the system results impact patient treatment

actions, such as the Lab-on-a-chip glucose detectors offering possible future implantation with decreased trauma, increased glucose trend visibility, and better glucose control. The bowel sound detector can be utilized to automatically learn individuals eating instances eliminating the need for the patient to announce that a snack or meal event is about to happen.

1.4 Dissertation Overview

This dissertation is organized as follows. In Chapter 2, a complete literature review of vertically aligned carbon nanofiber (VACNF) structures has been presented, and the design and implementation of the sensor for glucose sensing have been demonstrated. Chapter 3 reviews the literature on transimpedance amplifiers and implementation of a low power area efficient sensor current readout block. Chapter 4 starts with literature review of potentiostats for glucose monitoring systems and wraps up with the proposed integration plan of the VACNF sensor with low power potentiostat and transmitter. Chapter 5 demonstrates the proposed bowel sound monitoring approach with piezoelectric sensors and system design with an analog feature extractor and algorithm unit. Lastly, the dissertation is concluded, and possible paths forward are presented in Chapter 6.

CHAPTER 2
VERTICALLY ALIGNED CARBON NANOFIBER BIOSENSOR

2.1 Literature Review

Recent advancements in nanotechnology have promoted the use of nanostructure based biosensors for clinical diagnoses. Compared to macroscale sensors, microsensors or nanosensors have shown much higher sensitivities and selectivity. In the large range of available sensor materials, Carbon is a popular sensing electrode primarily due to its unique structural and material properties and potential biocompatibility. These structural and material properties include high conductivity, durability in harsh environments, and inertness to processing steps [9-13]. Carbon allotropes, such as diamond and graphite, are mined naturally. The structure of these allotropes are formed of a mesh of sp^3 or, sp^2 hybridized carbon atoms. Kroto *et al.* first reported the observation of synthetic carbon allotropes, the fullerenes, widely known as buckminsterfullerene [14]. Successful synthesis of carbon nanotubes were first reported in 1991 and graphene in 2004 [15]. Carbon allotropes consisting of networks of sp^3-, sp^2- and sp- hybridized carbon atoms such as graphene, fullerene derivatives, carbon nanofibers, and carbon nanotubes show great potential as sensing materials for biological applications. Filamentous carbon formation on a hot metal surface in the presence of a carbon containing gas was reported in a US patent published in 1889 [16]. The first transmission electron microscope (TEM) image of filamentous carbon (also known as "soot particles") was reported in 1952 by Radushkevich and Lukyanovich [17]. After the discovery of fullerenes, synthesis of carbon nanofibers and carbon nanotubes generated interest among researchers facilitated by the advent of catalytic plasma enhanced chemical vapor deposition (C-PECVD) [18]. PECVD provided control over nanostructure synthesis. Chen *et al.* reported the synthesis of nanofibers using PECVD in 1997 which was supported and established by the work of Ren *et al*. [18].

Melechko *et al.* reported vertical aligned carbon nanofiber synthesis and assembly techniques in detail [18]. Carbon nanofibers are conical structures with diameters in the

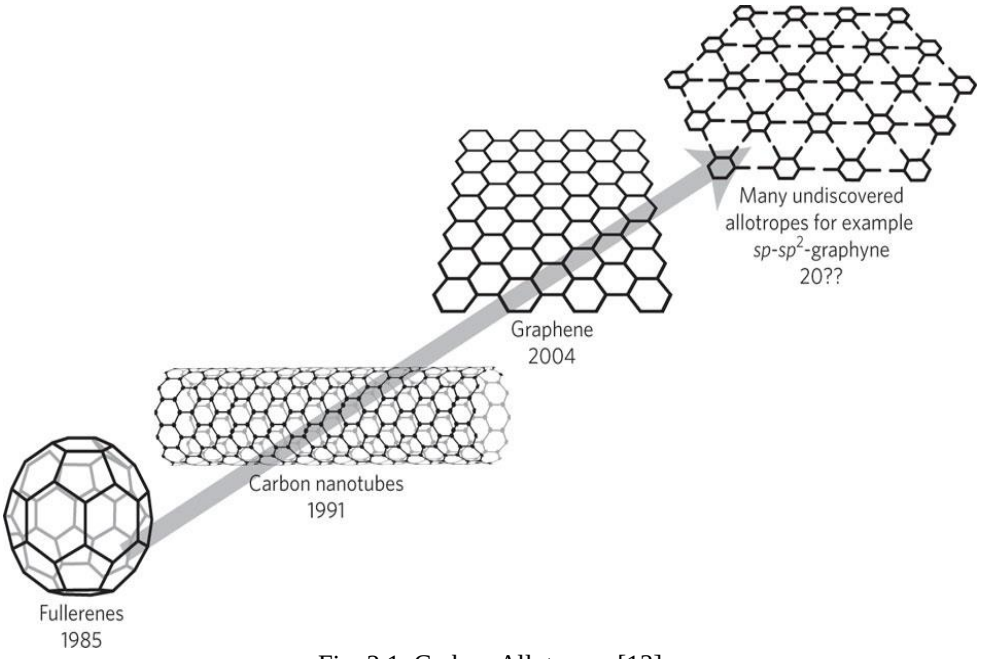

Fig. 2.1. Carbon Allotropes [13]

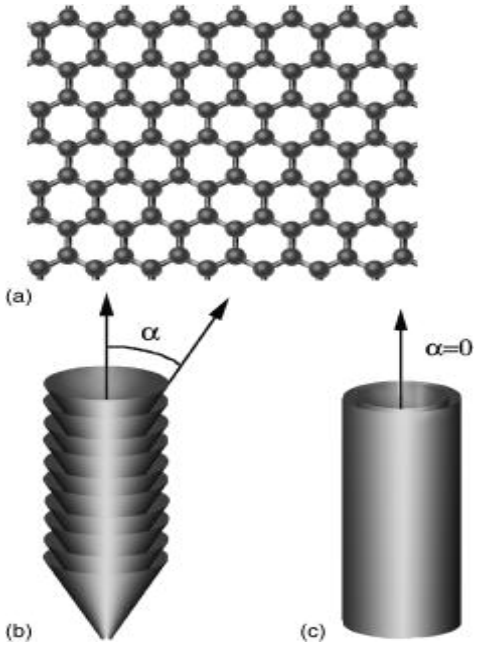

Fig. 2.2. (a) Graphene layer (b) carbon nanofiber (c) carbon nanotube [18]

range of few to hundreds of nanometer and lengths from less than a micrometer to millimeters [18]. Nanofibers consist of stacked curved graphite layer that form cones or, cups also known as herringbone or fishbone structure [18]. Carbon nanofibers are comprised of different arrangements of graphene sheets. Graphene sheets are 2D layer of 3D graphite. According to Melechco *et al.*, the angle between the fiber axis and the graphene sheet near the surface determines the type of carbon nanostructure [18]. If the angle value is zero, then the graphene layer along the surface of the nanostructure forms a special type of carbon allotrope, the carbon nanotube. Carbon nanotubes have special unique mechanical and electrical features due to this continuous graphene layer on the surface. If the angle is greater than zero then the graphene layers are weakly connected, and run only a part of the length forming conical layers like cups. This structure is known as the nanofibers. Both the graphene inplane and interplane components are responsible for change transfer in the nanofiber. Mechanical properties of nanofibers are different from nanotubes due to variations in the Van der Waals bonding between the graphene planes. In terms of chemical reactivity, nanofibers have defect edges and unsaturated bonds which are not present in the defect free carbon nanotube surface. Hence, carbon nanofibers are more chemically reactive when compared to carbon nanotubes.

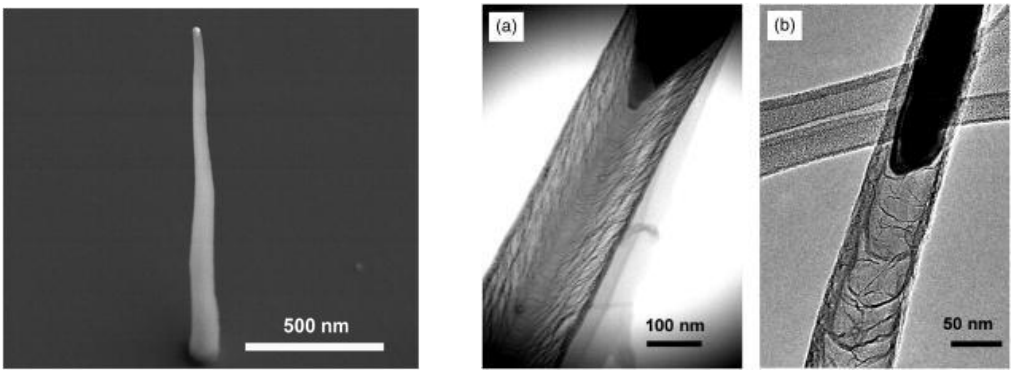

Fig. 2.3. A single carbon nanofiber , (a) SEM image of conical carbon nanofiber, (b) TEM image of bamboo-type carbon nanofiber grown with iron (Fe) catalyst [18] .

In fact, the VACNF is a conical structure of stacked grapheme layers where the open ended layers are abundant with acidic and basic groups that act as electrochemical reaction centers

[18-21]. Charge transfer occurs in these reaction centers during electrochemical reactions. VACNFs can be deterministically grown in a predetermined pattern on silicon or quartz surfaces. In addition, the growth process of VACNF allows the growth of a single fiber or forests of fibers and is dependent on the catalyst size. Forest of fibers has the advantage of fiber redundancy as well as reduced probability of fiber blow-off during the extensive growth process [35].

Glucose monitors widely use enzymatic sensors [11, 22-26]. Addition of chemically stable nanostructures in the sensing unit can significantly improve the sensor sensitivity. There are quite a few potential nanostructures reported in literature, such as TiO_2 nanostructures, CuO thin nanosheets, ZnO nanowires, Pt-Ir nanomaterials, Au nanoparticles, Pt nanotubules and CuO nanowires that promise improved sensor sensitivity [27-33]. VACNF forests with their unique capability of high loading of catalyst, high enzyme binding and high detection sensitivity are a good choice for enzymatic sensors [34-36]. VACNFs are also chemically stable and can be useful in detecting a wide range of analytes with appropriate enzymatic functionalization. The high conductivity of the nanofiber microelectrodes presents a low charge transfer resistance and helps the transfer of the electrochemical charges from the oxidation and reduction reactions to the external readout.

2.2 VACNF Microelectrode Implementation

2.2.1 Fabrication of VACNF Microelectrodes

Melechko *et al.* reported the fabrication process of VACNF on a silicon wafer [18]. DC plasma enhanced chemical vapor deposition (PECVD) was used to synthesize fibers on a silicon wafer. The successful growth of carbon nanofibers limits the choice of materials that can be present in the silicon wafer [37, 38]. A strong interaction is necessary between the catalyst and the support substrate, and the Ni/TiO_2 system exhibits the strongest interaction in comparison to Ni/SiO_2 and Ni/Al_2O_3 systems [38]. The activity of a metal catalyst support system depends on a variety of factors which include the dispersion of the

metal salt precursor on the support. While this limits the choice of materials, Ti interconnects on Si substrate can support successful growth of CNF.

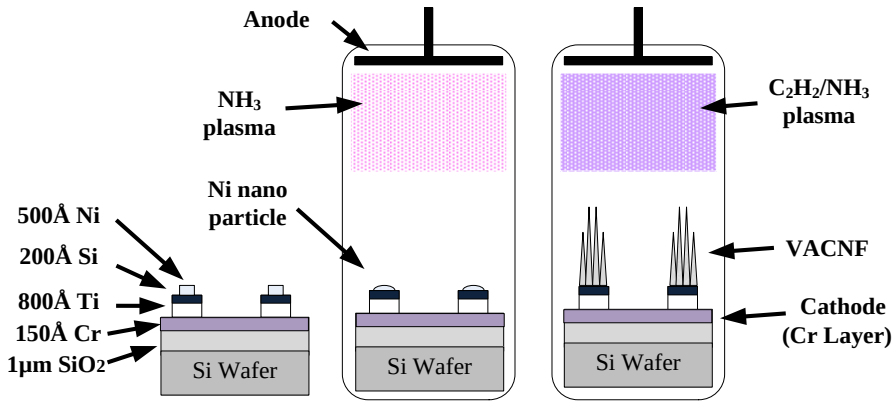

Fig. 2.4. VACNF growth process: 150Å Cr, 800Å Ti, 200Å Si and 500Å Ni were deposited on 1000Å thick SiO_2 layer on Si wafer. C_2H_2, NH_3 were flowed in the PECVD chamber at 700°C and pressure of 15Torr. Carbon continues to deposit under Ni catalyst and finally forms fiber forest.

A conducting surface of Chromium (Cr) was deposited on the wafer by chemical vapor deposition (CVD). The Cr acted as the cathode in the PECVD process. By using a prepatterned mask, metal contacts and interconnects were patterned using standard photolithography techniques. Ni dots were prepatterned on the wafer at predetermined positions using photolithography techniques. These Ni dots act as catalysts for VACNF growth. Acetylene (C_2H_2) and Ammonia (NH_3) were supplied through an upper showerhead in the PECVD chamber. In the reaction, acetylene acts as carbon source and ammonia as the etchant gas. To initiate fiber growth, the silicon wafer was mounted on a heater plate in the PECVD chamber and heated to about 700^{O}C. The chamber pressure was raised to 15 Torr, which initiates the plasma in the PECVD chamber. Ammonia plasma facilitates the formation of Ni nanoparticles from Ni dots, which later in the plasma reaction act as the seeds for the VACNF growth. The introduction of acetylene in the PECVD chamber initiates the growth of nanofiber under the Ni catalyst. The reaction time for VACNF growth was approximately 20-25 minutes. After VACNF growth, the conductive Cr layer was removed from the wafer leaving the interconnects and pads using Reactive

Ion Etch (RIE). The nanofiber morphology is a function of plasma power, ratio of C_2H_2/NH_3, flow rate, growth time and catalyst size. The catalyst diameter governs the type of the fiber. A catalyst diameter less than 100nm promotes single fiber growth, while greater than 100nm results in a forest of fibers [39]. Fig. 2.4 illustrates the VACNF growth process in detail.

2.2.2 VACNF Microelectrode Architectures

VACNF architectures have been explored for electrochemical sensors. The first sample is a long strip of metal of 12mm in length and 113μm in width on silicon (Fig. 2.5). VACNFs were grown with different densities of VACNF fibers with pitches of 5μm, 7.5μm, 12μm and 17μm. A total of 21,900 VACNF forests were grown on the metal strip and the VACNFs can be accessed with a metal pad. Another sample with a length of 300μm and width of 300μm was patterned on silicon wafer with different densities of the VACNF fibers containing 225 VACNF forests with 20μm pitches, and containing 400 and 900 VACNF forests with 15μm and 10μm pitches, respectively (Fig 2.6) [34].

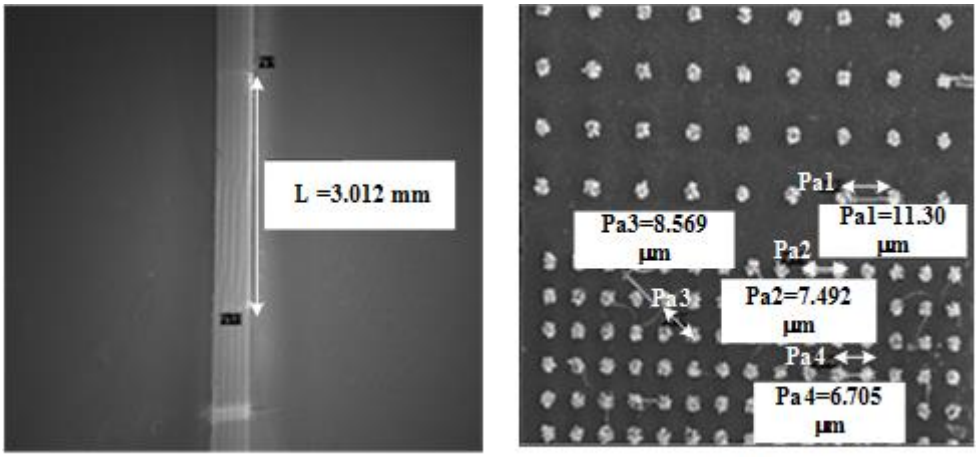

Fig. 2.5. (a) A section of the VACNF sample 1 (VACNF grown in 113μm × 3mm strip), (b) Magnified view of the VACNF grown region (different densities of VACNF grown on a single strip. Pitch Pa1 = 11.30μm, pitch Pa2 = 7.492μm, pitch Pa4 = 6.70μm) [34].

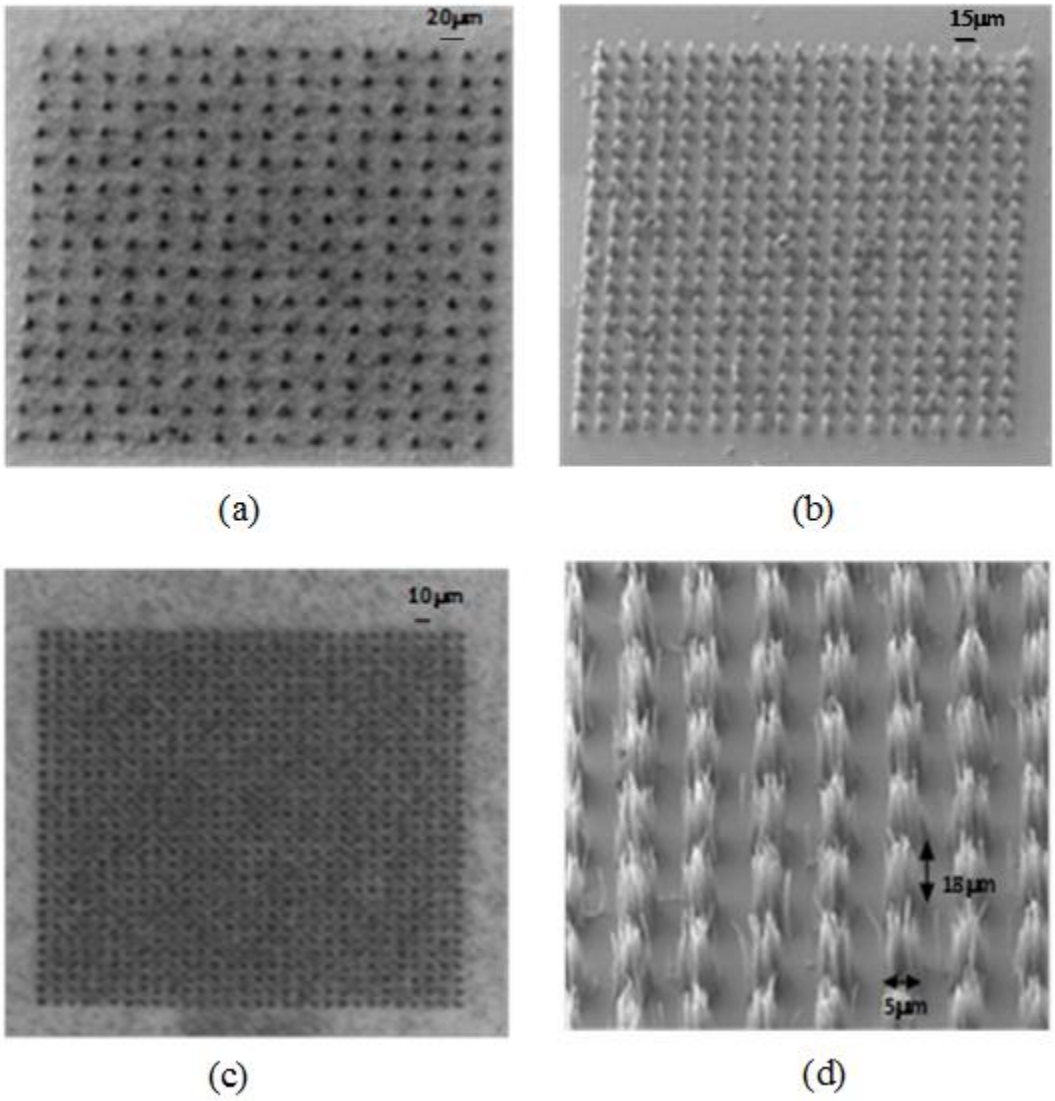

Fig. 2.6. (a) VACNF sample 2 type 1 (pitch 20µm), (b) VACNF sample 2 type 2 (pitch 15µm), (c) VACNF sample 2 type 3 (pitch 10µm), (d) SEM image of the VACNF forests in sample 2 (VACNF forest height = 18µm, VACNF forest base width = 5µm) [34].

2.2.3 VACNF Microelectrode Characterization

2.2.3.1 Reagents

To characterize the VACNF the following reagents were obtained from Sigma Aldrich and used without further modification: 0.1M phosphate buffer solution (PBS), 98% ruthenium hexamine trichloride ($Ru(NH_3)_6Cl_3$), 1M potassium chloride (KCL). The solutions were prepared with Milli-Q deionized water and stored at 4^{o}C in a refrigerator.

2.2.3.2 Instrumentation and Techniques

A CHI660D electrochemical analyzer was used to characterize the VACNF microelectrodes. A plastic reservoir was glued around the VACNF microelectrodes to hold liquids. The electrochemical analyzer was configured in two wire mode (counter electrode and reference electrodes tied together) to detect low currents (nA) and in three wire mode when detecting high currents (µA to mA). A standard Silver/Silver chloride (Ag/AgCl) electrode is used as the reference and counter electrode. An electrochemical cell is a device which facilitates electron transfer in a chemical reaction to or from electrodes with the help of an electrical potential. In this device, the VACNF microelectrodes form the working electrode of the electrochemical cell. Phosphate buffered solution (PBS) was used to maintain a constant pH of 7.4 throughout the testing period. Ruthenium hexamine trichloride, a standard oxidation and reduction reagent widely used in electrochemical characterization, was used to verify surface activity of the working VACNF microelectrodes.

2.3.3.3 Cyclic Voltammetry

Cyclic voltammetry is an electrochemical technique where an electrode potential ramps up and then back down and corresponding currents in the electrochemical cell measured and plotted against the electrode potential. Cyclic voltammetry (CV) has been very useful in the studying of biosynthetic pathways and electrochemical free radicals in organic

chemistry, studying the effects of ligands on the oxidation/reduction potential of central metal ion of complexes, facilitating analysis on enzymatic catalysis and exploring novel ways to introduce functional groups into complexes [40]. In a cyclic voltammetry, the potential of the "working electrode" Ei , ramps from an initial value to a value $E\lambda_1$ which is known as the switching value where the direction of the ramp is reversed. The ramp direction can be switched when its reach to a potential $E\lambda_2$ or, Ei (Fig. 2.7).

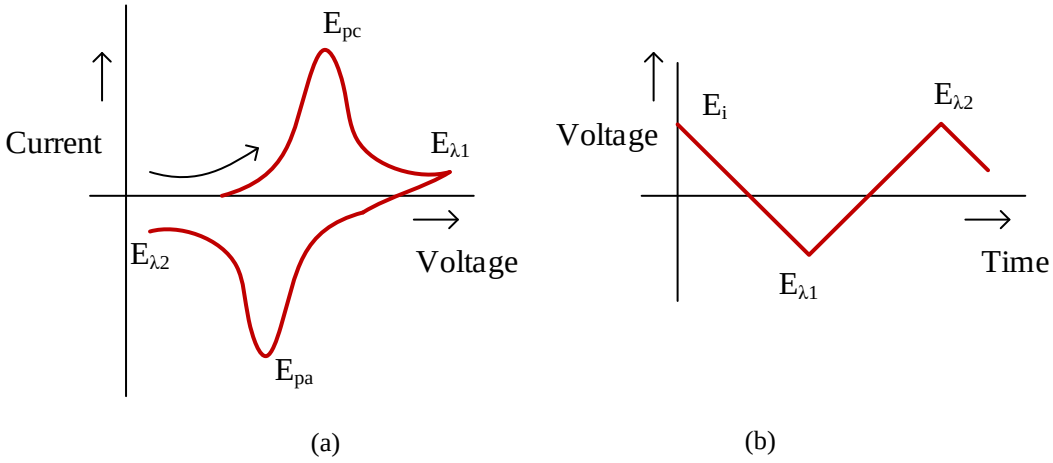

Fig. 2.7. (a) Cyclic voltammetry plot, (b) Ramp signal generated [46]

As the potential is scanned, the current increases until it reaches a peak then decays in a regular manner. The electrochemical current is dependent on two processes, the transfer of electroactive material to the surface of the electrode, and the electron transfer reaction occurring at the electrode-electrolyte interface. The electron transfer rate constant can be expressed as [40]:

$$k_f = k_o \exp\left(\frac{-\alpha n F}{RT}(E - E_o)\right) \quad (1)$$

Where k_o is the standard heterogeneous electron transfer rate constant whose value is dependent on the reaction property between the compound and electrode surface. n denotes the electron transferred per molecule, F is the Faraday constant (96,485 C mol $^{-1}$), R is the universal gas constant (8.314 J mol^{-1} K^{-1}), T denotes temperature in unit kelvin, E_o denotes the formal reduction potential and α denotes the transfer coefficient [41]. For a reversible reaction, the reactions need to be fast enough to maintain equilibrium of the concentrations

of the oxidized and reduced form at the electrode surface. The equilibrium condition can be expressed using the Nerst equation:

$$E = E_o - \frac{RT}{\mathrm{nF}} ln \left(\frac{[R]}{[O]}\right)_{x=0} \quad (2)$$

where R is the reduced form and O is the oxidized form.

2.2.3.4 Test Results

VACNF microelectrodes in an array were varied over samples to compare microelectrode performance. In sample 1, four islands of varying VACNF microelectrode densities were patterned on a single metal strip. In sample 2, VACNF microelectrodes with 10µm, 15µm and 20µm pitches were microfabricated on a 300µm × 300µm square area (Fig. 2.6). During the VACNF growth it was observed that dense forests promote the VACNF growth, possibly due to the localized electric field resulting in taller nanofibers similar to the work in [18]. The defect rich sites of the VACNF facilitate enzyme binding and offer increased reactivity to electrochemical reactions. Thus, the current responses of different samples in $Ru(NH_3)_6Cl_3$ were compared to extract the microelectrode sensitivity. The VACNF microelectrodes were characterized with 2.5mM $Ru(NH_3)_6Cl_3$ in 1mM KCl solution. The oxidation and reduction peaks were observed at -0.15V and -0.19V, respectively in the cyclic voltammetry (CV) plot of $Ru(NH_3)_6Cl_3$ (Fig. 2.8(a)). The peak currents generated in the electrochemical reaction are proportional to the electrochemical active sites of VACNF, and hence reflect the surface reactivity of VACNF microelectrodes. The peak reduction currents are compared with the total number of VACNF microelectrodes in the samples. (Fig. 2.8(b)). It was observed that the peak reduction currents increase with the number of VACNF microelectrodes in the samples. The peak current densities of a microelectrode in a sample were compared and the results demonstrated that current density per microelectrode decreases as the number of VACNF microelectrode increases in a sample (Fig. 2.9(a)). The capacitance of the VACNF microelectrodes were measured from the cyclic voltammetry of $Ru(NH_3)_6Cl_3$. The charging currents were measured at the open circuit electrode potential and for the instrument scan rate of 100mV/s [34]. The calculated

capacitances increase as the VACNF microelectrode number increases in a sample (Fig. 2.9(b)).

(a)

(b)

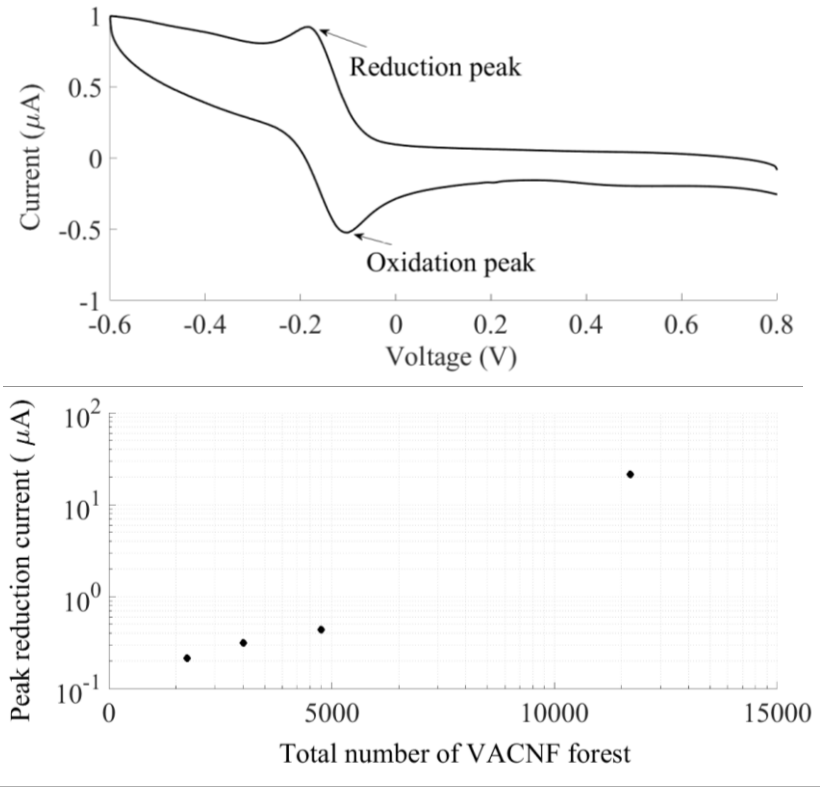

Fig. 2.8. Plots showing (a) CV plot of $Ru(NH_3)_6Cl_3$, (b) peak reduction current with the number of VACNF microelectrodes in a sample [34]

2.2.3.5 Discussion

The detection limit of VACNF microelectrodes can be tailored by examining the functional dependent parameters of VACNF electrochemical sensors. Densely grown VACNF microelectrodes in electrochemical sensors demonstrate high sensitivity, however they are not applicable for high concentration of analyte detection due to diffusion limitation effects. The VACNF microelectrodes demonstrate high specific capacitances and are an indication of an increased charge active surface area [34]. The deterministic design of the VACNF electrode based sensor thus depends strongly on the of electrode sensitivity, limit of detection (LOD), selectivity and the sensing limitations.

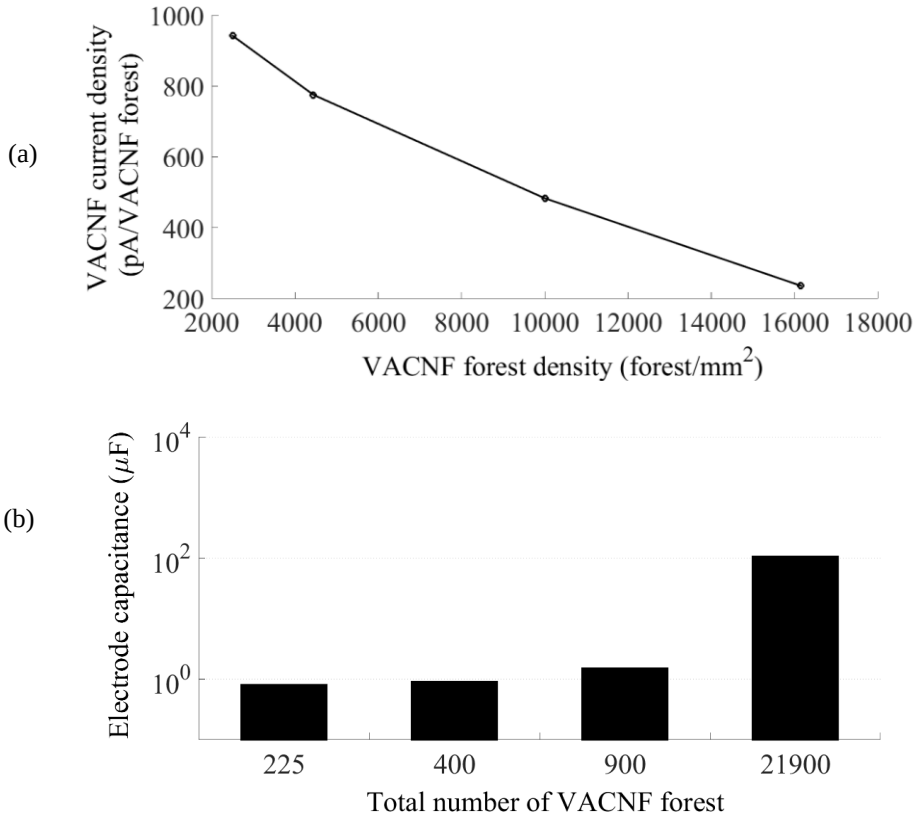

Fig. 2.9. Plots showing (a) VACNF microelectrode current density in a sample, (b) VACNF microelectrode specific capacitance with the number of VACNF microelectrode in a sample [34].

2.2.4 Robust VACNF Microelectrode Implementation

The VACNF surface, which is abundant with the reaction active sites, contains predominately acidic and basic sites which facilitate electrochemical charge transfer. Dense VACNF forests impede diffusion due to the closely located neighboring VACNF forests whose diffusion range interferes with each other. This results in substrate noise and can potentially limit the detection range. VACNF fibers are also weakly attached to the substrate and vulnerable to repeated electrochemical and washing steps. Surface passivation using SiO_2 and layers of SU8 coating has been used to improve the noise performance and strengthen single VACNF fiber microelectrodes [42]. For VACNF forests microelectrodes surface treatment strategy has been explored to obtain the optimum performance.

2.2.4.1 Surface Treatment

Surface treatments of a single VACNF fiber with SiO_2 passivation coating followed by SU8 coatings has shown much promise towards minimizing interference and strengthening single fibers for individual use. Similar treatment has been exercised for VACNF forests, however, after coating with 115nm of SiO_2 and dry etching using plasma RIE, the VACNF forests resulted in mechanically weak structures as the etching creates a nonuniform coating of SiO_2. Further coating with SU8 proved to be inefficient. On the other hand, using a thick SU8 coating on the VACNF forests makes it harder to control SU8 thickness and etch the tips. However, while adopting a thin SU8 coating and wet etch using buffered oxide (BOE:HF) a more stable and robust VACNF forest structure was developed. For this particular test, permanent epoxy negative photoresist SU8 2005(density:1.164 g/ml) was spun on the wafer at 2000 rpm for 45 seconds to form a 5µm thick SU8 layer which was then soft baked at 65ºC for 1 minute and then subsequently at 95ºC for 2 minutes. The surface treatment strategy proposed and adopted to process the VACNF forest microelectrodes is shown in Fig. 2.10.

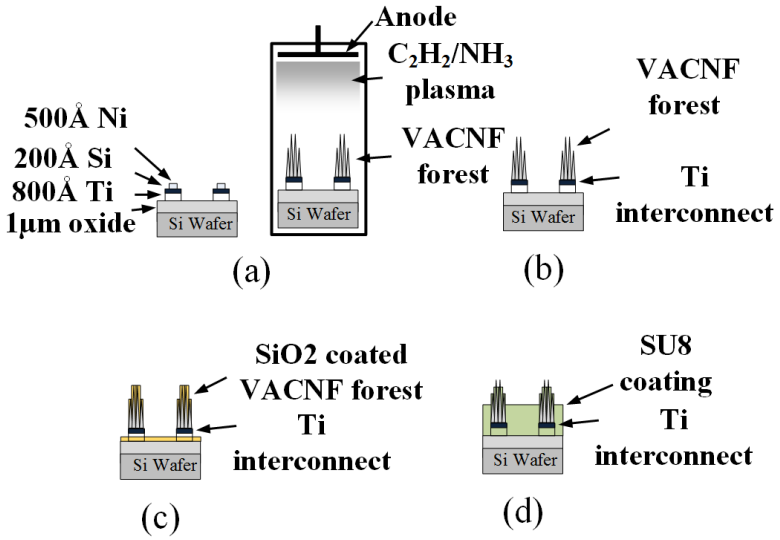

Fig. 2.10. (a) PECVD process, (b) VACNF grown on Si substrate, (c) Thin SU8 deposited on VACNF array, (d) SU8 wet etched from VACNF forest tips.

2.2.4.2 Dry Etch Vs. Wet Etch

Dry etch was performed with a plasma RIE etcher and wet etching was performed in a wet bench with 6:1 buffered HF. Dry etch was performed for 1 minute. Wet etching was adopted to etch away thin SU8 from fiber tips. The samples were dipped in 6:1 BOE:HF for 2 to 3 minutes followed by a washing step to shed off the SU8 from fiber tips and surface. The exposed region of VACNF microelectrodes are the only reactive parts to electrochemical reactions. Fig. 2.11(a) shows bare VACNF forests before the surface treatment, Fig. 2.11(b) shows the VACNF forests covered with a thin SU8 layer. Fig. 2.11(c) shows SiO_2 treated and dry etched VACNF microelectrodes.

2.2.4.3 Test Results

To verify the surface treatment effect on the VACNF, the SEM images and microscopic images of the microelectrodes were compared following consecutive electrochemical tests. All characterization tests were performed with 5mM $Ru(NH_3)_6Cl_3$ solutions. Since the peak current of the cyclic voltammetry plot is proportional to the number of VACNF forests microelectrode on a sample and active surface area, bare VACNF forests were compared with surface treated VACNF forests. The SEM images of the bare VACNF forests microelectrode array are shown in Fig. 2.11(a). Fig. 2.11(b) shows VACNF forests treated with thin SU8 2005 and etched with 6:1 BOE: HF. The VACNF forests tips were exposed and active for electrochemical reactions. Fig. 2.11(c) shows VACNF forest microelectrodes coated with 115nm SiO_2 and RIE dry etched. It is evident from the SEM image (Fig. 2.11(c)) that RIE results in a non-uniform passivation coating on the VACNF forests indicating that RIE is not a good alternative to etch SiO_2 from the VACNF forests. RIE etches away the passivation coating uniformly perpendicularly located from the plasma and from the VACNF surface. Thus etching is not localized to the fiber forest tips and causes a weak VACNF forest after the etching steps. Electrochemical tests were performed to examine the surface functionality of the surface treated VACNF microelectrodes. Fig. 2.12 shows images of bare and surface treated VACNF microelectrode arrays in 20 consecutive CV tests with $Ru(NH_3)_6Cl_3$ solution in

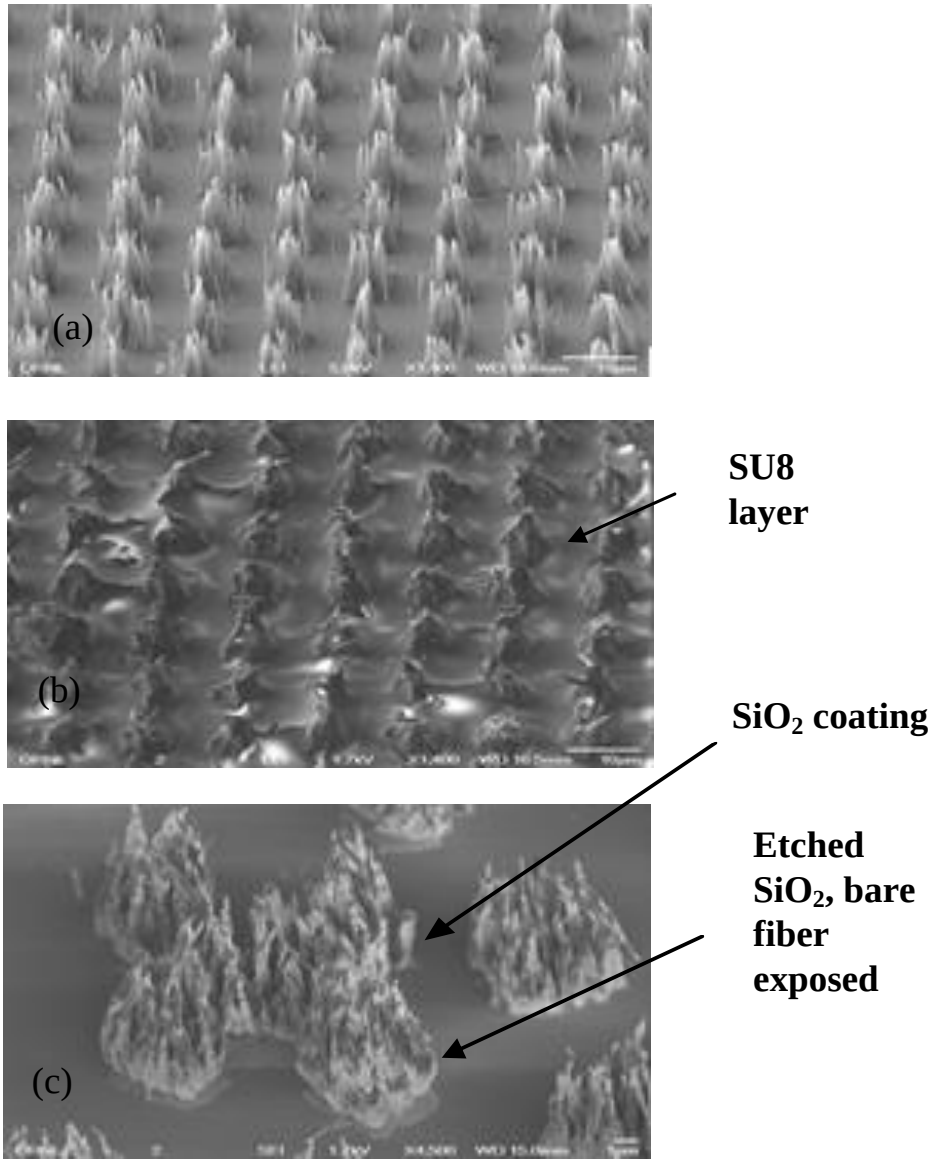

Fig. 2.11. (a) Bare VACNF array on metal pad, (b) SU8 treated and wet etched VACNF array, (c) SiO_2 deposited and RIE dry etched VACNF array [43].

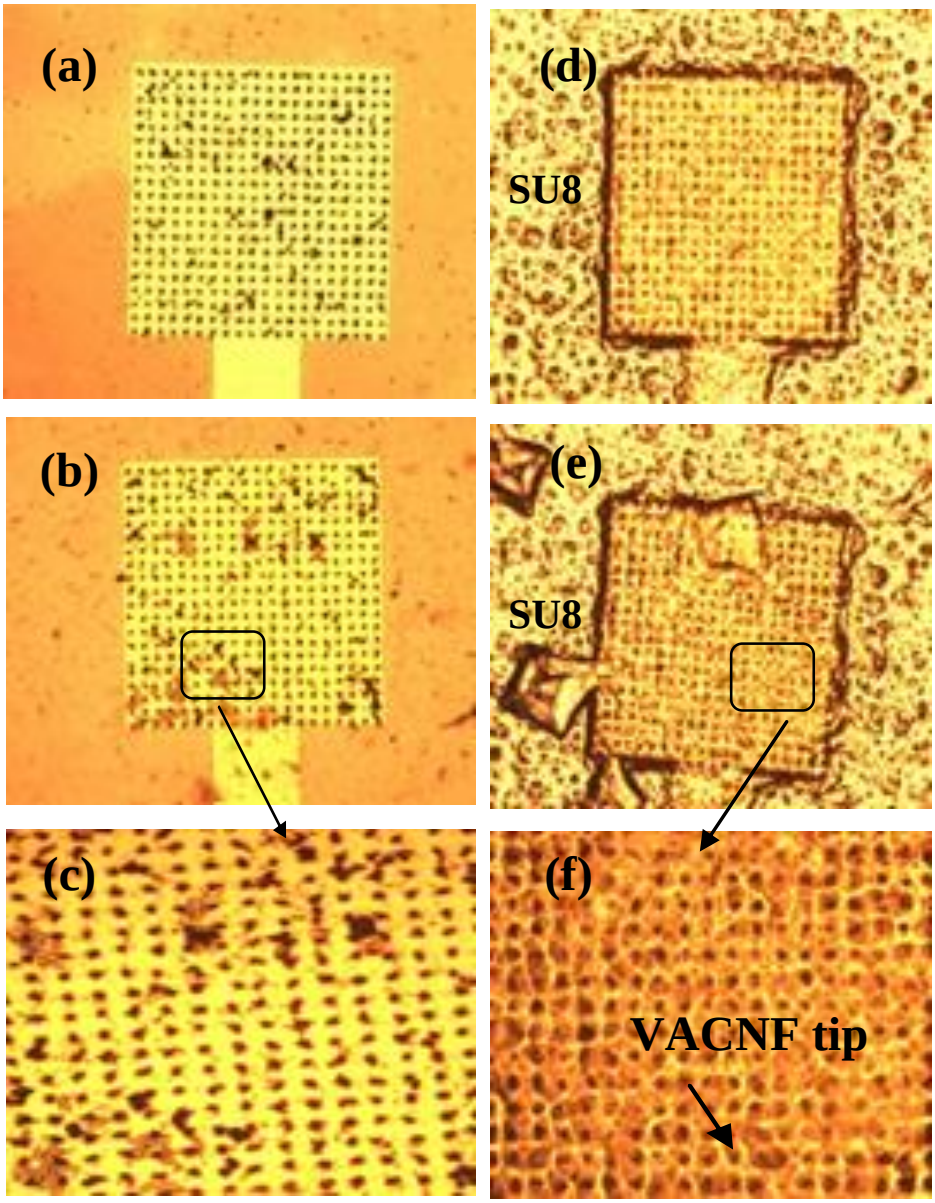

Fig. 2.12. (a) VACNF array on metal pad, (b) bare VACNF array after 20 consecutive tests, (c) zoom view of damaged bare VACNF array, (d) VACNF array treated with SU8, (e) SU8 treated VACNF array after 20 consecutive tests, (f) zoom view of Robust VACNF array [43].

PBS. The tests were followed by rinsing with PBS solution. Visual analysis of the images demonstrates that bare forest arrays suffer from severe structural damage after the consecutive tests when compared to surface treated VACNF forests. Electrochemical tests support this claim which is evident from Fig. 2.13. The reduction peaks were hardly visible for the bare VACNF microelectrodes after the 16^{th} consecutive tests however no visual degradation has been observed for the surface treated VACNF microelectrodes. Barely visible peaks in the CV plots are strong indications of poor signal to noise ratio. Thus it has been verified that the SU8/wet etch surface treatment results in an improved SNR in VACNF microelectrodes. The comparison of the peak reduction currents of the bare VACNF array and surface treated array is shown in Fig. 2.14. After consecutive tests the SNR of bare forest fibers suffers significantly, whereas SU8/wet etch treated forests demonstrate a steady response even after 20 consecutive tests. The standard deviation of the reduction current compared to bare VACNF array ($\sigma = 0.349\mu A$) demonstrates high stability for the SU8 treatment ($\sigma = 0.048\mu A$). It was verified from the responses that bare VACNF forest microelectrodes were less durable compared to the SU8 treated VACNF forest microelectrodes. The surface treatment with SU8/wet etch clearly improves the SNR and the VACNF forest microelectrode durability in the electrochemical test environment [43].

2.3 Empirical Modeling of VACNF Microelectrode

Carbon nanofiber response over a wide frequency range may be modelled by a parallel RC network [44, 45]. According to Helmholtz theoretical explanations of electrode electrolyte double layer, double layer capacitances can appear at the electrode-electrolyte junctions. VACNF forests in an electrochemical cell can be modeled with double layer capacitances, charge transfer resistances and other constant phase elements such as Warburg constants.

2.3.1 Electrochemical Impedance Spectroscopy (EIS)

Electrochemical impedance spectroscopy (EIS) is a technique where the electrochemical cell impedance is measured and plotted against the ac source frequency. EIS proves useful

(a)

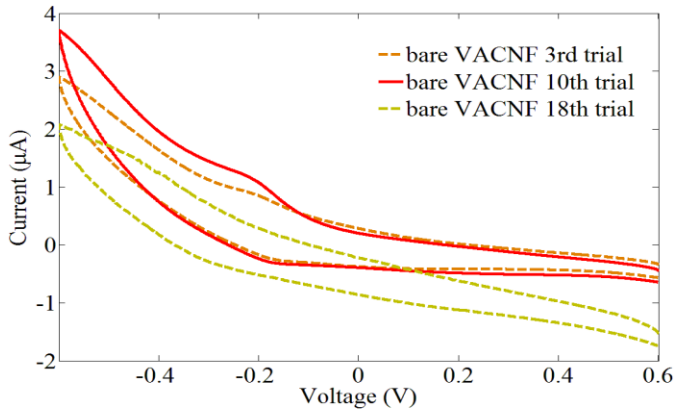

(b)

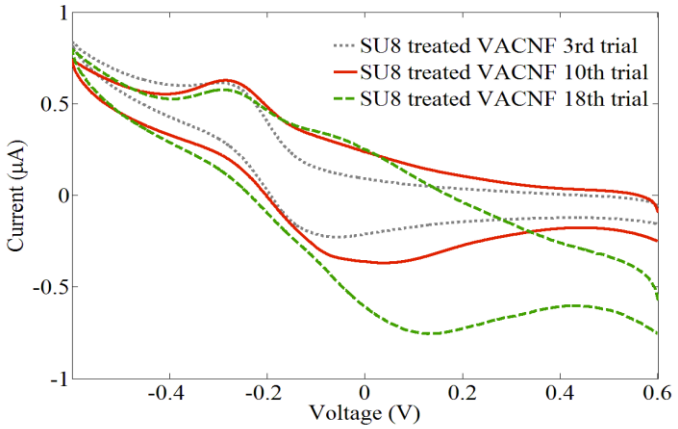

Fig. 2.13. Cyclic voltammetry plots of $Ru(NH_3)_6Cl_3$ for (a) bare VACNF array and (b) SU8 treated VACNF [43].

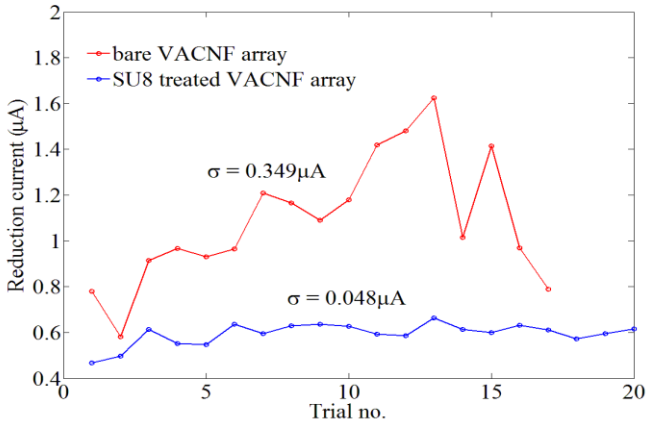

Fig. 2.14. The reduction peak current in 20 consecutive tests in $Ru(NH_3)_6Cl_3$ solution [43].

in quantitative analysis of porous electrode and distinguish dielectric and electrical properties of materials. EIS also allows the investigation of the electrode in terms of AC frequency and modeling of the cell using lumped RC circuits. The AC impedance of an element can be expressed as below,

$$Z(\omega) = \frac{\delta V(\omega)}{\delta I(\omega)} \tag{3}$$

where Z(ω) is the AC impedance, δV(ω) is the change in voltage and δI(ω) is the change in current (Fig. 2.15)

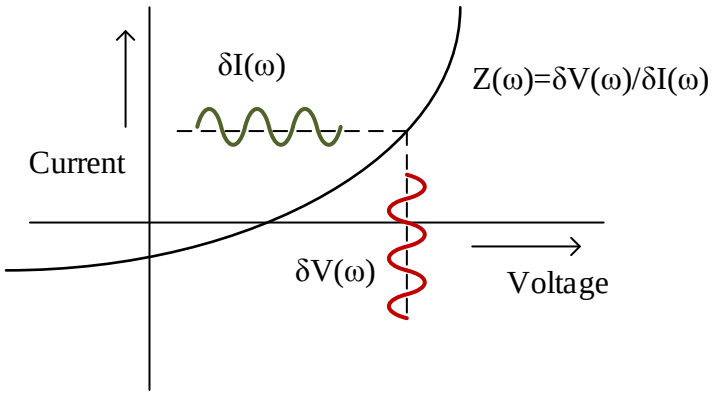

Fig. 2.15. Analyzing Impedance

2.3.1.1 Bode Plot

The impedance can be plotted in a log scale, where the x axis is log frequency and the y axis is both the log absolute magnitude of impedance (|Z|) and phase angle. A bode plot shows frequency versus impedance information and enables one to discern effects of lumped circuit elements over the frequency spectrum. Fig. 2.16 shows a bode plot of a RC circuit [40]. A bode plot shows the effect of a single time constant and the location of the pole. At the pole the phase shifts by 90^{o} and the gain rolls off.

2.3.1.2 Nyquist Plot

The impedance can also be expressed as vector. The complex impedance can be expressed as,

$$Z = \frac{E}{I} = Z_o exp(i\emptyset) = Z_o(cos\emptyset + isin\emptyset) \quad (4)$$

where Z is the net impedance, Z_o represents the impedance at dc, E is the applied voltage, I is the current, $\emptyset$ is angular frequency. A Nyquist plot is generated when the imaginary impedance is placed in y axis and real impedance in x axis. The vector length represents the absolute value of the impedance and the angle between the vector and x axis, $\emptyset$, represents the frequency. Thus, low frequency data typically lies on the right side of the Nyquist plot and high frequency data on the left side. The Nyquist plot of an RC circuit can be approximated by a semicircle (Fig. 2.16(c)).

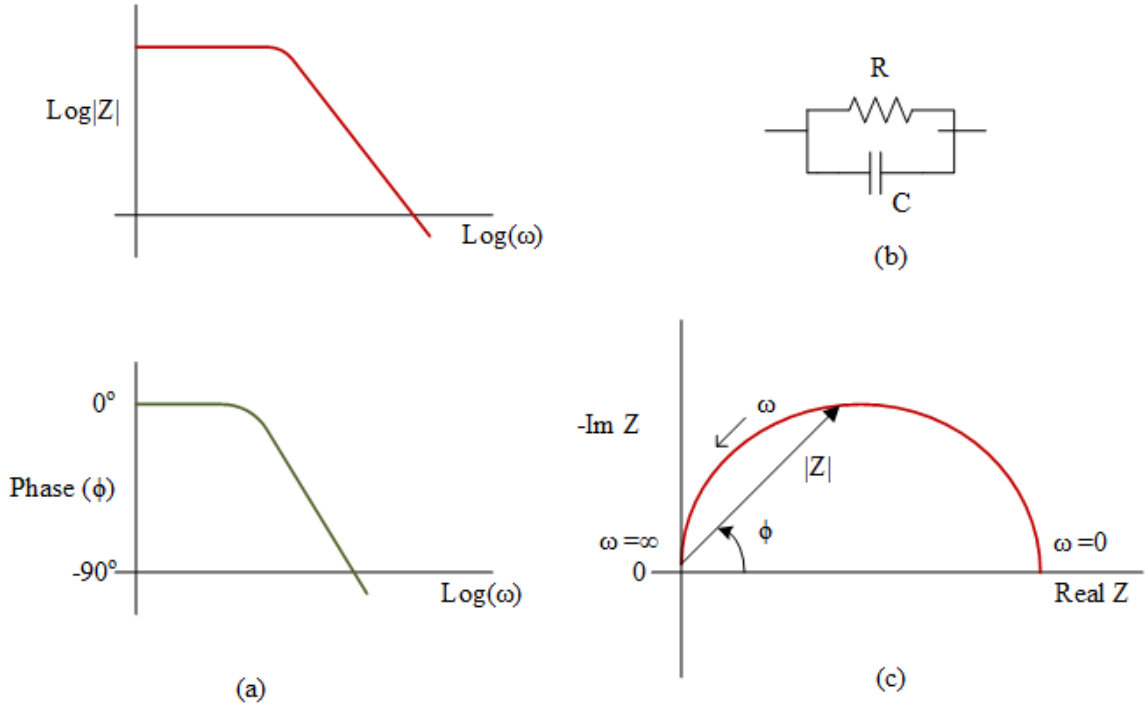

Fig. 2.16. (a) Bode plots, (b) Equivalent circuit, (c) Nyquist plot [46]

A Randles cell is the simplest form of an electrochemical cell model, and consists of a solution resistance R_s, a double layer capacitance, C_{dl}, formed at the electrode and an electrolyte surface, and a charge transfer or, polarization resistance R_{ct} or, Rp. The double layer capacitance is formed as the electrode is immersed in an electrolyte, where the ions in the electrolyte stick to the electrode surface and are separated from the electrode charges.

The charge transfer resistance is formed due to the kinetics of diffusion at the electrode surface. Diffusion gives rise to an impedance known as the Warburg impedance. The Warburg impedance is dependent on the frequency of the voltage perturbation, and decreases as the frequency increases. At low frequency, the movements of the reactant molecules extend in space which gives rise to higher Warburg impedance. The Warburg impedance can be expressed as in [46],

$$\mathrm{Z} = \sigma(\omega)^{\frac{-1}{2}}(1-j) \text{ for infinite diffusion layer thickness}$$

$$\text{, where } \sigma = \frac{RT}{n^2F^2A\sqrt{2}}\left(\frac{1}{C_o\sqrt{D_o}} + \frac{1}{C_R\sqrt{D_R}}\right)$$

$$\mathrm{Z} = \sigma(\omega)^{\frac{-1}{2}}(1-j)\ \tanh\left(\delta\left(\frac{j\omega}{D}\right)^{1/2}\right) \text{ for finite diffusion layer thickness} \qquad (5)$$

Here, δ is the Nerst diffusion layer thickness, ω is the angular frequency, D_o is the diffusion coefficient of the oxidant, D_R is the diffusion co-efficient of the reductant, D is the average value of diffusion co-efficient, A is the surface area of the electrode, n is the number of electrons transferred, and C_x is the concentration of diffusion species. The Randles cell Nyquist plot is shown in Fig. 2.17 and the Warburg impedance plot is shown in Fig. 2.18.

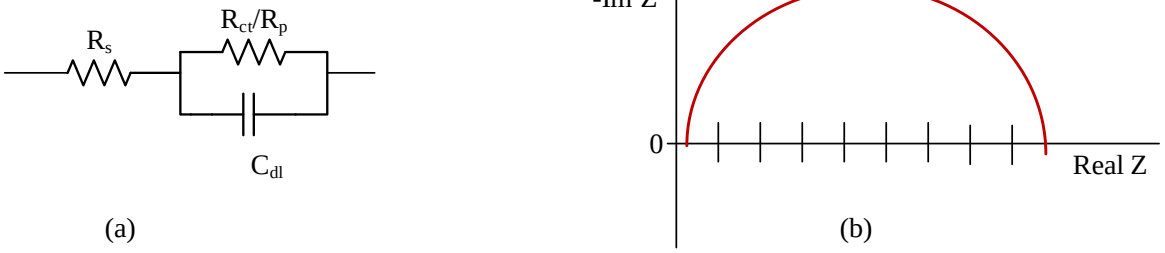

Fig. 2.17. (a) Equivalent circuit, (b) Randles cell Nyquist plot [46]

In an electrochemical cell where both kinetic and diffusion process of charge transfer occurs, the circuit model can be expressed as in Fig. 2.19. Mixed kinetics and diffusion can give rise to this type of response, which is a combination of double layer capacitance, charge transfer resistance and Warburg impedance. At low frequencies, the Warburg

impedance dominates with the charge and solution resistance while at mid frequencies only resistances dominate. At high frequencies the double layer capacitance dominate the cell's impedance.

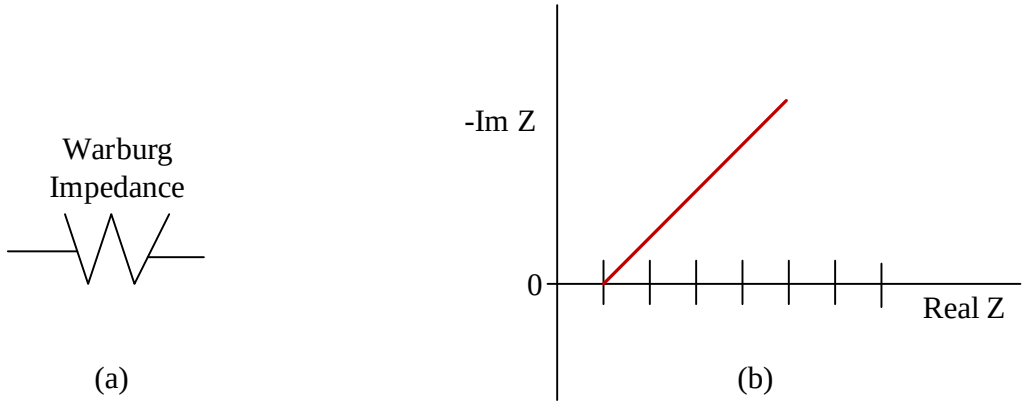

Fig. 2.18. Warburg Impedance [46]

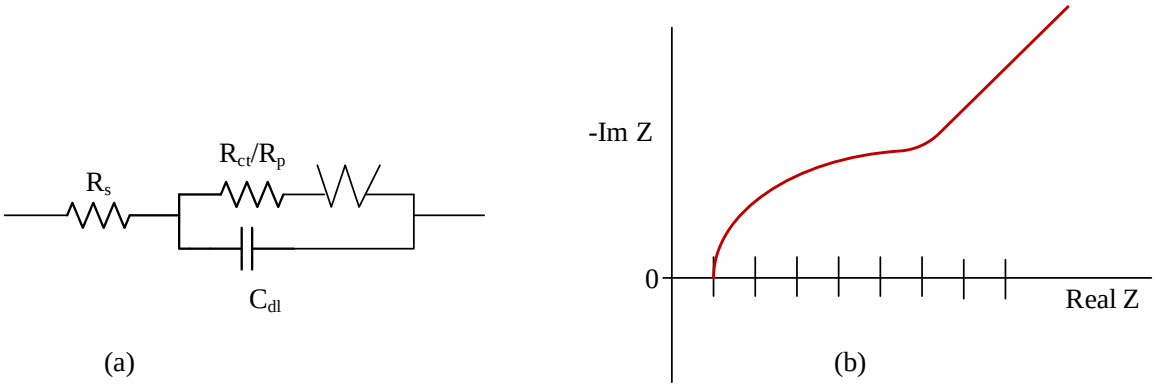

Fig. 2.19. Mixed kinetics and diffusion controlled cell [46]

2.3.2 Equivalent Circuit Model of VACNF microelectrodes

A number of models have been previously developed for VACNF fibers which show the relationship of the nanofiber density with electrochemical sensitivity [44, 45]. While a single nanoelectrode demonstrates high signal to noise ratio and is useful for biomolecule detection with high sensitivity, high density VACNF fibers typically demonstrate a macro-electrode behavior with anodic and cathodic peak currents and background charging or discharging currents. The microelectrodes used in this work resemble macroscale

electrodes with moderate sensitivity and enable operation within the electrode diffusion limits. The VACNF forests are distributed so that no interaction between the neighboring forests radial diffusion layers are present. Single uncoated carbon nanofibers have been modeled with Randles cell in a previous work which represents a single time constant [44]. The surface treatment of VACNF microelectrodes with SU8 followed by enzyme coating for functionalization, modifies the electrode properties significantly. The porosity of the carbon nanofiber presents a large surface area for charge transfer and results in a large double layer capacitance and Warburg impedance. Fig. 2.20 shows a Nyquist plot of the VACNF microelectrode in 5mM glucose solution. The Nyquist plot suggests that both kinetic and diffusion processes are dominant in the VACNF microelectrodes. The model consists of a solution resistance, a double-layer capacitance, a charge transfer or polarization resistance, and a Warburg impedance. Frequencies greater than 100Hz results in a Nyquist plot resembling a Randles cell. The extracted charge transfer resistances (~Ω) and capacitance (nF) demonstrate much smaller values compared to standard platinum electrodes (~kΩ) [47]. The Nyquist plot is a diagonal line for frequencies less than 10Hz corresponding to a solution resistance of 6.92kΩ with Warburg impedance and high double layer capacitance (μF). Fig. 2.20 shows the Nyquist plots for the frequency range 1Hz to 100kHz.

A nonlinear least square fitting algorithm in the CHI660D electrochemical analyzer was used to generate the equivalent circuit model of VACNF microelectrode. The algorithm works in the following way, it requires an initial value and performs optimization for the swept frequency range. In cases where a wide frequency spectrum is involved, the algorithm results in a poor fitting due to uncertainty of an appropriate initial value. The frequency range of the amperometric device is below 10 Hz. The range of parameters for different VACNF microelectrode architectures are double layer capacitances 0.8 to 2μF, Faradaic resistances of 2-466 Ω and Warburg constant around 0.99. This works utilizes 900 VACNF forest electrode configurations. The non-planar diffusion profile of VACNF microelectrode enhances the diffusion compared to a planar electrode and thus results in increased sensitivity. The diffusion related impedance, the Warburg elements are

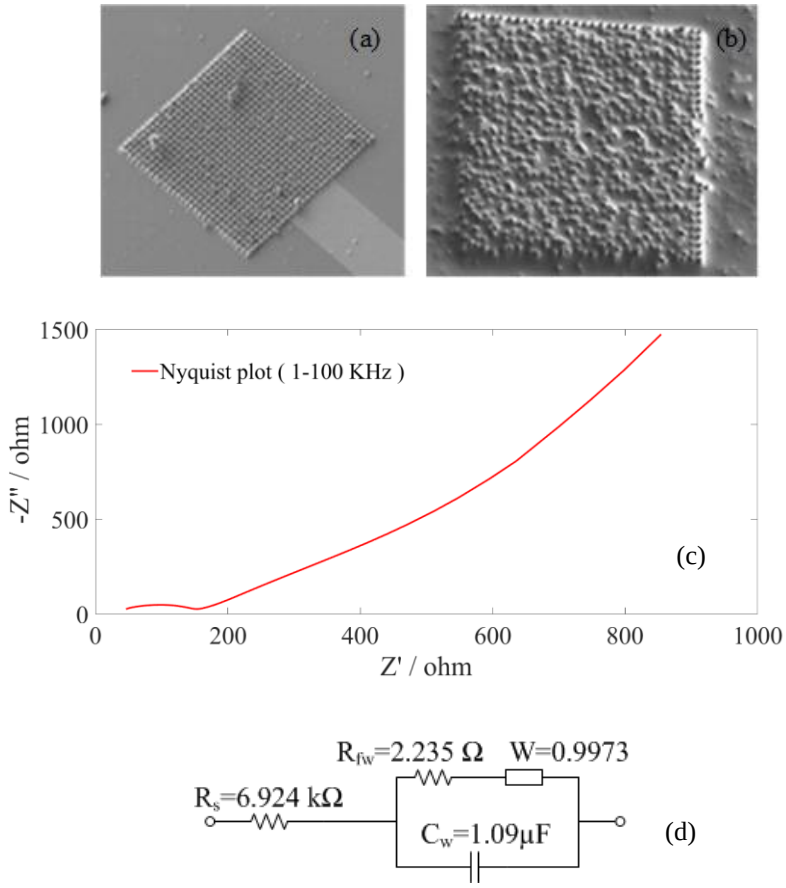

Fig. 2.20. (a) VACNF on Ti forming the working electrodes, (b) SU8 coated WE, (c) Nyquist plot of the enzyme functionalized VACNF electrode (1 to 100 kHz) and (d) electrical equivalent model of VACNF microelectrode in 5mM glucose solution.

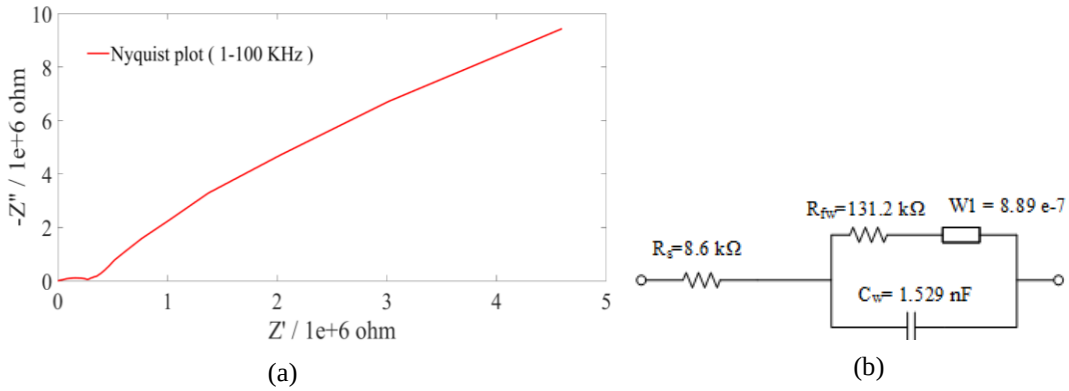

Fig. 2.21. (a) Nyquist plot of a bare Ti working electrode (1 to 100 kHz) and (b) electrical equivalent model of bare electrode in 5mM glucose solution.

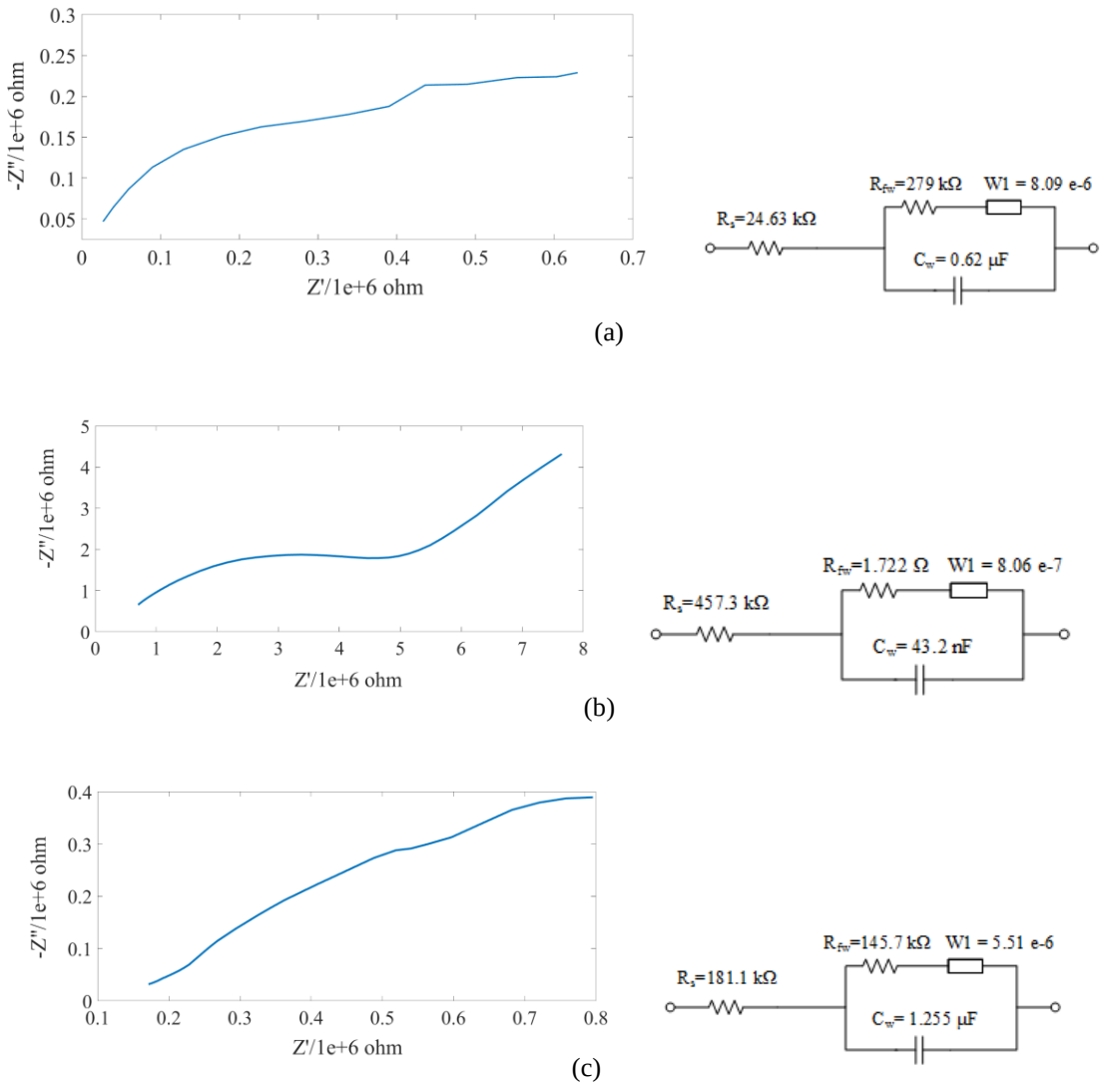

Fig. 2.22. (a) Nyquist plot of a bare Ti working electrode (0.01- 10 Hz) and electrical equivalent model of bare electrode in 2.5mM $Ru(NH_3)_6Cl_3$ solution, (b) Nyquist plot of 225 VACNF microelectrodes on Ti working electrode (0.01- 10 Hz) and electrical equivalent model of the electrode in 2.5mM $Ru(NH_3)_6Cl_3$ solution, (c) Nyquist plot of 900 VACNF microelectrodes on Ti working electrode (0.01- 10 Hz) and electrical equivalent model of the electrode in 2.5mM $Ru(NH_3)_6Cl_3$ solution.

frequency dependent and demonstrate large impedance in the Nyquist plot at the device working frequency range. The VACNF microelectrodes, thus, demonstrate very low charge transfer resistances (testing frequency <10Hz), high double-layer capacitances and act as macro-electrode in an electrochemical setup. Fig. 2.21 shows the Nyquist plot for the bare Ti electrode which demonstrates high charge transfer resistances compared to the VACNF grown Ti electrodes. The comparison of bare electrodes with the VACNF grown electrodes are shown in Fig. 2.22. The charge transfer resistance improves when 225 VACNF are grown on the Ti electrode, however 900 VACNF on the same electrode shows an increase in the charge transfer resistances. The degradation of charge transfer can be associated with the overlapping diffusion regions for the neighboring VACNF forest microelectrodes.

2.4 Electrochemical Test (Glucose Measurement)

2.4.1 Reagents

The following reagents were obtained from Sigma Aldrich and used for solution preparation without any further modification: Phosphate buffer solution (PBS), horseradish peroxidase (HRP, type VI-A), glucose oxidase (GOx, Aspergillus niger), β-D-(+)-glucose (99.5% GC), Hydrogen Peroxide (H_2O_2) solution (30% (w/w) in H_2O).

2.4.2 Electrode Functionalization

HRP and GOx were co-immobilized on the VACNF surface to functionalize the VACNF electrode for glucose sensing. 2μL of HRP and 2μL of GOx were spread over the samples and air-dried for a time period of around 10 hours. The amount of enzymes were chosen to avoid excess enzyme on the VACNF forests. The prepared biosensors were stored in a refrigerator in PBS solution at 4^{o}C.

2.4.3 Glucose Concentration Measurement

For glucose measurement, the VACNF electrode was coated with enzyme GOx and Co-enzyme HRP. GOx oxidizes glucose and produces gluconic acid with H_2O_2 as a reaction byproduct. HRP catalyzes the reduction reaction of H_2O_2. The electrons necessary for the reaction are supplied by the VACNF microelectrodes. The process is reported in detail in [48-50]. The peak current occurs at the electrode potential of -0.78V [51]. The byproduct H_2O_2 in the reaction initiates the charge transfer at the VACNF electrode with the help of the catalyst HRP and dictates the peak current potential. Fig 2.23 outlines the reaction.

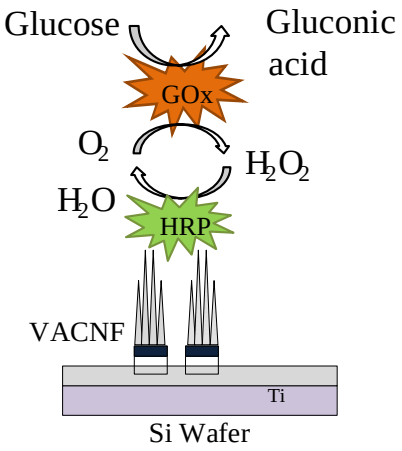

$$\text{Glucose} + O_2 \xrightarrow{GO_x} \text{Gluconic acid} + H_2O_2$$
$$H_2O_2 + 2H^+ + 2e^- \xleftrightarrow{HRP} 2H_2O$$

Fig. 2.23. Glucose kinetics on enzyme functionalized VACNF electrode [34]

In the cyclic voltammetry test of the peroxide, the peak current occurs at -0.772V (Fig. 2.24). The peroxide acts as a strong oxidizer and can initiate oxidation reaction. Thus, depending on the acidity or alkaline nature of the medium, the reaction can move in either direction. Fig. 2.25 shows the cyclic voltammetry of glucose. Fig. 2.26 shows the cathodic peak currents in multiple measurements in the PBS solution. The solutions were prepared individually by weighing glucose and mixing with Milli-Q water. Fig. 2.27 shows the

background subtracted amperometric response of the functionalized VACNF electrode for successive addition of 5 mM glucose in a PBS solution. The VACNF/GOx/HRP modified sensor platform selectivity to interfering materials has previously been verified in amperometric tests in the presence of interferers [35] where it was shown that HRP and GO_x modified VACNF biosensor demonstrate the highest response to glucose in the presence of uric acid, L-ascorbic acid and 2-acetamidophenol. The VACNF/GOx/HRP biosensor platform is thus very selective to glucose and can detect glucose from potential interferers.

2.5 Discussion

The glucose response of concentrations ranging 5mM to 20mM in VACNF electrodes have been tested, this covers the hyperglycemic range of a diabetic patient. Applicability of VACNF sensor platform for glucose concentration ranging 1mM to 5mM, corresponding to the hypoglycemic range of a diabetic patient was also verified in prior work [51]. In addition, VACNF microelectrodes were successfully employed in a previous work to detect glucose concentration in the μM range [35]. The resolution and the detection limit of the microelectrodes depend strongly on specific architecture. For sample #1(21900 VACNF forest) the sensitivity was calculated to be 89μA/mM and the highest detection limit before dominated by diffusion saturation was 40μM. For sample #2 (900 VACNF forest) the sensitivity was calculated as 35nA/mM and no highest detection limitation was observed up to 20mM concentration of glucose. The concentration range for more than 20mM is beyond the scope of medical applications. The platforms saturate at different concentrations based on the VACNF microelectrode density on the sample. Therefore for a wide operation range for glucose the microelectrode footprint design requires consideration of functional dependent parameters. Our novel contributions in this area are as follows, a comprehensive modeling of VACNF microelectrodes has been performed, a solution to achieve robust VACNF microelectrodes in the sensor platform has been proposed, verified, and utilized to develop a micro sensor for blood glucose measurement.

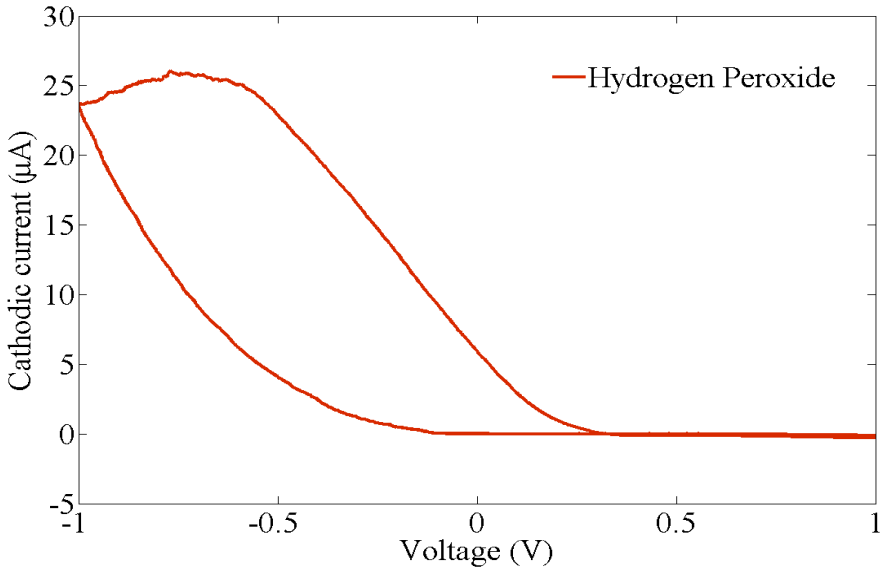

Fig. 2.24. Cyclic voltammetry plot of H_2O_2 in 0.15mM PBS [34]

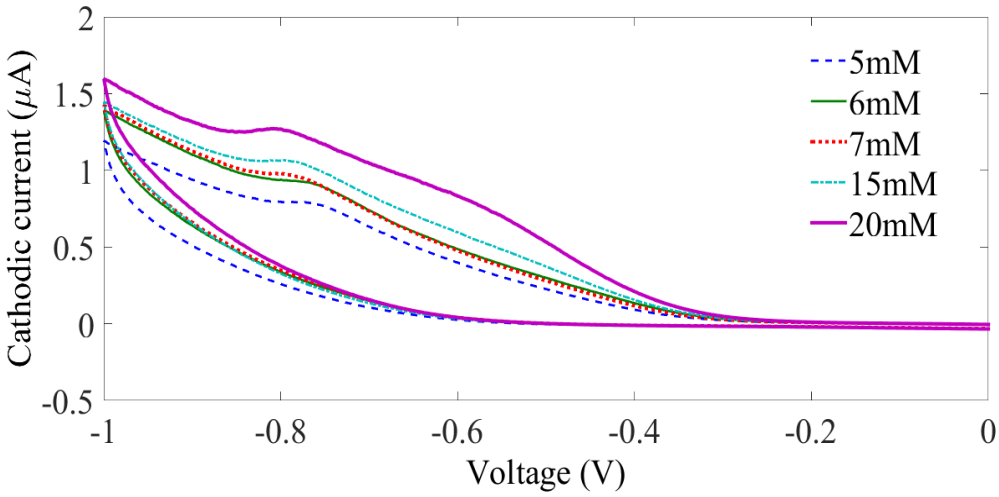

Fig. 2.25. Cyclic voltammetry plot with different glucose concentration 5, 6, 7, 15, and 20mM [34].

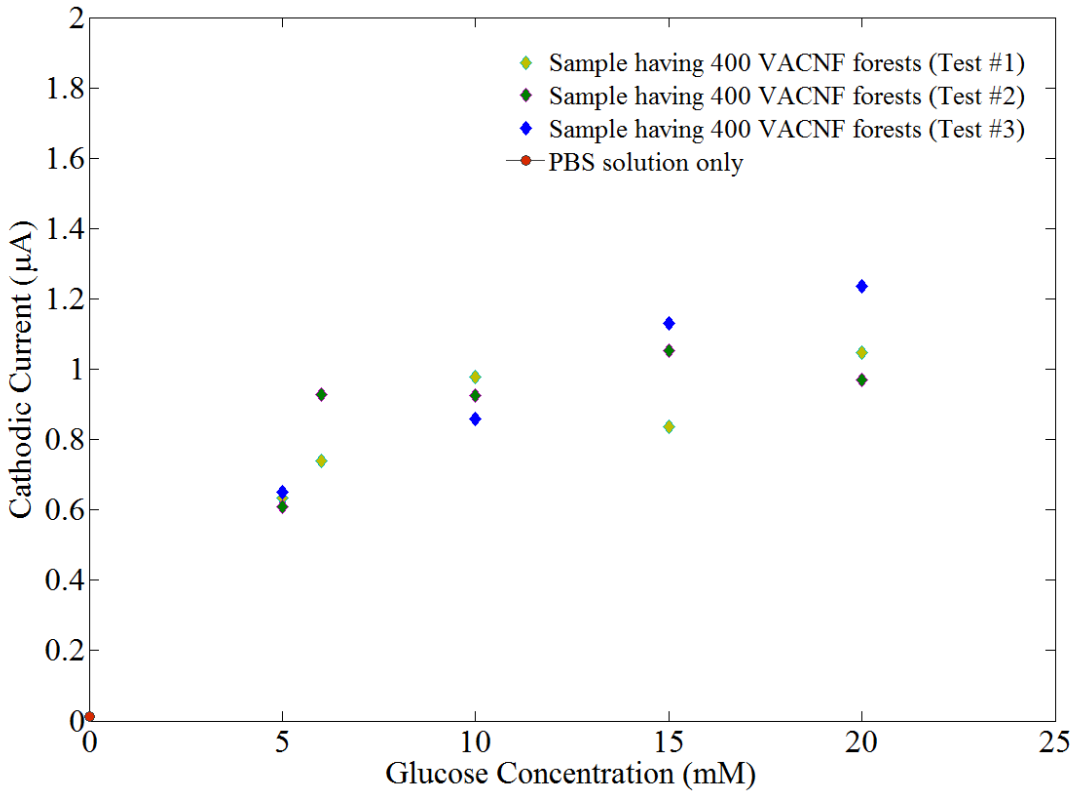

Fig. 2.26. Output current versus glucose concentration in 0.15 M PBS solution for multiple tests [34].

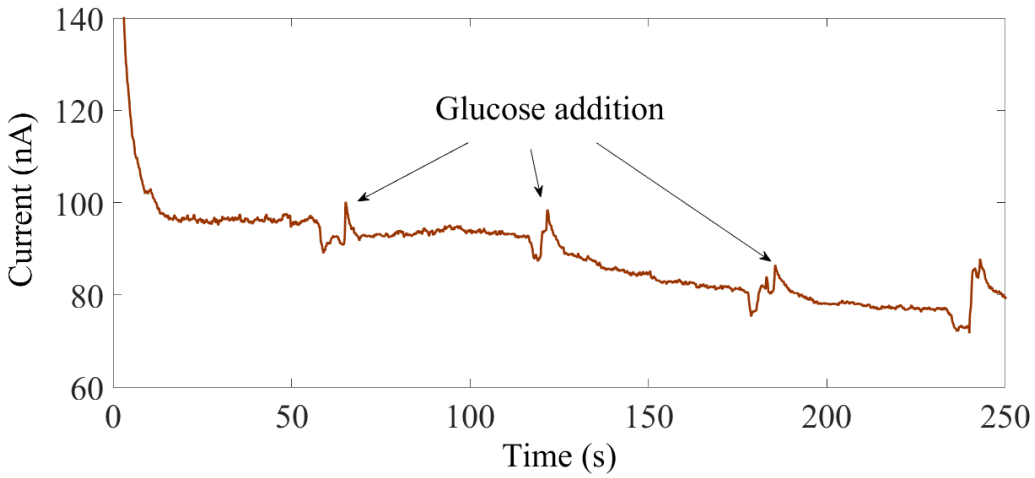

Fig. 2.27. Amperometry with 5mM glucose [34].

Note: Portions of this chapter has been published in the following articles:

[43] K. A. Al Mamun, F. S. Tulip, K. MacArthur, N. McFarlane, S. K. Islam, D. Hensley, and I. I. Kravchenko, "A robust VACNF platform for electrochemical biosensor." *IEEE Sensors Conference*, pp.1-4, 2013.

[34] K. A. Al Mamun, F. S. Tulip, K. MacArthur, N. McFarlane, S. K. Islam, and D. Hensley, "Vertically Aligned Carbon Nanofiber based Biosensor Platform for Glucose Sensor," *International Journal of High Speed Electronics and Systems*, vol. 23, no. 01n02, 2014.

[97] K. A. Al Mamun, S.K. Islam, Dale K. Hensley, N. McFarlane, "A Glucose Biosensor Using CMOS Potentiostat and Vertically Aligned Carbon Nanofibers," *IEEE Transactions on Biomedical Circuits and Systems*, 2016 (Accepted).

CHAPTER 3

LOW-POWER LOW-NOISE TRANSIMPEDANCE AMPLIFIER

3.1 Transimpedance Amplifier

A transimpedance amplifier takes an input current and converts it to a proportional output voltage. The gain of a transimpedance amplifier is the ratio between the output voltages to the input current and expressed in Ohm (Ω). Transimpedance amplifiers have been widely reported in literature and utilized to measure current from sensors. The two popular topologies of transimpedance amplifier (TIA) are (1) open loop TIA, based on common gate (CG) amplifier and (2) closed loop TIA, based on current feedback amplifiers (Fig. 3.1). Design of an open loop TIA in a low voltage process presents challenges to designers and requires considerations of the tradeoffs between amplifier noise, gain, bandwidth, rail-to-rail voltage level, and power [52-55].

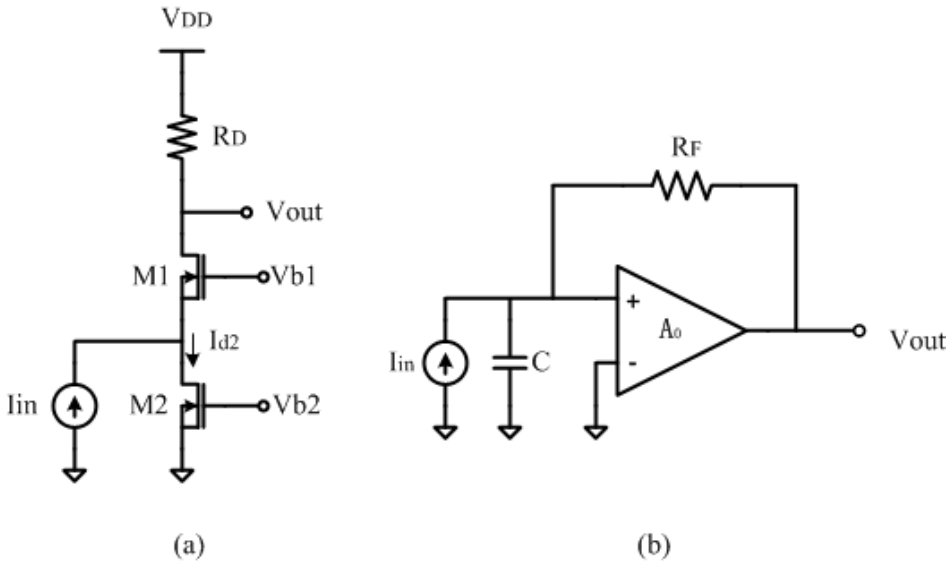

Fig. 3.1 TIA topology (a) Open loop TIA (CG stage); (b) Closed loop TIA [52]

The open loop TIA topology offer advantages of low input impedance and wide bandwidth but exhibits poor noise performance. The noise is strongly dependent on the load and

biasing current. As such, for a low noise open loop TIA, both noise sources need to be minimized. The tradeoff between the noise current and voltage headroom is evident from the following equation,

$$\frac{4kT}{In^2,R_D} + \frac{8\text{kT}\gamma}{In^2,M_2} < \frac{V_{DD}}{Id_2} \tag{6}$$

where k is the Boltzmann's constant (1.38 x 10^{-23} J K^{-1}), T is the temperature in kelvin, γ is the noise coefficient (2-3), I_n is the noise current, V_{DD} is the rail voltage, and Id_2 is the drain current. The equation demonstrates that both the noise and voltage rail cannot be decreased together without reaching the limit. On the other hand, the current feedback TIA topologies offer better performance in terms of noise, input and output resistance, and drive capability. The transimpedance gain is dependent on the feedback resistor/capacitor. The noise of the feedback branch directly couples into the input. For a low noise TIA, a very high feedback resistor and coupling capacitor is required. In a low voltage process capacitive feedback is very useful. The only caveat is that for significantly low frequencies such as sub Hz operation, typical for biological experiments, the TIA needs to have a very high dc resistance path in parallel to achieve the targeted transimpedance gain while providing large time constants (ms) to achieve a cutoff frequency less than 10kHz. Thus, capacitive or resistive feedback TIAs could cost much CMOS space. One alternative design is an open loop TIA topology which would offer less chip space for the application and improve the inherited poor noise performance in the low voltage process while consuming significantly low power.

3.2 Implementation of Low-power Low-noise Open Loop TIA

An open loop TIA topology can be implemented using a common-gate or common base amplifier. Common gate amplifiers have a flat band response even at sufficiently low frequencies (if dc coupled) but are prone to noise interferences. Low input impedance and direct coupling of load noise at the inputs are the primary causes of the poor noise performance in open loop TIA. The noise and voltage headroom constraint in an open loop TIA prohibits use of common gate topology in a low noise application in low voltage

CMOS processes. However, a low bias current and utilization of tall and wide transistors can significantly improve flicker, shot and thermal noise performances in low voltage process. The amplifier gain can be boosted using a difference input pair, and linearity of the amplifier can be improved by utilizing a differential stage. As such, the proposed open loop TIA has a difference pair common gate input stages followed by a voltage level shifter or source follower stage which feeds into a common source differential stage (Fig. 3.2). The differential stage converts the input differential voltage signals to a single ended voltage output. Thus, the amplifier takes current differences and produces a single ended voltage. Low bias current, use of difference and differential pair, tailoring of transistor sizes and operating regions improve the noise performance, suppresses substrate common mode noise and offer competitive power performances at low voltage processes.

3.3 Proposed Transimpedance Amplifier

3.3.1 TIA topology

Fig. 3.2 shows the proposed and implemented transimpedance amplifier. The TIA consists of a common gate difference input pair stage, voltage level shifter stages and a differential to single ended common-source amplifier stage. In the figure, transistors M5-M7 mirror the bias currents to the input common-gate stage. Transistors M1 and M2 act as the common gate amplifier with transistors M3 and M4 as the loads. The differences in input current signals produces a proportional voltage drops across the loads. The differential voltages produced are proportional to the load value at the first stages, which controls the gain of the first stages. The voltage level shifter formed through transistors M9-M12 couples the differential signals at the first stages to the differential amplifier stage and adjusts the output dc voltage level. The level shifter acts as source followers and shifts the dominant pole to a much higher frequency. The differential to single ended common source stages amplifies differential inputs and converts to a signal ended output voltage. The input stage bias current was chosen to be as 50nA and the transistors sizes were designed from the tradeoffs of amplifier noise contribution, power consumption, and chip real estate requirement [56]. Transistors M3 and M4 were biased in moderate inversion region,

common-gate input difference pair amplifier transistors M1 and M2 were biased in weak inversion, and the current mirrors M5-M7 and the rest of the transistors were biased in the strong inversion region.

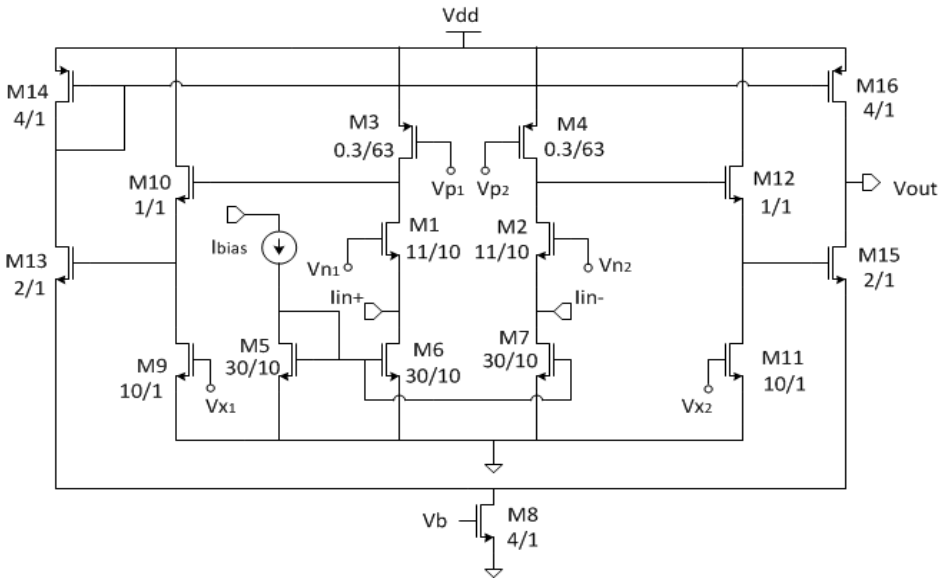

Fig. 3.2 Schematic of proposed transimpedance amplifier. Units of widths and lengths are in µm [54].

3.3.1.1 AC Small Signal Analysis

Fig. 3.3 shows the AC small signal equivalent circuit of the TIA. The elements are denoted as below, transconductances as g_m, transistor output resistances as r, net capacitances at the output of common gate and input of the source follower stage as C_1& C_2, total capacitances at the output of source follower and input of common source stages as C_3 and C_4, load capacitances as C_L and active loads as R_{ON}. The TIA gain of interest is in the low frequency region (<10Hz), as such the amplifier at low frequencies can be calculated from the following equation,

$$A_{vi} = g_{m16}\, r_{O16}\left[\frac{g_{m13}/g_{m14}}{1+g_{m13}r_{O8}}.(r_{O3}||r_{O1}).\frac{g_{m10}r_{O9}}{1+g_{m10}r_{O9}}\right] + r_{O16}\left[\frac{g_{m15}}{1+g_{m15}r_{O8}}.(r_{O4}||r_{O2}).\frac{g_{m12}r_{O11}}{1+g_{m12}r_{O11}}\right] \quad (7)$$

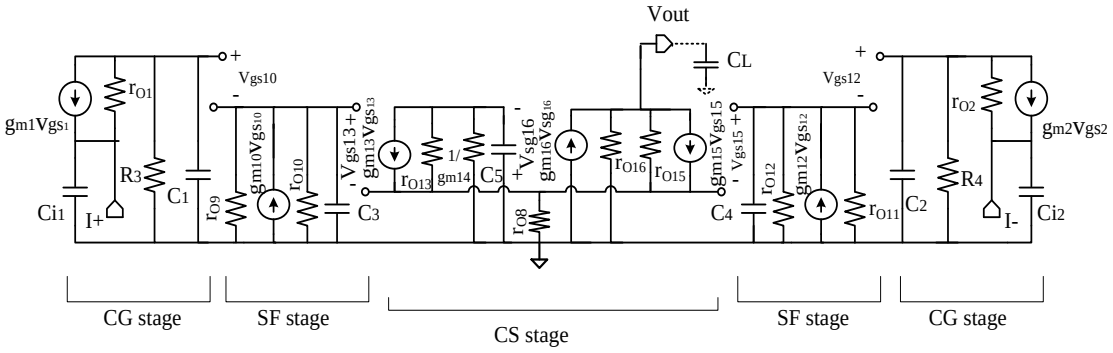

Fig. 3.2. Small signal model of the proposed Transimpedance amplifier [54]

where the transconductance of the corresponding transistors are denoted as g_m, the transistor output resistance as r_o, and the transimpedance gain of the amplifier as $A_{vi.}$ According to equation 7, the TIA gain is proportional to the transconductances of the common source differential stage, and active loads in common gate and common source stages. Thus, for a high open loop gain, the sizes of common source amplifier transistors were optimized for high transconductance and biased in the strong inversion region. The load transistors in the common gate stages were biased in moderate inversion region for the bias current, and the sizes optimized to avoid overloading the amplifier initial stage.

3.3.1.2 Noise Analysis

Flicker noise and thermal noise were considered in the noise analysis of the performance of the TIA topology. Flicker noises are the primary cause of interferences and can significantly affect the noise performances in the low frequency application. Thermal noise is a broadband noise and is strongly dependent on bias current. The input noise of the proposed TIA topology can be calculated as follows:

$$SNR = \frac{{I_f}^2}{8kT\left[\frac{2}{3}\left(g_{m6,7}+g_{Mb6,Mb2}\right)+\frac{1}{r_1}\right]+\frac{2K_f}{C_{ox.f}}\left[\frac{g_{m6,7}^2}{(WL)_{6,7}}+\frac{g_{m3,4}^2}{(WL)_{3,4}}+\frac{g_{Mb6,Mb2}^2}{(WL)_{Mb6,Mb2}}\right]} \quad (8)$$

where, W is denoted as the transistor widths, L as the transistors lengths, C_{ox} as the transistor oxide capacitances, f as frequency, K_f as the flicker noise constant, T as

temperature, k as Boltzmann's constant (1.38 x 10^{-23} J K^{-1}) and g_m as the device transconductances. Resistances r_1 and r_2 are defined as:

$$r_1 = R_{ON}||R_{in(SF)};\ r_2 = r_{9,11}||r_{10,12}||R_{in(CS)} \tag{9}$$

Where r_x is the output resistance of transistor Mx. A high transimpedance gain in the first stage is needed to reduce noise contributions of subsequent stages to the input. At low frequencies, flicker noise defines the noise spectrum, and according to equation 5 flicker noise is inversely proportional to transistor dimensions and proportional to the transconductances. Thus, tall and wide transistors can reduce flicker noise contribution and a low bias current facilitates reduction of thermal noise contribution. As such, all noise contributing transistors (M3, M4, M6, and M7) of the amplifier were designed to have large dimensions and biased with a bias current of 50nA. The bias current was chosen based on the input current range which for the application was modeled as the maximum of 2nA.

3.3.1.3 Input Impedance

Input impedance of a feedback TIA can be calculated from the following equations:

$$Z_{in} = \frac{R_F}{A(s)+1} \tag{10}$$

where Z_{in} is the input impedance, R_F is the feedback resistor, and A(s) is the open loop gain. The impedances are low at low frequencies. At high frequencies the loop gain degrades, resulting in a net increase in impedance and resembles an inductive load. On the other hand, the input impedance of the proposed TIA topology can be represented as follows,

$$Z_{in} = \frac{1}{g_{Mb1}}||\frac{1}{sC_{in}} \tag{11}$$

where g_{Mb1} is the transconductance of transistor Mb1 (Fig. 3.2) and C_{in} is the net capacitances at the gate. The input impedance dependence on the frequency can be written as,

$$As\ s \to 0, Z_{in} \approx \frac{1}{g_{Mb1}}\ and\ s \to \infty, Z_{in} \approx 0 \tag{12}$$

The input impedance decreases as the frequency increases. The TIA acts as a capacitive load to the sensors.

3.3.1.4 Spurious Free Dynamic Range

The amplifier linearity and distortion performance can be formulated with spurious free dynamic range and using the following equations:

$$V_{out}{}^{+} = \sum_{n=1}^{\infty} k_n \, I_{in}{}^{n}$$

$$V_{out}{}^{-} = \sum_{n=1}^{\infty} k_n \, (-I_{in})^{n} \tag{13}$$

$$V_{out\,(difference-differential)} = V_{out}{}^{+} - V_{out}{}^{-} = \sum_{n=1,odd}^{\infty} k_n \, I_{in}{}^{n}$$

$$V_{out\,(single-ended)} = \sum_{n=1}^{\infty} k_n \, I_{in}{}^{n}$$

where V_{out+} denotes the output due to the positive input current, V_{out-} denotes the output due to the negative input current, $V_{out(difference-differential)}$ denotes the net output of the difference-differential TIA topology, and $V_{out(single-ended)}$ represents the output of a single ended TIA topology. According to equation 8, the difference-differential amplifier can suppress even harmonics, provide better dynamic performance compared to a single ended potentiostat structure and thus extends SFDR to a much higher value.

3.3.1.5 Simulation and Measured Results

The proposed TIA topology was implemented in a standard 180nm, 6 metal, 1 poly CMOS process. Simulation results of the first version of the proposed topology demonstrates that the TIA can produce a transimpedance gain of 215MΩ, 3dB bandwidth of 642kHz, and gives phase shift less than 10^{o} up to 100kHz and 75^{o} at 1MHz [57]. A 10pF of capacitive load degrades the amplifier bandwidth to 60kHz (Fig. 3.3(a)). The input referred noise current (IRNC) is calculated by dividing the output noise spectrum by the midband transimpedance gain. The calculated IRNC is 112fA/√Hz at 20 kHz and 910fA/√Hz at 100Hz (Fig. 3.3(b)). The transimpedance amplifier consumes

139μW of dc power. The TIA has a linear operating range of 0 to 2.25nA (Fig. 3.4). The CMRR of the amplifier is 42dB, and is calculated as a change in output voltage with the change in common mode current. The level shifter and the common source differential amplifiers were fabricated and tested for functional verification. The simulated and test results are shown in Fig. 3.5. Measured results demonstrated voltage gain of 29.20dB, 3dB frequency of 58kHz which agrees well with the simulated results, voltage gain of 31.49dB, 3dB frequency of 60kHz. The analysis of amplifier suggests that the dominant pole of the topology is located at the output of the differential stage. An output buffer stage thus needed for increased the driving capability and wide band frequency response in this topology.

Open loop TIA topology performances are prone to process related variations. The effects of mismatches (variation of transistor threshold, body effect, and other parameters) and process variations (chip to chip variation in mobility, velocity saturation, early voltage and temperature dependence) on the TIA topology were analyzed by Monte Carlo simulation with 1000 random samples. The statistical plot in Fig. 3.6 shows the TIA performance as a function of systemic process variations and transistor mismatch. 78% of the samples show gain within 1σ and 99% of the samples show bandwidth within 1σ variations. The target biosignal measuring application requires measurements frequencies below 10 Hz, thus the proposed TIA topology can still satisfy the requirements with variations. A comprehensive study of both process variations and device mismatch was performed, and it is observed that when considering the net effects of both a mean gain of 195MΩ with a standard deviation of σ=64 and 3dB bandwidth of 94 kHz with a standard deviation of σ=67 resulted (Fig. 3.6). However, when only the process variation was considered a mean gain of 234MΩ with a standard deviation of σ=35 and mean 3dB bandwidth of 100 kHz with the standard deviation of σ=5 resulted. Thus, it is evident that Monte Carlo plots that the lower tail gain part and upper tail 3dB parts resulted from transistor mismatches. Adopting interleaving and common centroid layout techniques can significantly improve this TIA performance.

(a)

(b)

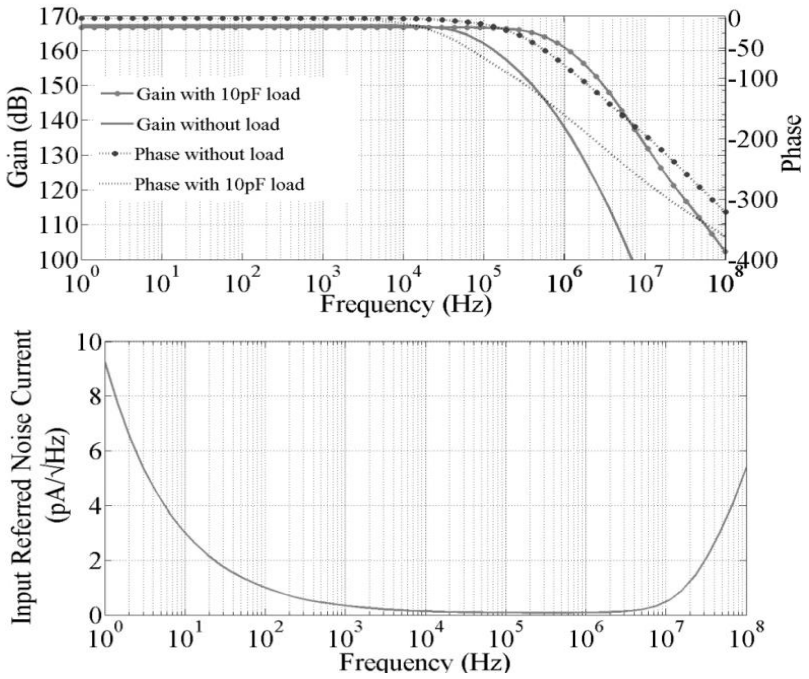

Fig. 3.3. Simulation result (a) AC gain and phase response of TIA, (b) Input referred noise current of the TIA [54].

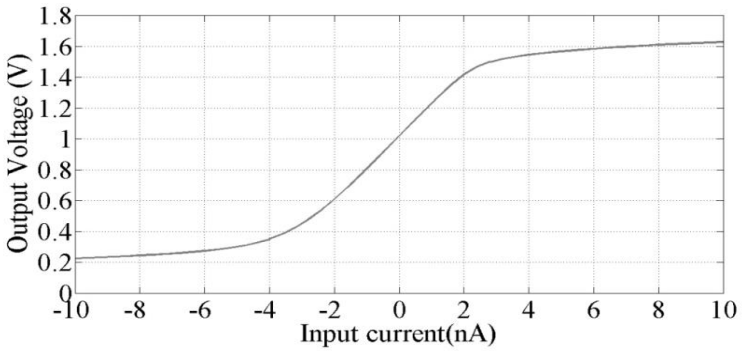

Fig. 3.4 Simulated DC transfer curve of the amplifier [54].

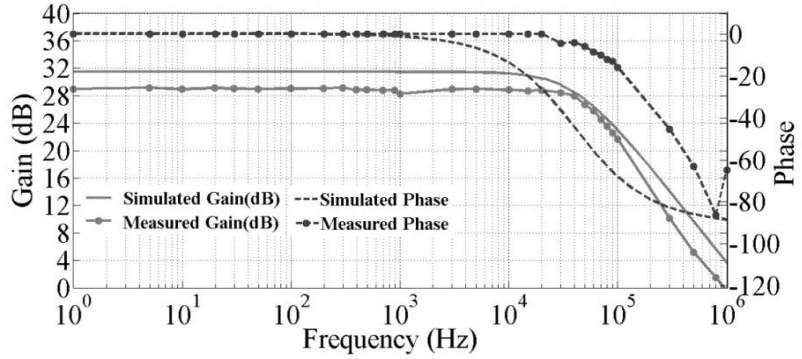

Fig. 3.5. Source follower and common source outer stage ac response comparison [54].

3.3.2 Optimization of the TIA Topology

There always exist certain tradeoffs among amplifier power, gain-bandwidth, noise, and input and output dynamic range. The first version of the TIA was optimized for high gain and ultra-low noise for the input dynamic range of pA to 2nA ionic currents, while the second version was optimized for low power and a higher input dynamic range of 200nA to 5µA. The target application for version 2 was to enable integration with micro-fabricated VACNF microelectrodes for a Lab-on-a-chip sensing system consisting of an on-chip potentiostat and RF transmitter. Based on the VACNF modeling data and electrochemical characterization results, the following specifications were targeted for the sensor platform. The specifications are as follows, the electrochemical current swing can be as small as tens of nA to 5µA with a dc background currents of 3µA and the electrode capacitances can be as large as 100µF. The potentiostat need to regulate a potential of 0.78V at the working electrode and should produce a rail to rail output swing for the maximum electrochemical input current when coupled with a VCO.

3.3.2.1 Optimized TIA Structure

The TIA structure was optimized for power and the input dynamic range utilizing the inversion coefficient method [56]. The common-gate input differential pair was optimized for noise, low power, and compact layout area while maintaining a high gain to reduce following stage noise contribution. Equation (5) suggests that flicker noise dominates the overall noise performances at low frequencies and needs to be minimized by increasing M6, M7, M3 and M4 transistor dimensions. High $r_{o3}||r_{o1}$, $r_{o4}||r_{o2}$ and r_{o16} will give a high gain. Since first stages need optimization for low noise and gain, the current sources (M5-M7) were biased in strong inversion region (inversion coefficient, IC = 15 with an aspect ratio W/L = 5.3/5) and loads (M3, M4) were biased in deep strong inversion region (IC = 50) with aspect ratio W/L = 1/0.95. Strong inversion region gives the highest transistor output resistance in the design plane, while moderate inversion region gives good noise performance and minimizes layout area. A high g_m value can lower the TIA input impedance.

(a)

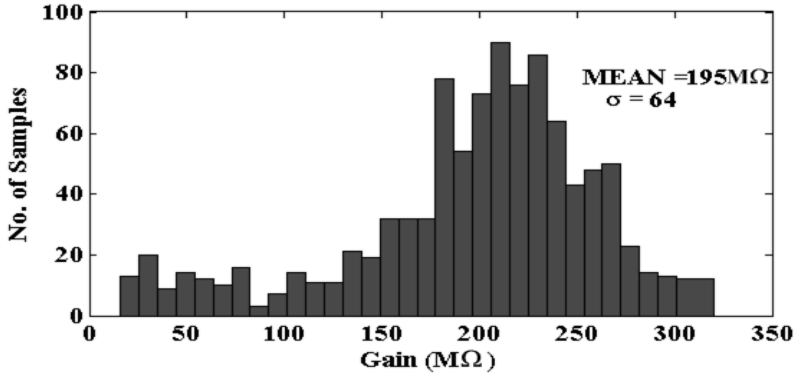

(b)

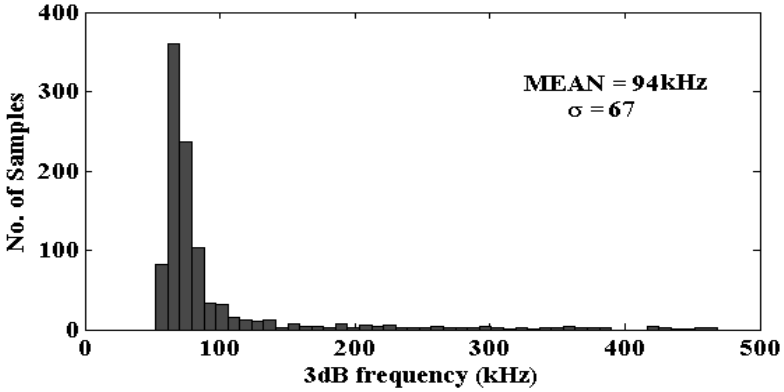

Fig. 3.6. MonteCarlo simulation results of the TIA structure (a) histogram for gain and (b) -3dB bandwidth. [54].

Table 3.1. Specifications for transimpedance amplifier in the sensor platform:

Parameter	**Approximate Requirements**	**TIA (Version 2)**
Gain	~500K	641K
Bandwidth	<1KHz	8.1kHz (10pF load)
Lower cutoff frequency	<1Hz	<1Hz
Background current	~100nA	Bias Current: 10μA(can withstand background current upto 1μA)
Dynamic Range	500nA~1.6μA	200nA~5μA
Power	<100μW	47.4μW

Biasing the common gate input pair M1, M2 in weak inversion region (IC = 0.1, W/L = 70/0.45) allows for the highest transconductance efficiency and g_m for the bias current. The DC mismatch between the transistors can create a DC offset. However, the mismatch is minimized when transistors operate in weak inversion. The low V_{ds} in weak inversion enhances the dynamic range for the signal in low voltage processes. The differential to single ended stage (M8, M13-M16) needs optimization for power, layout area, and output swing, and hence the transistors were biased in moderate inversion region. The transistors inversion coefficient and dimensions for version 2 are as follows: M8: IC = 3, W/L = 10/20; M13, M15: IC = 0.2, W/L = 4/1; M14, M16 : IC = 0.2, W/L = 2.52/10. The level shifters transistors were biased in strong inversion region with the IC and dimensions M9-M12: IC = 15, W/L = 2.67/50 to achieve a high drain source resistance. The current mirror consisting of transistors M_{b1}-M_{b5} were optimized for strong inversion region (Mb1-Mb3, IC = 30, W/L = 2.66/10 and Mb4-Mb5, IC = 30, W/L = 12.6/10). The optimized TIA structure is shown in Fig. 3.7.

3.3.2.2 Simulation and Test Results

Simulation results of the optimized topology demonstrates that the TIA has a DC gain of 641KΩ , 3dB bandwidth of 8.1KHz and phase shift less than 10^o up to 3KHz with a 10pF load capacitor [58]. The input referred noise current (IRNC) is calculated by dividing the output noise by the midband gain and the IRNC is 50.3pA/√Hz at 100Hz. The amplifier consumes 47.4μW power during operation. The TIA was fabricated in a 0.18μm commercially available CMOS process and tested using a SR785 dynamic spectrum analyzer and SR770 FFT network analyzer. Fig. 3.8 shows the measured bode plots of the amplifier gain and phase responses. The TIA demonstrates 92dBΩ gain and phase difference of less than 1^o up to 5 kHz. From the measured noise spectrum (Fig. 3.9), it is evident that the noise at 1Hz is 8.1nA/√Hz. The integrated noise is 0.69μA over the equivalent noise bandwidth of 12.72kHz. However, the rate of change in the glucose concentration is well below 1Hz, thus inclusion of a low pass filter using an off-chip capacitor filter out noise above 10Hz and gives an integrated noise value of 71.8nA. The measured transfer characteristics of 4 fabricated chips are shown in Fig. 3.10. The voltage

transfer characteristics show variations over process and could be due to the open loop TIA topology. The amplifier thus requires calibration before any practical use. The amplifier demonstrates a linear range from 500nA to 7μA. FFT analysis has been performed with a 10mV signal of 500Hz. At the operating region of the TIA measured fundamental power spectral density (PSD) was -48.75dBV while the nearest strongest harmonic PSD was -89.37dBV. Thus, the measured spurious free dynamic range (SFDR) was calculated as 40.63dB (Fig. 3.11). The high SFDR demonstrates that the TIA produces low distortions for the input dynamic range (200nA-5μA). Fig. 3.12 and Fig. 3.13 show the microphotograph of the TIA and the cadence layout of the TIA.

3.3.3 Comparison with Prior Art

The performance of the proposed transimpedance amplifiers are compared with prior arts in Table 3.2. The proposed transimpedance amplifier topology offer ultra low current detection sensitivity and improved noise performance at low power.

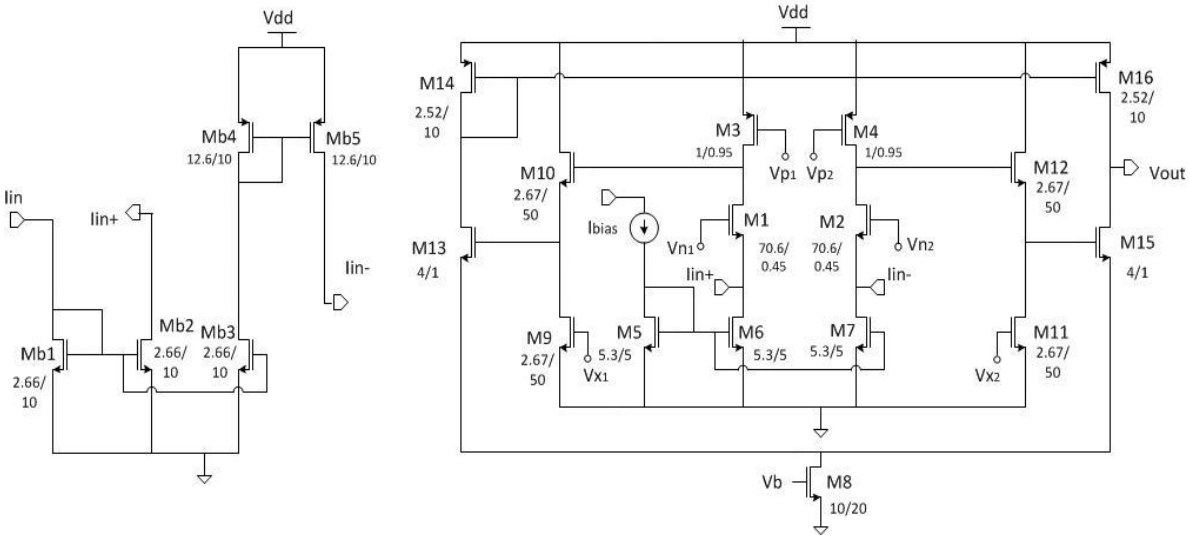

Fig. 3.7. Optimized low power TIA structure [58]

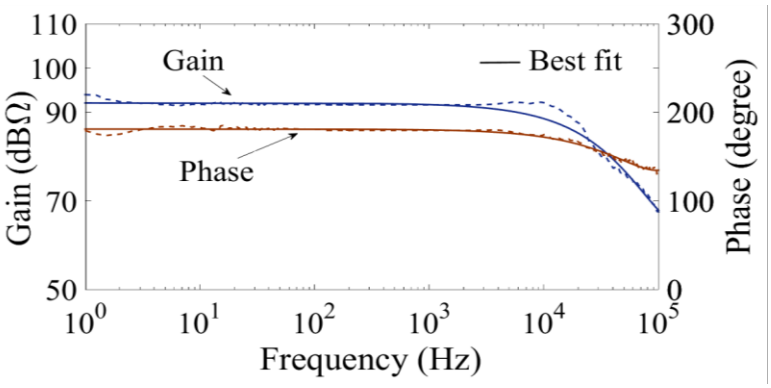

Fig. 3.8. (a) Measured gain and (b) Phase response of the current measuring unit (difference-differential pair TIA) [97].

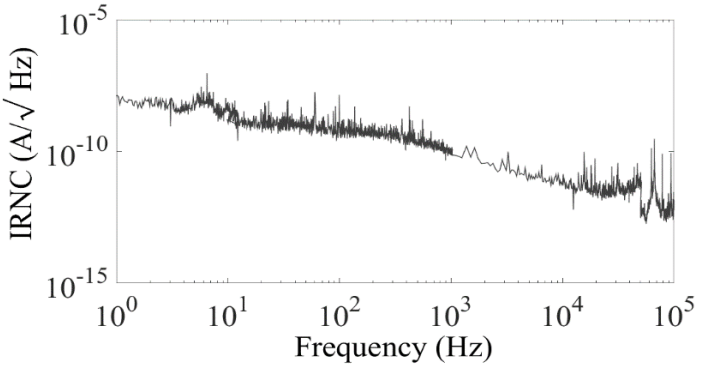

Fig. 3.9. Measured input referred noise current (IRNC) spectrum of the difference-differential pair TIA [97].

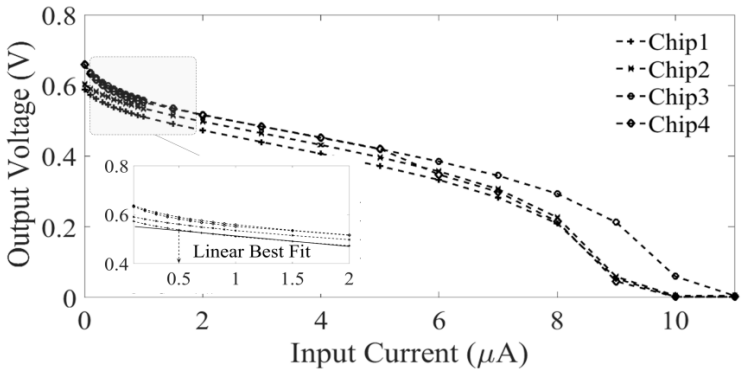

Fig. 3.10. Transfer characteristics of the current measuring unit (TIA), Linear Best fit plot for 0.1-2μA region (inset).

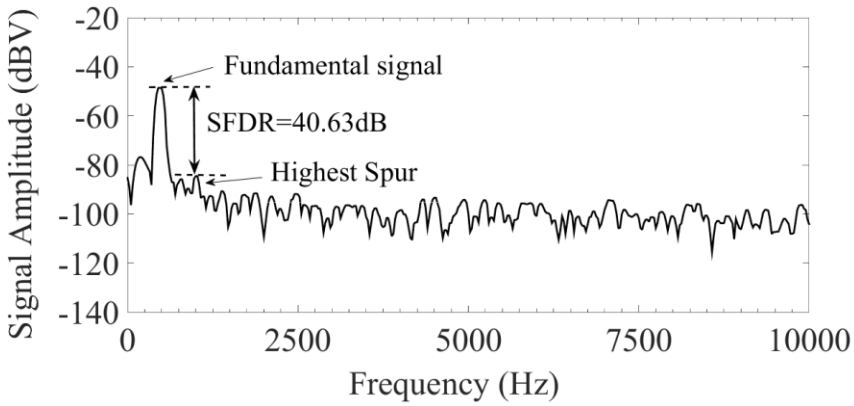

Fig. 3.11. FFT of the output signal of the current measuring unit (TIA) [97].

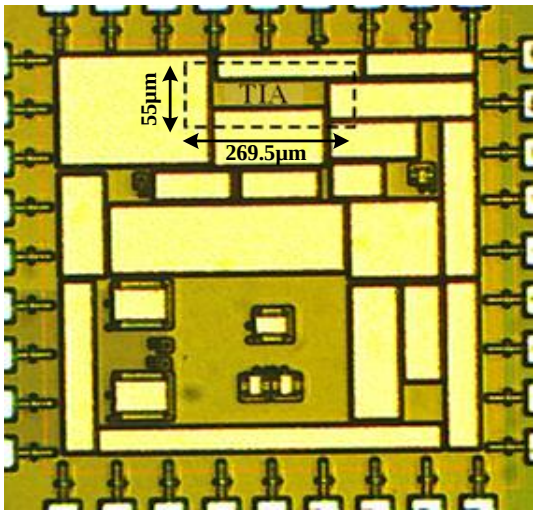

Fig. 3.12 Chip microphotograph of the TIA.

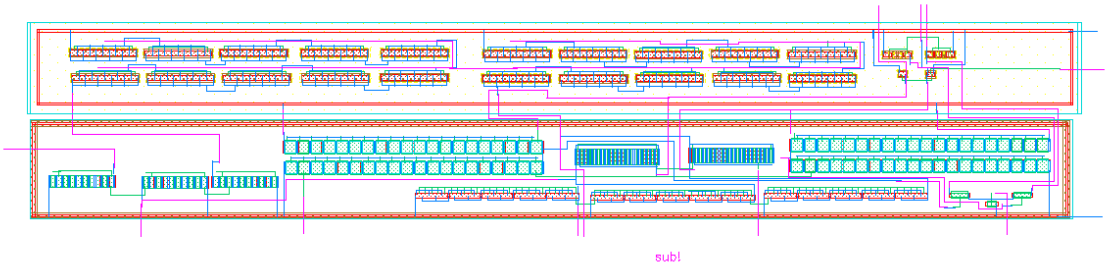

Fig. 3.13 Layout of the TIA.

Table 3.2. Comparison of performance of TIA topologies

Parameter	**[53]**	**[54]**	**[55]**	**Version 1**	**Version 2**
Application	Biosensor	MEMS	Biosensor	Biosensor	Biosensor
Technology	0.35µm CMOS	0.18µm CMOS	0.18µm CMOS	0.18µm CMOS	0.18µm CMOS
Topology	Integrator-differentiator	Capacitive feedback	Capacitive feedback	Difference-differential	Difference-differential
Supply	3.3	1.8V	1.8V	1.8V	1.8V
Midband Gain	30M	56M	100M	215M	641K
Bandwidth	2MHz	1.8MHz	1MHz	615kHz/ 60kHz(10pF load)	285kHz/8.1kHz (10pF load)
GBW	60	100.8	100	132.2	0.182
Lower cutoff frequency	100Hz	1kHz	40Hz	1Hz	1Hz
Input Referred Noise Current	4fA/√Hz @100Hz	250fA/√Hz @1KHz	1100fA/ √Hz @ 100Hz	910fA/√Hz @100Hz	50.3 pA/√Hz @100Hz
Integrated Input Referred Noise**	28.24pA*	99.52pA*	318.49pA*	95.08pA	127nA
Dynamic Range	-	-	-	200pA to 2nA	200nA to 5µA
Power	21mW	436µW	132µW	139µW	47.4µW

* Input referred noise plot is available from lower cutoff frequency

**Integrated noise is calculated over respective noise equivalent band from the Input referred noise plot.

For cases (*), integration carried out from lower cutoff to noise band which might underestimate the overall integrated noise.

3.4 Discussion

In this chapter we have demonstrated a novel difference-differential transimpedance amplifier topology to detect ultra low currents with improved noise performance and increased linearity at low power. Version 1 detects currents from 200pA to 2nA and consumes 139μW of power. Version 2 is optimized for VACNF based glucose sensors and detects currents from 200nA to 5μA while consuming 47.4μW of power. This TIA topology offers implementation in the smallest chip space and is suitable for low power biosensing applications.

Note: Portions of this chapter has been published in following articles:

[57] K. A. Al Mamun, M. H. U. Habib, and N. McFarlane, "A low-power low-noise transimpedance amplifier for an integrated biosensing platform," *IEEE International Midwest Symposium on Circuits and Systems*, pp. 161-164, 2013.

[58] K. A. Al Mamun, and N. McFarlane, "A CMOS potentiostatic glucose monitoring system for VACNF amperometric biosensors," *IEEE International Symposium on Circuits and Systems*, pp. 477-480, 2015.

[97] K. A. Al Mamun, S.K. Islam, Dale K. Hensley, N. McFarlane, "A Glucose Biosensor Using CMOS Potentiostat and Vertically Aligned Carbon Nanofibers," *IEEE Transactions on Biomedical Circuits and Systems*, 2016 (Accepted).

CHAPTER 4
CMOS POTENTIOSTAT FOR GLUCOSE MONITORING

4.1 CMOS Potentiostat

Potentiostat circuits have been long utilized in enzymatic glucose monitoring systems. Potentiostats can be utilized for constant voltage amperometry, cyclic voltammetry or impedance spectroscopy [59-67]. In constant voltage amperometry a fixed voltage difference is maintained between the working and reference electrode to enable the action potential in the electrochemical reaction. Among the various potentiostat topologies reported, the grounded working electrode potentiostat topology is a popular choice for amperometry (Fig. 4.1). However, studies have indicated that the topology is prone to instability [60, 62]. One alternative topology keeps the counter electrode at ground potential [60]. Another approach reported uses compensating networks to stabilize the potentiostat [62]. Since glucose sensors utilize the reduction of H_2O_2 on the electrode surface, the working electrodes must maintain a negative potential with respect to the reference electrode. Thus, the use of a grounded counter electrode in a potentiostat for amperometric glucose sensors is limited. In the potentiostat current measuring unit transimpedance amplifiers (TIA) are typically utilized to measure the sensor current. In the topologies where the working electrode directly feed the current measuring unit, coupling of noise interference and measuring unit stability is greatly compromised. Potentiostat topologies which uses current mirrors to isolate the direct loading of sensor current can significantly improve the potentiostat stability. Input and output dynamic range of a potentiostat is a key metric to compare potentiostat implementation efficiency in a certain CMOS processes. Single ended and fully differential potentiostat topologies has been reported where the fully differential potentiostat topologies demonstrate improved input and output dynamic range compared to a single-ended potentiostat, and thus enable implementation in a low voltage process [63, 68-70]. For sensitive measurements, potentiostat current measuring units utilize capacitor charging time, sigma-delta or semi-synchronous sigma-delta ADC to achieve current sensitivity in the range of pico to femto

amperes [61, 71, 72]. In current mirror based potentiostat several techniques have been proposed to improve the linearity errors using error cancellation loop or compensation networks [73, 74]. These potentiostats can offer a wide dynamic range, improved sensitivity but demand increased power (mW) and chip real estate (60,000μm^2) [61, 72, 75, 76]. In a portable Lab-on-a-chip sensing systems, the importance of power and area-efficient implementation has been established. Several low power and compact potentiostat topologies have been reported using bulk driven amplifier, amplifier sharing and feedback or resistive TIA in current measuring blocks [77, 78]. The drawback of these structures is they are power intensive and consume a large chip space which forbids implementation in a compact power starving systems such as the lab-on-a-chip or implantable devices.

4.2 Proposed Potentiostat

In amperometry, the potentiostat circuits typically use three electrodes, working electrode (WE), auxiliary or counter electrode (AE/CE), and reference electrode (RE). The working electrode is functionalized with enzymes. The electrochemical reaction occurs at the functionalized electrode when a constant potential difference is maintained between the reference and the working electrodes. The current source/sink from the working electrode is supplied by the counter electrode, and thus the reference electrode can maintain a fixed potential throughout the reaction process. In the proposed glucose sensing system, VACNFs act as the working electrode, while a standard Ag/AgCl electrode is used as the reference and counter electrodes (Fig. 4.2). The potentiostat circuit consists of two major units, (1) the potential control unit and (2) the current measuring unit with a frequency translator for data transmitter. In this thesis two types of potential control unit have been studied, an amplifier based potential control unit and a current regulator based potential control unit. The sensor current is coupled to the TIA through a current mirror. The current mirror aids in restraining the working electrode to directly load the TIA and reduces sensor induced interferences by providing an impedance path to ground. The counter electrode is connected to the control amplifier output in case of amplifier based control unit or with the transistor drain in regulator based control unit. The reference electrodes are connected at

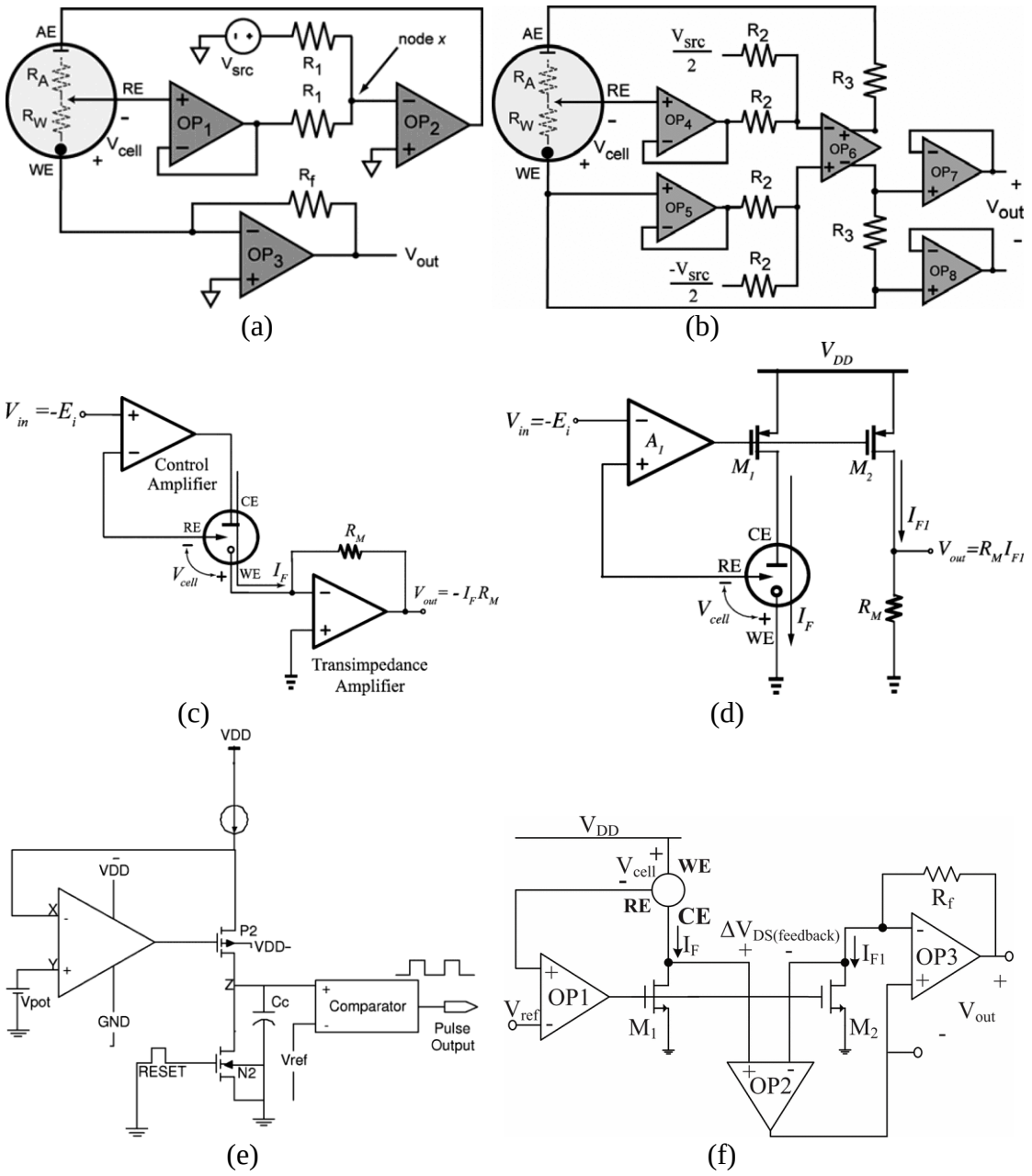

Fig. 4.1. CMOS potentiostat topologies (a) Single ended potentiostat, (b) fully differential potentiostat, (c) current mirror potentiostat with grounded WE, (d) low-power current mirror potentiostat, (e) VLSI potentiostat, (f) highly accurate potentiostat [59-67].

the input of a voltage buffer or directly tied with the positive rail in case of regulator based control unit. A difference common-gate input pair differential TIA follows the potential control unit and converts electrochemical current to voltages. A 5 stage current starved VCO converts the voltages to frequencies.

4.2.1 Potential Control Unit

The potential control unit in the potentiostat regulates and maintains a constant reference to the working electrode potential. The counter electrode sources or sinks current as needed to maintain the potential. In the VACNF microelectrode electrochemical cell model, R_{S1} and R_{S2} denotes the solution resistances, R_{fw} denotes the faradaic resistance of the working electrode, R_{fc} represents the faradaic resistance of the counter electrode, C_W as the total (double layer and specific) capacitance of the working electrode, C_C as the double layer capacitance of the counter electrode, $Z_{RE\text{-}CE}$ represents the net impedance in between the counter and reference electrodes, and $Z_{RE\text{-}WE}$ represents the net impedance in between the reference and working electrodes. The impedances are expressed as follows:

$$Z_{CE-RE} = R_{S1} + \left(R_{fc} || \frac{1}{sC_c}\right)$$
$$Z_{RE-WE} = R_{S2} + \left(R_{fw} || \frac{1}{sC_w}\right) \quad (14)$$

where $R_{fw} >> R_{fc} >> R_{S1} \& R_{S2}$, and $C_W >> C_C$. Faradaic resistances have greater effects on net impedances at low frequencies while double-layer capacitances dominate at high frequencies. The working principle of the amplifier based single-ended potential control unit (Fig. 4.3(a)) can be expressed with following equation as in [63],

$$\frac{V_{RE-WE}}{V_{ctrl}} = \frac{A_2 Z_{RE-WE}}{A_2 Z_{RE-WE} + 2(Z_{RE-WE} + Z_{CE-RE})} \quad (15)$$

where $V_{RE\text{-}WE}$ denotes the voltage across the reference and working electrodes, $V_{CE\text{-}RE}$ is the voltage across the counter and the reference electrodes, A_2 represents amplifier open loop gain, and V_{ctrl} denotes the control voltage. $V_{RE\text{-}WE}$ tracks the control voltage V_{ctrl} when A_2 is sufficiently high. In Fig. 4.3(a) the amplifier based control unit amplifier, A_2, controls

the feedback current while the voltage follower formed with the amplifier A_1 maintains a high impedance at the reference electrode. The counter electrode helps maintain the constant reference and working electrode potential by supplying the currents necessary for the electrochemical reactions to the working electrode. The disadvantage of using the amplifier based control unit is that at high reaction currents the coupling current mirror can show non-linear response and thus limit the detection accuracy. A current regulator based potential control topology can be used to circumvent the issue (Fig. 4.3(b)). In the current regulator topology the working electrode potential is regulated using a feedback loop while the RE is tied with the positive rail. As both voltages are well regulated the potential difference is well regulated with this topology. The CE is connected with the drain terminal of the transistor. A folded cascade topology (Fig. 4.3(c)) was used for the amplifiers A1, A2. The transistor sizes of the current mirror and the folded cascode amplifiers are as follows, Mb1, Mb2, Mb3= 2.66 μm /10 μm and Mb4,Mb5=12.6μm/10μm, M6,M7= 10μm/5μm; M1,M3=5μm/5μm; M2,M4= 1.92μm/1μm; M5=3.84μm/1μm; M8= 10μm/1.5μm; M4,M16=20μm/1.5μm; M9 =6.88μm/0.75μm; M15,M17=16μm/0.75μm; M11, M13= 3μm/2μm; M10, M12 =1μm/1μm, and M18,M19=3μm/10μm.

4.2.2 Current Measuring Unit

Fig. 4.2 shows the general overview of a VACNF based glucose monitoring system where a CMOS potentiostat unit with a difference-differential transimpedance amplifier acts as the sensor frontend and a current starved voltage controlled oscillator provides the voltage to frequency conversion needed for wireless transmission of the sensor signal [58]. A difference-differential TIA has been proposed and designed for current measurement. A current mirror converts the current to a differential currents and feeds into the difference-differential TIA stage.

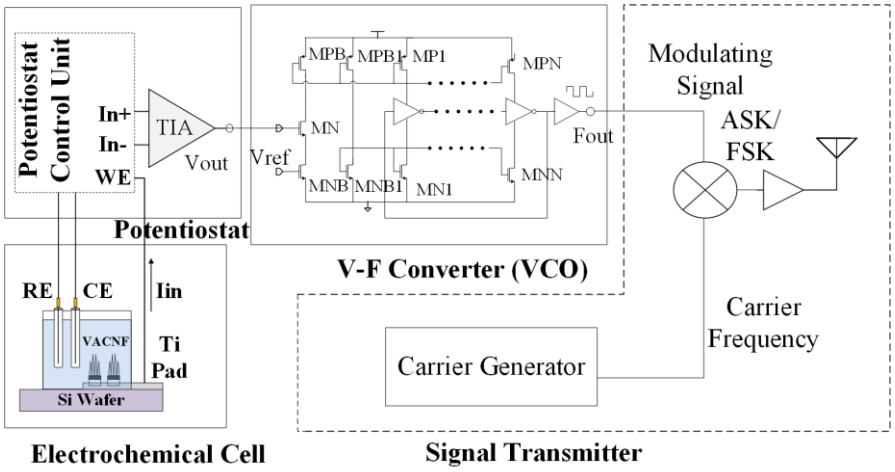

Fig. 4.2. General overview of the CMOS potentiostat based amperometric glucose monitoring system.

The proposed current measuring unit has several advantages over traditional structures. First, the inductive nature of feedback TIA can be suppressed using an open loop TIA structure, Second, satisfactory CMRR and SFDR for the application is achievable at low power when a difference–differential topology is used. Common mode feedback circuits are not necessary in this design, and thus the power and chip space can be significantly reduced. Third, through prior experiments VACNF microelectrodes demonstrate that a constant cell potential of 0.78V is required for glucose reduction [34]. A 1V dynamic range potentiostat can achieve the voltage swing for the sensing application. Fourth, a traditional current feedback TIA requires large feedback resistances and capacitances to achieve satisfactory noise performance [52]. The proposed TIA topology provides a low noise front end while relaxing the requirements for large feedback resistances or capacitances. Fifth, the capability of suppressing even harmonics components of a signal in differential structure is added in the open loop TIA topology to improve TIA linearity. The transimpedance amplifier needs to be highly linear within the dynamic range of the sensor. From the experimental measurements (Chapter 2), background currents of 100nA to 3μA flow through the sensor with VACNF microelectrode sensitivities 50nA to 200nA/mM which is based on the number of microelectrodes on a sample. Since VACNF sensor sensitivity can be tailored utilizing varying number of VACNF microelectrodes in a

sample, the TIA gain is not a limiting factor when integrated with the VACNF microelectrodes.

4.2.2.1 Low Power Low Noise TIA Implementation

The difference-differential pair transimpedance amplifier utilized in the potentiostat current measuring unit is shown in Fig. 3.8. The first stage is a common gate difference pair which is formed with transistors M1-M7. As the VACNF amperometric sensor can have background currents as high as 3μA, the amplifier first stage was biased with a current source which is at least 3 times the input current. For the particular design a bias current of 10μA was chosen. The outermost stage is a differential stage comprised of transistors M8, M13-M16 and is connected to the input difference stage through a level shifter pair consisting of transistors M9-M12. The net power consumption of the structure can be expressed as: $P = V_{dd}.(2I_{bias} + 2I_{SF} + I_{tail})$, where I_{bias} is the first stage bias current, I_{SF} is the bias current of the level shifter, and I_{tail} is total current of the outer differential stage. To keep the net power consumption low the outer differential stage was biased with much lower current (500nA) compared to the first stage. Corruption of the electrochemical signal by interfering noise sources can limit the use of a potentiostat in sensing application. The signal-to-noise ratio (SNR) is a measure of potentiostat immunity to noise sources. The SNR of the proposed potentiostat can be expressed as:

$$SNR = \frac{{I_f}^2}{8kT\left[\frac{2}{3}g_{m6,7}+\frac{1}{r_1}\right]+\frac{2K_f}{C_{ox.f}}\left[\frac{g_{m6,7}^2}{(WL)_{6,7}}+\frac{g_{m3,4}^2}{(WL)_{3,4}}\right]} \quad (16)$$

where, I_f is the electrochemical current, W and L are the width and length of the transistor, C_{ox} is the oxide capacitance, f is the frequency, K_f is the process dependent flicker noise constant, T is temperature, k is Boltzmann's constant and g_m is the device transconductance. The input common-gate input difference pair primarily contributes to the noise. The input stages are optimized for noise, while maintaining a high gain and low power, and a compact layout area. The outermost differential stages (M8, M13-M16) were optimized for power, layout area, and output swing.

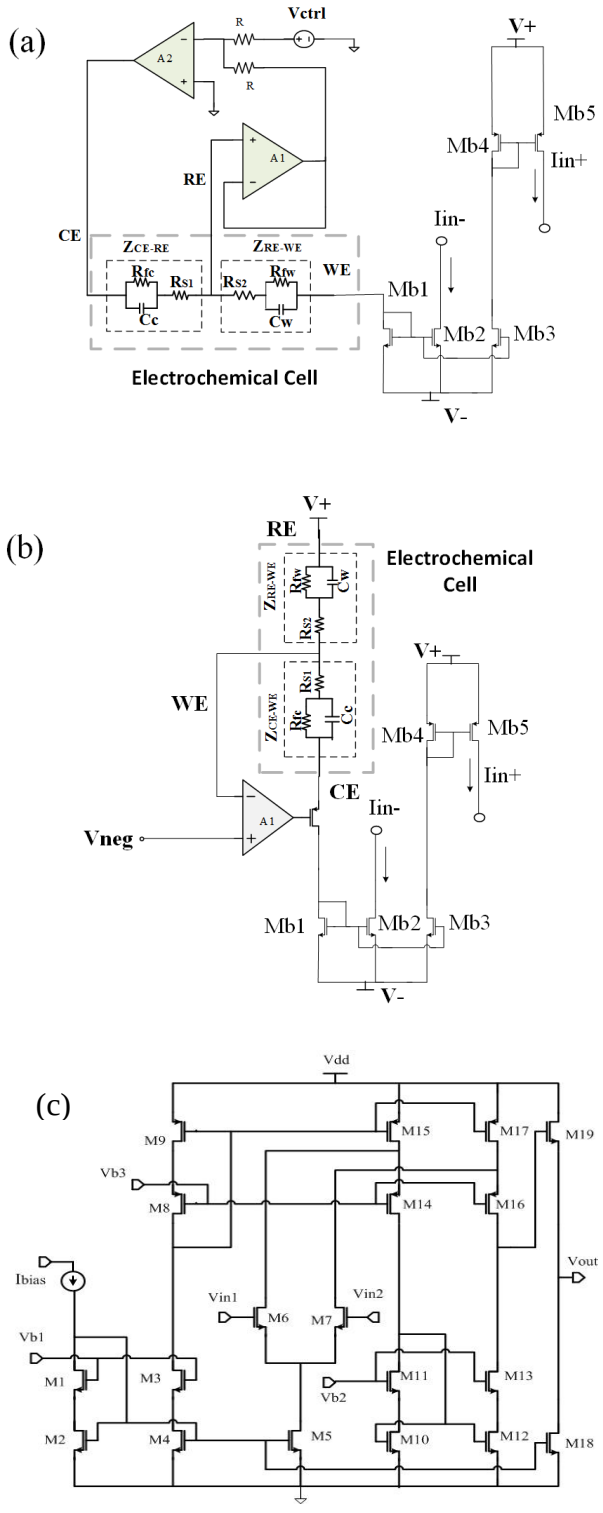

Fig. 4.3. Potentiostat control unit, (a) Amplifier based control unit, (b) Current regulator based control unit, (c) Folded Cascode amplifier A1and A2 [97].

4.2.2.2 Electrochemical Cell Voltage Swing

A potentiostat topology applicability for a particular application is strongly dependent on the allowable voltage swing. Wide voltage swing is necessary to detect electrochemical species that requires varying activation potentials. Glucose detection based on H_2O_2 reduction with VACNF microelectrodes needs approximately -0.6 to -0.78V across the reference and working electrode. The voltage swing that the potential control unit offer for the proposed potantiostat can be expressed as,

$$S_{differential} = |V_{DD}|.\frac{R_w}{R_w+R_A+r_o} \quad (17)$$

where R_w denotes the faradaic resisrance of the VACNF microelectrodes, R_A is the faradaic resistance of counter electrode, r_o denotes the drain source resitance of the diode connected MOSFET. For $R_W >> R_A, r_o$, the voltage dynamic range converges to rail voltage and since the potentiostat uses a 1.8V rail, and the voltage swing can theoretically be as high as 1.8V according to equation (7). However, the voltage swing will be limited to a transistor threshold below and above the the highest (~1.4V) / lowest rail (~450mV), respectively.

4.3 Current Starved VCO

The TIA output is fed into a VCO for frequency translation. A standard 5 stage VCO topology followed by a buffer was designed which gives approximately 500 kHz of change in frequency per 0.1V change in TIA output. The 0.1V TIA output change correspond to a 1µA change in sensor current (Fig. 4.4). The current starved VCO gives wider dynamic range and linearity at significant low power. The transistor sizes are as follow, MP1, MP3=6µm/2µm; MP2=60µm/2µm; MN1, M16=3µm/2µm; MN2 =40µm/5µm; MN3= 3µm/1µm; MN4=30µm/1µm. The digital buffer utilized 2 inverters where the first inverter has PMOS, NMOS aspect ratio of 6µm/2µm and 4µm/5µm respectively and the second inverter has PMOS and NMOS aspect ratio of 24µm/2µm and 16µm /5µm respectively.

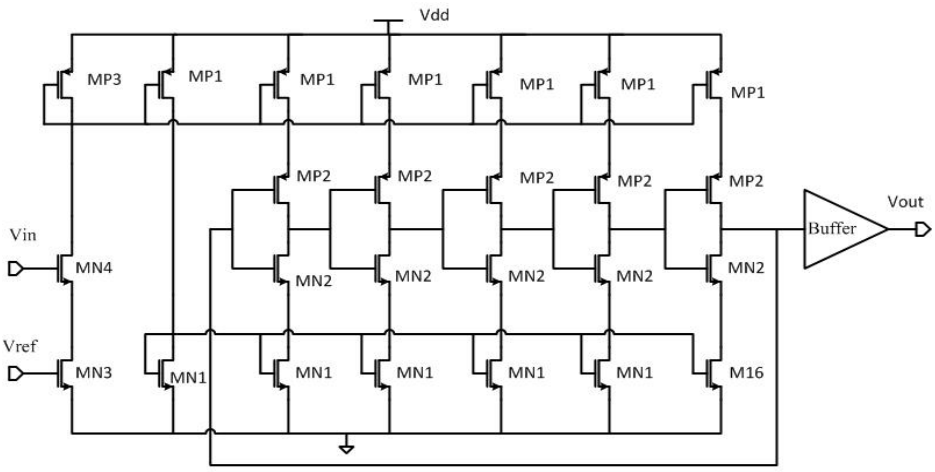

Fig. 4.4. Current starved VCO [58].

4.4 MonteCarlo Analysis and Test Results

MonteCarlo plots for the folded cascode OTA stages (A,A1,A2) are shown in Fig. 4.5 and Fig. 4.6. The designed folded cascode OTA demonstrates mean gain of 60.7039 dB with a standard deviation of 1.749 dB and mean bandwidth of 8.47 kHz with a standard deviation of 2 kHz due to process variations (variations in mobility, velocity saturation, temperature dependences, early voltages). Mismatch (body effect, threshold and other layout related variations) demonstrates mean gain of -5.764 dB with a standard deviation of 33.174 dB and mean bandwidth of 923.97 kHz with a standard deviation of 1.094 MHz. The large deviations due to mismatch largely originated from using weak and moderate inversion devices in the amplifier to minimize power. The designed amplifier performance is thus heavily dependent on the matching accuracy and requires adoption of precise layout techniques. The integrated system response is shown in Fig. 4.7. It is evident that the integrated system has a linear range of operation from 200nA to 5µA. To perform the amperometric test with glucose the potential control unit is used to maintain a 0.781V potential difference between the reference and the working electrode. Glucose concentrations ranging from 1mM to 20mM was added to 150mM phosphate buffer saline (PBS) and poured into a well built around the VACNF microelectrodes. The amperometric test results are shown in Fig. 4.8. The amperometric test suggests that the VACNF

microelectrodes with 900 VACNF microelectrodes show linear responses upto 5mM of glucose. Above 5mM nonlinearity introduced. With 400 VACNF forests the amperometric response of glucose concentration extends to up to 20mM without significant non linearity. Each concentration is prepared through weighing glucose and mixing with a measured volume of Milli-Q water. The mixing method adopted can lead to greater sample preparation error when compared with the serial dilution method. Serial dilution tends to give a more linear response. The test setup is shown in Fig. 4.9. The current two-chip integrated solution uses an off-chip biasing network. The power consumption of the integrated system components are as follows, the transimpedance amplifier consumes 44.5µW, the current regulator based potential control unit consume 27.2µW while the amplifiers A1 and A2 in the potentiostat consume 5.39µW and 6.06µW of power, respectively. The total power consumption of the potentiostat is 71.7µW. Fig. 4.10 shows the chip microphotograph of the potentiostat. Fig. 4.11 and Fig. 4.12 shows the layout of the amplifier based and current regulator based potentiostat potential control unit respectively. Fig. 4.13 shows the layout of the VCO unit.

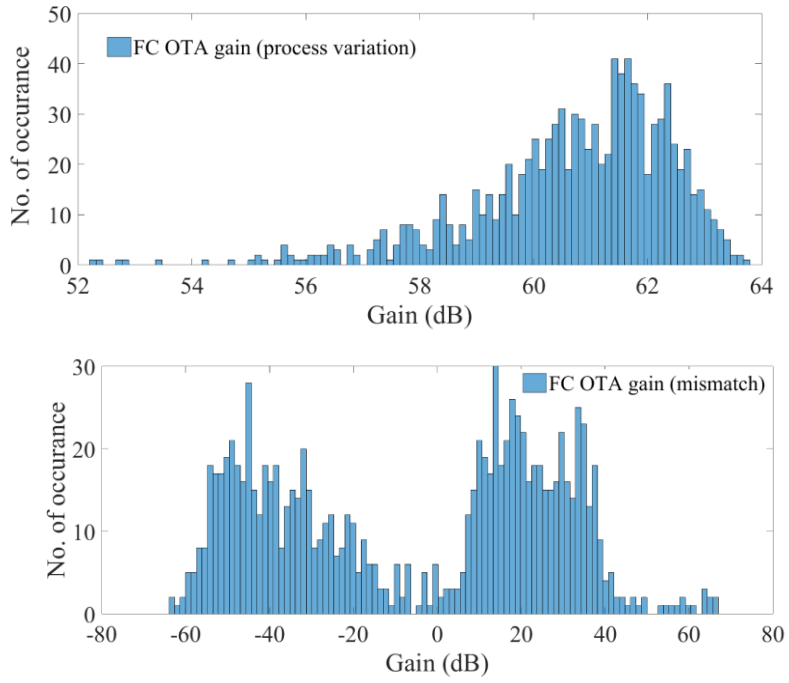

Fig. 4.5. MonteCarlo plots of folded cascade OTA. Gain variations due to process and mismatch.

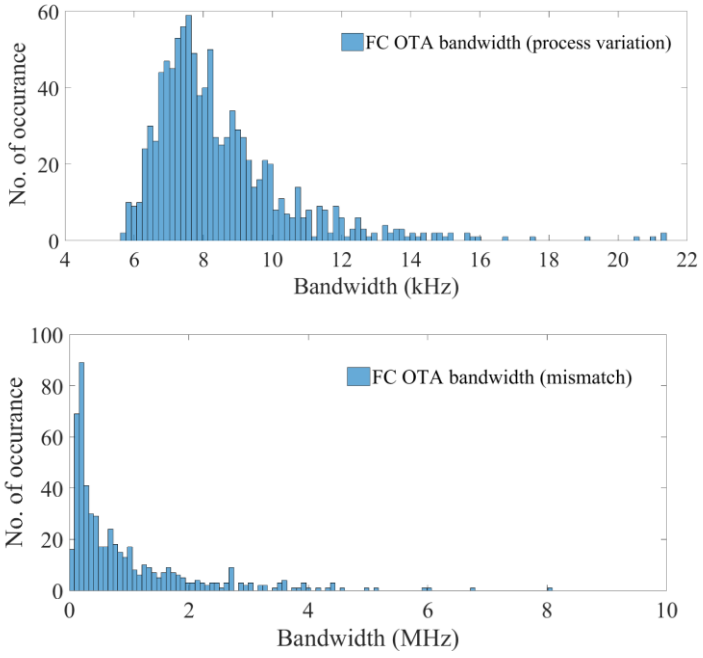

Fig. 4.6. MonteCarlo plots of folded cascade OTA. Bandwidth variations due to process and mismatch.

(a)

(b)

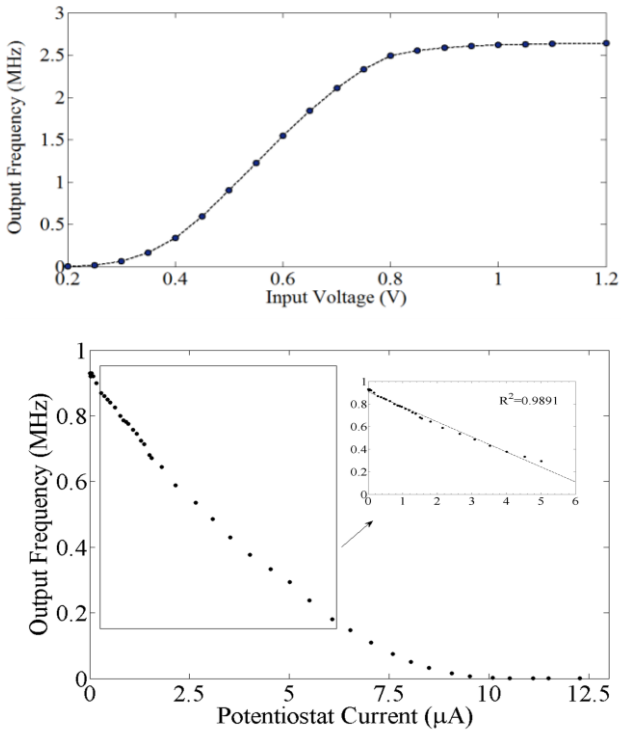

Fig. 4.7. (a) VCO transfer plot, (b) Transfer characteristics of the integrated potentiostat [97].

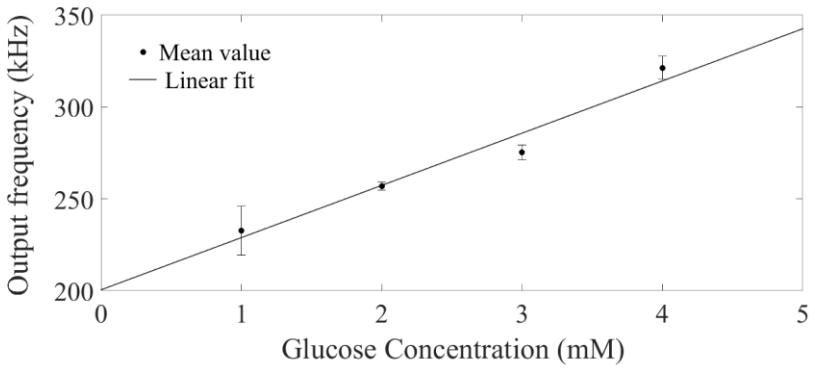

Fig. 4.8. Amperometric response of glucose solution in 0.1M PBS with a 15×15 VACNF forest array (pitch 20µm) on a 300µmx300µm Ti at the VCO output (modulating signal) [97].

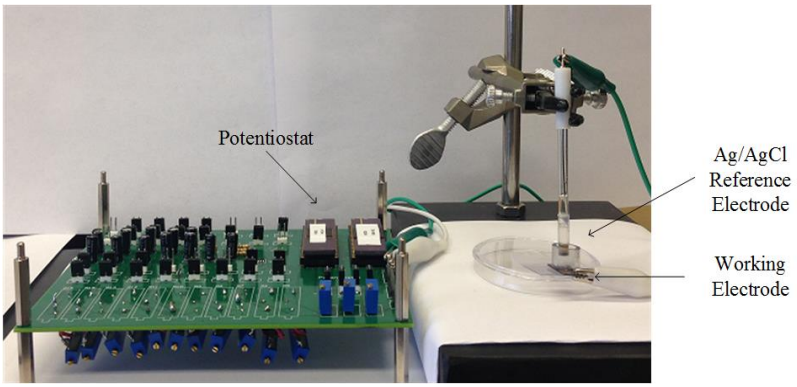

Fig. 4.9. Experimental test setup [97].

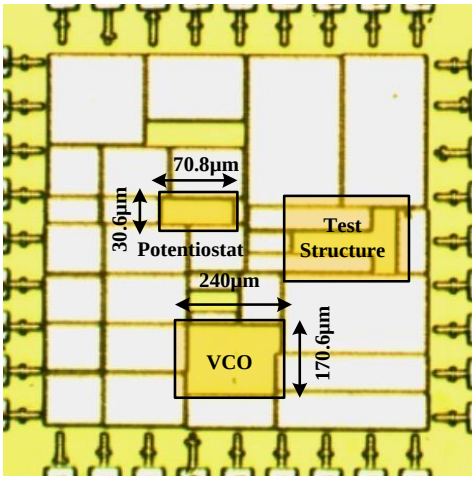

Fig. 4.10. Chip photomicrograph of the potentiostat.

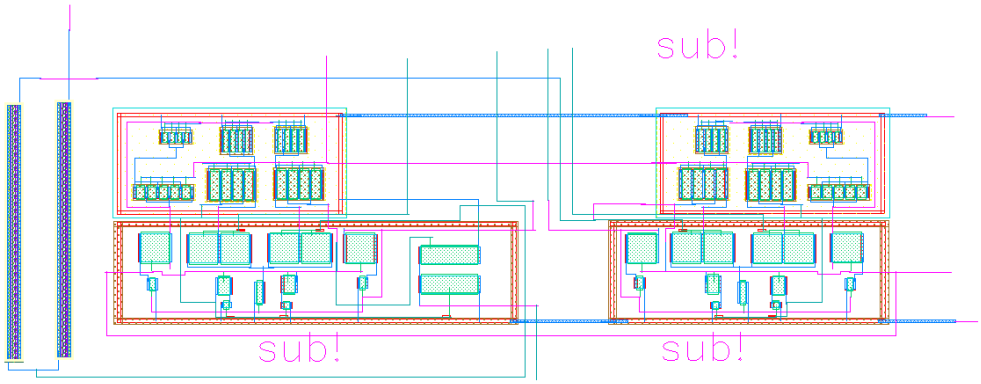

Fig. 4.11. Layout of the amplifier based potentiostat potential control unit.

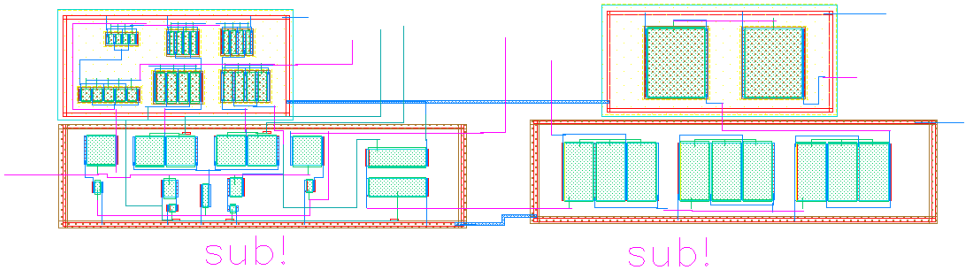

Fig. 4.12. Layout of the a current regulator based potentiostat potential control unit.

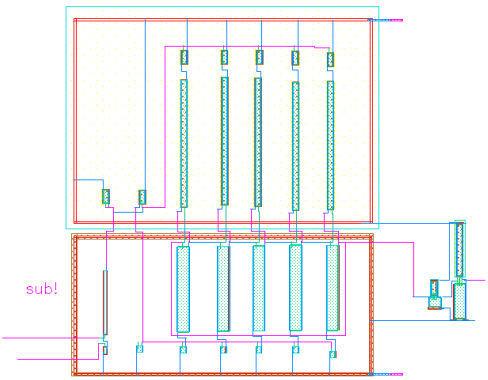

Fig. 4.13. Layout of current starved VCO.

4.5 Performance Comparison

Table 4.1 shows the comparative performance of the VACNF microelectrodes in amperometric sensing [24-26]. VACNF-SU8/GOx/HRP sensor platform demonstrates sensitivities which allow use of the platform for highly sensitive detection (200nA/mM). Table 4.2 shows a comparative performance of potentiostat topologies [63, 67, 69, 75, 79] . When compared with the state-of–the–art potentiostat in similar standard CMOS process, the proposed potentiostat topology demonstrates power and area efficiency (demands 39.83µA from a 1.8V supply and takes 0.0179 mm^2 chip space). A cyclic voltammogram (CV) plot was performed to verify the onset of reduction reaction using CH instruments CHI660D potentiostat and our implemented on-chip potentiostat are in good agreement except that the on-chip TIA produces errors when current falls below 0.1µA. A figure of merit similar to power-aware metric used in low power processor comparison has been proposed to compare the performances of the potentiostat. The FOM can be defined as below:

$$FOM=(Imin/Irange)*P*A \quad (18)$$

where Imin (nA) = lowest detectable current, Irange (A) = input dynamic range, P (W)= power dissipation, A(mm^2)= area required for system implementation.

Table 4.1. Comparison of amperometric glucose sensor performance

Ref.	**Sensor Type**	**Reaction Potential**	**Sensitivity**	**Linear Glucose Concentration Range**
Periasamy *et al.* [24]	GCNT/GOx/GAD	-0.44V	507nA/mM	6.3-20.09mM
Yao *et al.* [25]	GCE/CNT/Au/PDDA-GOx	-0.3	2.5µA/mM	0.5-5mM
Tsai *et al.* [26]	PPy-cMWCNT-GOx	+0.9	95nA/mM	0.28 to 4mM
Proposed system	VACNF-SU8/GOx/HRP	-0.78	50-200nA/mM^{-1} 89.035µA/mM^{-1}	1 - 11mM 0.4-40µM

Table 4.2. Comparison of potentiostat topology performance

Work	**Yang *et al.* [75]**	**Roham *et al.* [67]**	**Martin *et al.* [63]**	**Nazari *et al.* [69]**	**Sohn *et al*. [79]**	**Proposed System**
Process	0.5 µm	0.5 µm	0.18µm	0.35 µm	0.13 µm	0.18µm
CE	Ti/Au	Not Reported	Pt wire	Not Reported	Not Reported	Ag/AgCl
RE	Ag/AgCl	Ag/AgCl	Calomel	Not Reported	Ag/AgCl	Ag/AgCl
WE	Ti/Au	Carbon fiber microelectrode	Pt	Not Reported	Pt	Vertically aligned Carbon nanofiber microelectrode
WE Electrode Size	$100\mu m^2$ (4x4 array)	3.5µm radius (100µm length)	10^{-6}-10^{-4} cm^2 (7 x 2 array)	200µmx200µm	Commercial Pt electrode	300µmx300µm (30x30 array)
Chip Placement	Off-chip	Off chip	On chip	On chip	Off chip	Off chip
Current Readout	Switched Capacitor	Sigma-delta modulator	Fully differential	Fully differential	Single ended	Difference-differential
Power Supply	5V	2.6V	1.8V	3.3V	3.3V	1.8V
Isupply	600µA	22µA	8.8mA	16µA (per OTA)	148µA	39.83µA
Sensor current detection range	6pA-10µA	10pA-400nA	Not Reported	100p-60nA	1µA-20µA	500nA-7µA
Potentiostat Core Area (mm^2)	1.68 (approx.)	0.06	0.45	0.04	0.036	0.0179
FOM	3.02	0.0858	Not Available	10.6	925	37.7

4.6 Discussion

In this chapter, we have demonstrated our novel proposed solutions to achieve low power area efficient potentiostat system for integration with a VACNF based sensor system. The integrated system consumes 71.7μW of power from a 1.8V source and can be implemented in 0.0179 mm^2 chip space. The VACNF-SU8/GOx/HRP based sensor facilitates electrochemical charge transfer and demonstrates tunable detection sensitivities from 50 to 200nA/mM in physiological range glucose solution.

Note: Portions of this chapter has been published in the following articles:

[43] K. A. Al Mamun, and N. McFarlane, "A CMOS potentiostatic glucose monitoring system for VACNF amperometric biosensors," *IEEE International Symposium on Circuits and Systems*, pp. 477-480, 2015.

[97] K. A. Al Mamun, S.K. Islam, Dale K. Hensley, N. McFarlane , "A Glucose Biosensor Using CMOS Potentiostat and Vertically Aligned Carbon Nanofibers," *IEEE Transactions on Biomedical Circuits and Systems*, 2016 (Accepted).

CHAPTER 5
LOW-POWER BOWEL SOUND MONITORING SYSTEM

5.1 Bowel Sound Monitoring System

Continuous glucose monitoring systems have been a widely researched topic and implemented in a number of commercial artificial pancreases. An artificial pancreas takes glucose sensor data, predicts glucose variations using control algorithms and administers insulin dosage as required. Several clinical research studies demonstrated the usefulness of a continuous glucose monitor (CGM), as the CGM can well regulate blood glucose level to euglycemic level [4, 5]. An artificial pancreas consists of continuous glucose monitoring system, control algorithms, and a continuous subcutaneous insulin infusion (CSII) system. The artificial pancreas system measures glucose in blood plasma, monitors variations and applies insulin timing and dosage regulation by comparing the glucose level with standardized values. Dynamic physiological conditions such as meal events, food habits, stress levels, exercise, sleep patterns can greatly alter glucose levels [6-8]. Thus, the AP systems needs to consider the effect of these physiological variables when predicting glucose fluctuations using algorithm. Current APs do not offer any feature to measure the dynamic event and is susceptible to potential negative events due to over/under dose of insulin. Overdose of insulin, or delayed insulin infusion after a meal event can result in a hypoglycemic state and could lead to coma in extreme cases. On the other hand underdose of insulin can cause hyperglycemia leading to complex health complications. Complex algorithms and multiple sensor platforms show much promise to implement a true AP system for real life scenarios, however challenges lie in the implementation of such algorithms which mostly requires nonlinear feedback [8, 80]. To implement the glucose level dependence with the physiological variables, current CGMs require manual administration by a patient or health caregiver. These CGMs can detect adverse events, trigger emergency alarm or stop insulin infusion. To fully automate the physiological feedback activity, the monitor can provide locomotion data while bowel sounds could be traced to meal events, glucose fluctuation or gastrointestinal motility. It has been

demonstrated in numerous research studies that bowel occurrence rates and features are correlated with motility, food type, and blood glucose levels [9].

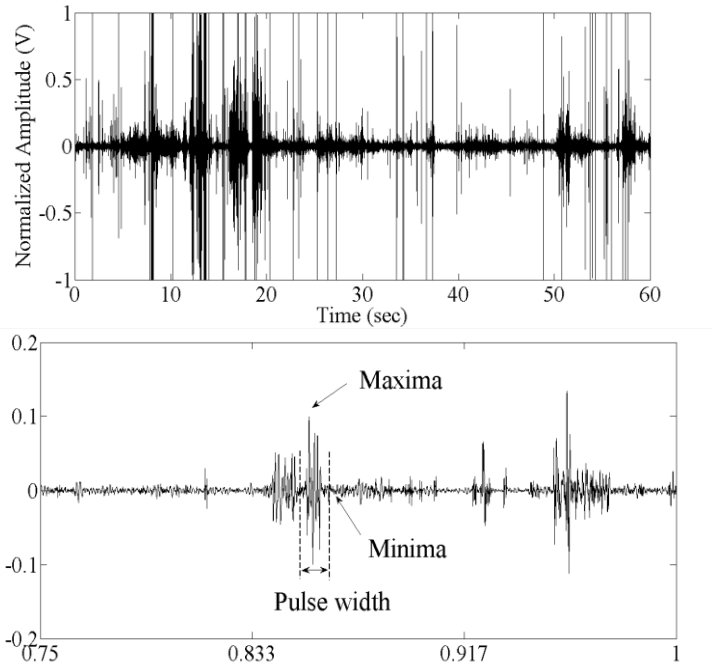

Fig. 5.1. Abdominal bowel sounds (Inset: filtered bowel sounds and features utilized for the detection) [95].

Bowel sound measurements is a clinically accepted method to the detection of sepsis, small volume ascites, intestinal transit time and assessment of abdominal surface [81, 82]. A number of methods for bowel enhancement, detection and segmentation exist with the help of wavelet analysis, neural network and estimation algorithm [81, 83-86]. The relationship of bowel rate with food consumption and the onset of meal instances have been demonstrated [87-91]. The current state of art systems require bulky and power intensive structures to implement feature signal analysis. As such the current instrumentation forbids inclusion of such system in a portable Lab-on-a-chip device.

Bowel sounds show certain notable features. The signal spectrum lies below 500Hz, the peaks and troughs can be identified in the bowel while the sounds are of short duration (Fig. 5.1). A research study has been performed to identify bowels from interfering sources by extracting bowels using these features [91]. Implementations of an algorithm which can

correlate and identify the pattern in real time can successfully isolate the bowel sounds. For the study stethoscopes were placed on the abdomen to detect the bowel sounds, however in a portable device this will cost much space, and at the same time is not very convenient to use [90]. An alternative flexible piezoelectric film sensor can be utilized for the portable application. The charges in the sensor can be amplified with a charge amplifier. The power intensive blocks in a bowel monitor are the digital signal processors (DSP), which can be replaced by implementing an analog feature extractor and mixed signal processing block. This can facilitate reducing computational load by working in conjunction with a DSP. Analog feature extraction has been a widely researched in neural amplifiers [92, 93]. Thus, combination of a flexible piezoelectric film, charge sensor, feature extractor, and control algorithms can offer implementation of a portable bowel detection system.

5.2 Proposed Bowel Sound Monitoring System

A bowel detection algorithm can be implemented which compares features and records only extracted bowel sounds which meet predetermined criteria. A bowel bit can be generated corresponding to successful bowel detection. A counter following the bowel bit can count the bowel occurrence rate per minute or any specified time. An overview of the sensor integration and proposed monitoring system is shown in Fig. 5.2.

The proposed bowel sound detection system consists of several blocks. First, to sense the abdominal vibration in the presence of interfering signals microphones and stethoscopes has been widely used [83,88,94]. Placing a stethoscope during measurement forbids implementation in a portable system. Piezoelectric film sensors can be a better alternative to these sensors. Second, to sense the charges in the piezoelectric sensor a charge amplifier can be employed. The sensitivity of a charge amplifier can be tuned with capacitor banks. Third, a low pass filter is required at the output of the amplifier to filter out interfering environmental noise sources including sliding, walking, talking, heartbeats [90]. Fourth, to sort the signals based on the peaks, troughs, pulse widths a feature extractor is needed which can extract signal features and perform a matching test. Fifth, to sort the bowels an

algorithm unit is required to locate bowels and count the occurrence rates. The proposed system consisting of a tunable charge amplifier, analog feature extractor and an algorithmic logic implementation unit [95, 96].

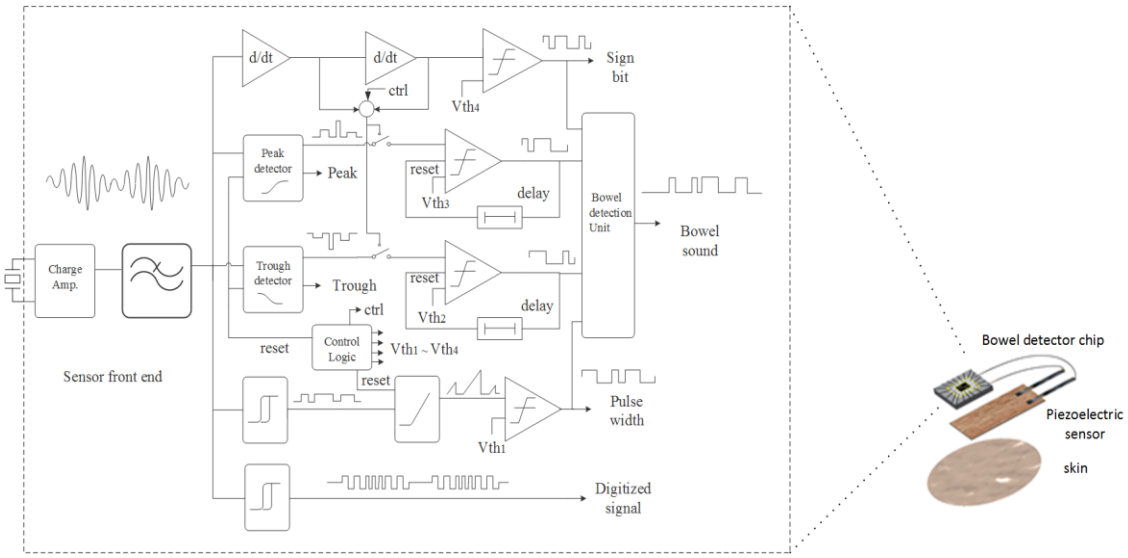

Fig. 5.2. Overview of bowel sound detection system [96]

5.2.1 Piezoelectric Sensor

A commercial flexible piezoelectric film sensor, model DT series/FDT series from the Measurement Specialties were proposed to use in the sensing front end (Fig. 5.3). Both the sensor has a laminating film covering the sensor which ensures affix the sensor directly on the patient's abdomen. A medical patch can be used to ensure a robust contact. The flexible piezoelectric sensor (FDT series) offers better integration compared to the DT series. The output of the piezoelectric sensor is fed into the input of a charge amplifier.

5.2.2 Charge Amplifier

For signal conditioning of the piezoelectric sensor, charge amplifiers are a popular choice. Charges generated in the piezoelectric material are integrated in the charge amplifier to produce a proportional voltage. An integrator circuit can act like a charge amplifier where

the charge gain is inversely proportional to the feedback capacitance when a high open loop amplifier is used. Tunable feedback capacitance can give variable gain in a charge amplifier. In this work a 52dB folded cascade amplifier is utilized as the core amplifier (Fig. 5.4). To achieve the gain specification at low power the current mirror MOSFETs were biased in strong inversion region while the cascaded stages were in moderate inversion. The inversion coefficient were used to optimize transistor sizes as follows: The transistor sizes to achieve this were: M6, M7=10µum/5µm; M1,M3=5µm/5µm; M2, M4=1.92µm/1µm; M5=3.84µm/1µm; M8=10µm/1.5µm; M4, M16= 20µm/1.5µm; M9=6.88µm/0.75µm; M15, M17=16µm/0.75µm; M11, M13=3µm/2µm; M10, M12= 1µm/1µm. To complete the feedback path a DC stabilizing resistor, realized by a MOS transistor working in triode region was designed in parallel with capacitor banks in series with switches. The feedback capacitors can generate charge gain from 0.003 to 100V/pC when integrated with Measurement Specialties piezoelectric film sensors which give approximately 10–15pC/microstrain. One microstrain represents the deformation of one part per million of an object under strain relative to its undeformed state. Strain is proportional to stress (units: N/m^2 or, Pa or psi) and can be represented as Strain(ε) / Young's modulus(E) (units: N/m^2, or Pa or psi). The charge amplifier was followed by a low pass filter to attenuate the interfering noise source. A third order low pass filter with a 1kHz cutoff is designed combining passive and active filter components. The charge amplifier gain can be represented as,

$$\frac{\mathrm{Vout}}{\mathrm{Q}} = \mathrm{e}^{-\mathrm{t}/\tau}.\ \frac{1}{\mathrm{Cf}} \tag{19}$$

Where, C_f is the feedback capacitance, τ is the time constant, Q is the integrated charge and Vout is the output voltage.

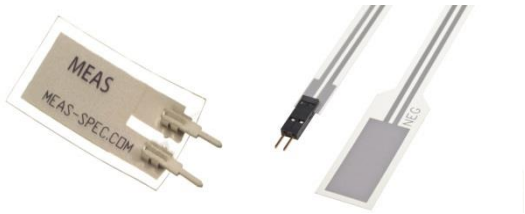

(a) (b)

Fig. 5.3. Piezoelectric sensors from measurement specialties (a) DT series, (b) FDT series [97]

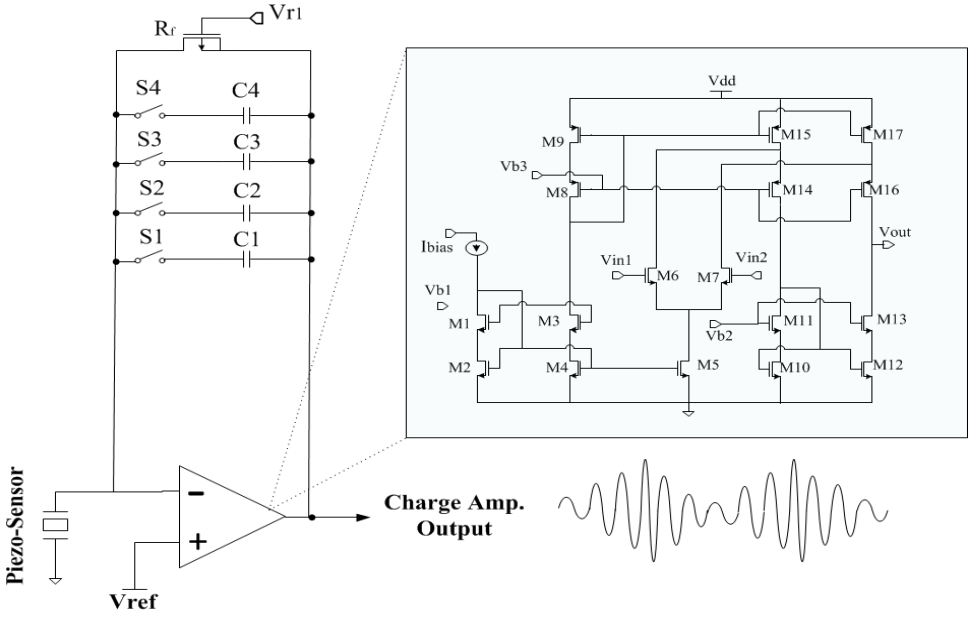

Fig. 5.4. Tunable charge amplifier [96]

5.2.3 Analog Feature Extractor

The feature extractor block consists of a signal peak and trough detector, differentiator, sign bit generator, pulse width detector block utilizing ramp generator, and digitizer blocks (Fig. 5.5, Fig. 5.6, Fig. 5.7, Fig. 5.8). 7 transistors 2 stages OTA topology and 5 transistors single stage OTA topology are used for the peak and trough detector respectively with the charging and discharging capacitors. After a peak and trough event the capacitor need to be reset using to enable recording the next events. The resetting event is synced with a synchronizer and control logic block. To detect signal slopes and sign bit, a second order differentiator is designed with a 9 transistor OTA, 1MΩ resistor and a 1pF capacitor in feedback path and 1MΩ resistor and a 50pF capacitor in series path. The transistors in the 9 transistor OTA were biased in weak inversion region to enable low power operation. The transistor sizes are M0, M1=2.82µm/30µm; M2, M3, M5, M6=2µm/50µm; M4= 1.28µm/50µm; M7, M8=30µm/1µm; M9=50µm/1µm; M10=4µm/1µm. The low power OTA topology gives 51dB gain with 55kHz bandwidth. A Schmitt trigger generates sign bit from the differentiator outputs. The transistor sizes are M1=10µm/5µm; M2=20µm/1µm; M3=10µm/1µm; M4=1.5µm/0.5µm; M5=0.22µm/5µm; M6= 0.4µm/0.5µm. High performance comparators were utilized to digitize the peak and trough value by comparing with experimentally extracted threshold levels. The comparator consists of a high performance 3 stage comparator topology which is comprised of a cross couple stage, a 5 transistor OTA and a digital buffer. The transistor sizes are M1, M2=10µm/30µm; M3, M9, M10, M11, M12, M13=30µm/10µm; M4 =6µm/30µm; M5, M6, M7, M8=15µm/20µm; M14=30µm/4µm; M15, M16=4.5µm/10µm; M17, M18=6µm/20µm; M19=1.5µm/0.75µm; M20=0.7µm/1µm; The raw input signal is digitized and fed into a ramp generator to create a ramp proportional to the pulse width. A current steering ramp topology is used to ensure fast charging and discharging rail-to-rail output at low voltage rail. The transistor sizes are M0, M1, M6, M7=10µm/30µm; M2=15µm/20µm; M3, M5=0.4µm/20µm; M4, M9= 15µm/20µm.

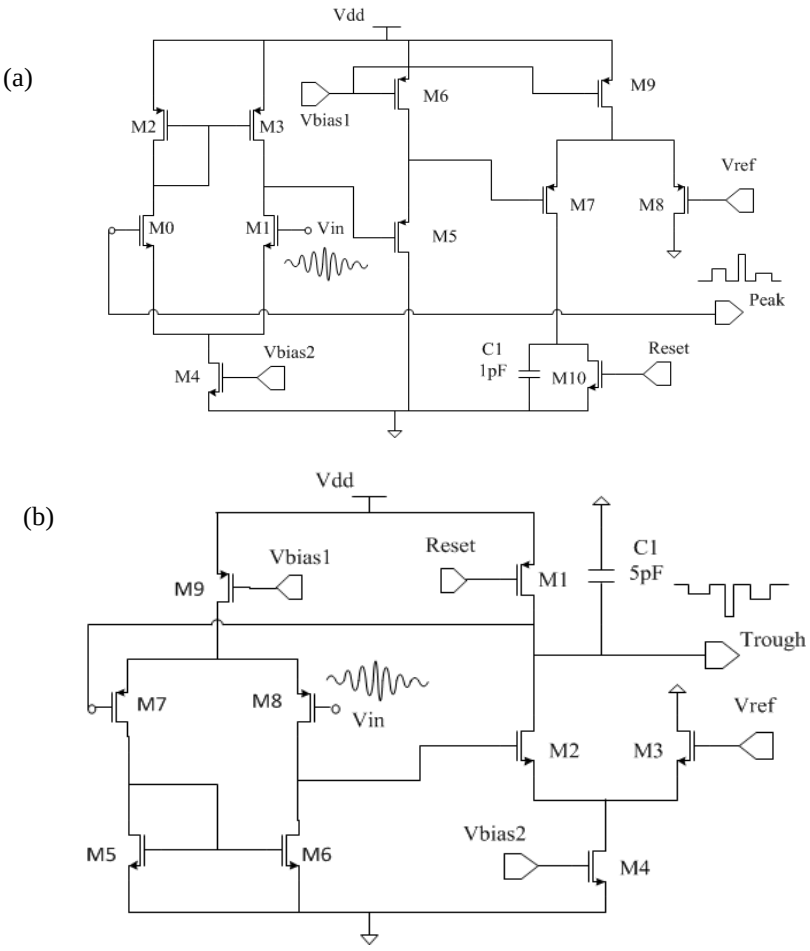

Fig. 5.5. (a) Peak detector, (b) Trough detector [96]

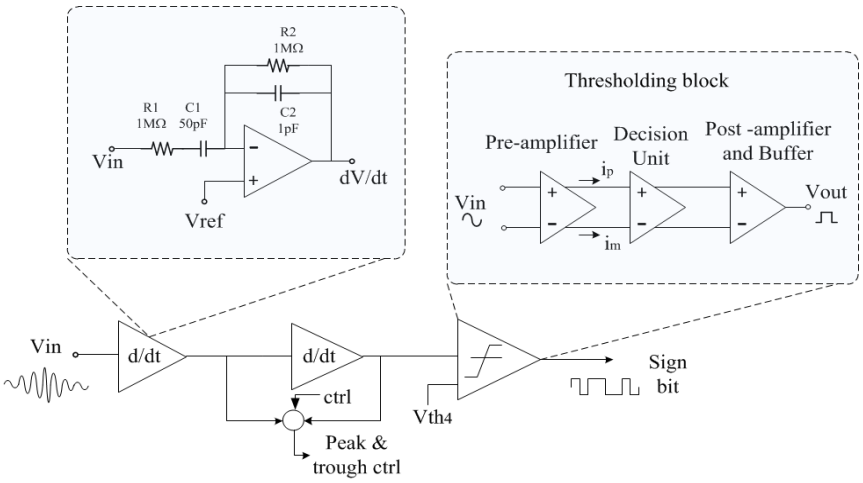

Fig. 5.6. Sign bit generator [96]

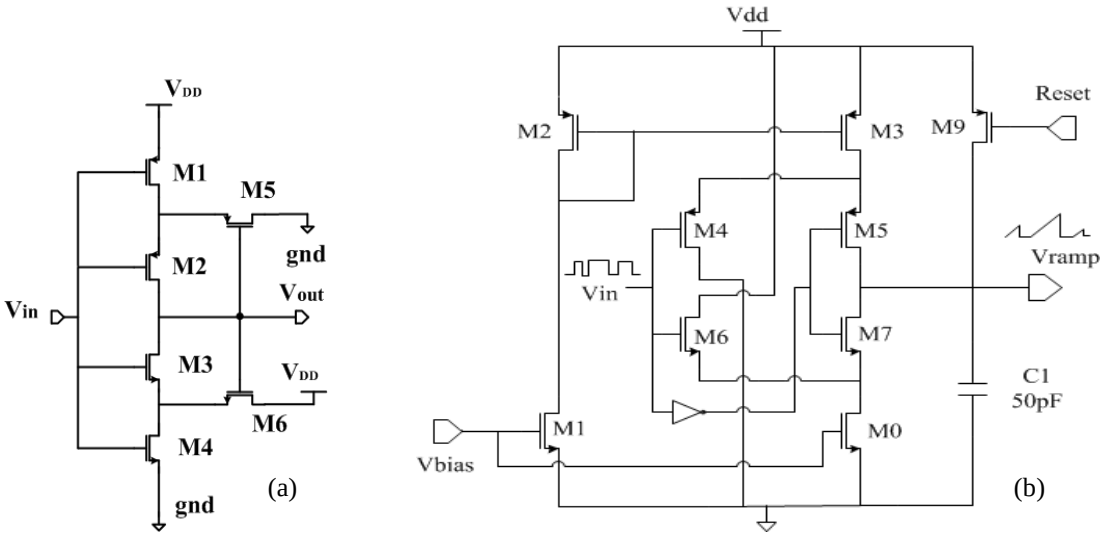

Fig. 5.7. (a) Schmitt trigger, (b) Ramp generator [96]

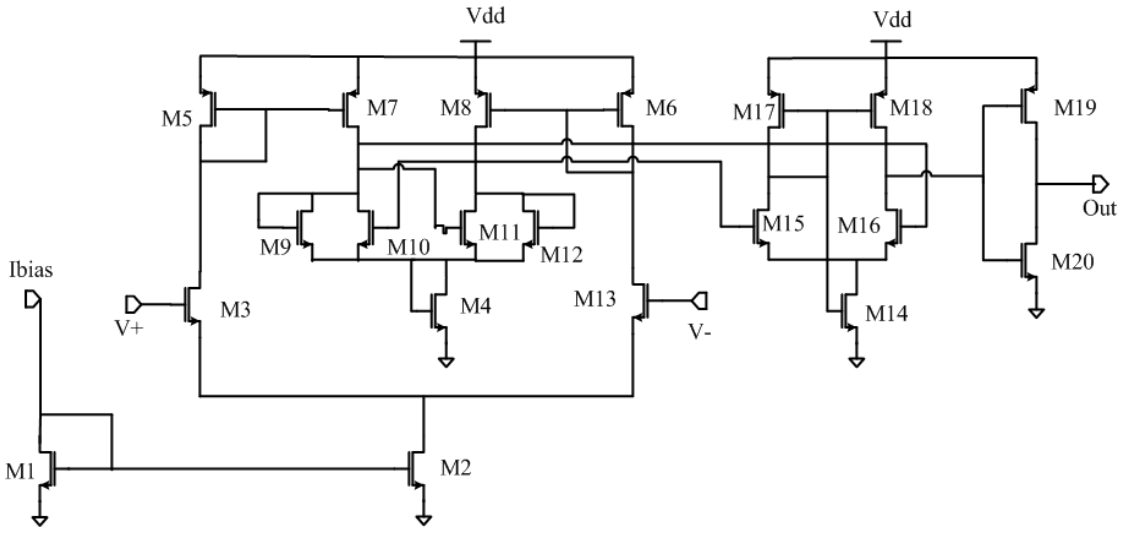

Fig. 5.8. High performance thresholding block [96]

The ramp generator and the schmitt trigger are optimized for low power operation using inversion coefficients (Fig. 5.7). The ramp value is compared with experimentally measured thresholds levels. From the raw bowel sounds the range of bowel pulse widths were identified and used as the controlling signals for the ramp. All the threshold levels were measured from recorded bowel sounds which were previously measured in a study with a digital stethoscope and a sound card. The feature extractor extracts peaks, troughs, pulse widths, slopes, sign bits from the measured signal and stores into an analog memory. All the control switches use transmission gates. The digitized data can be synced to a clock and fetched in parallel to an external flash memory using synchronizers.

5.2.4 Algorithm Unit

Digital logic gates were used to design the algorithm unit (Fig. 5.9). The control unit synchronized all the synchronizing event and control the data fetching operation. A successful measurement of peak bit forwards the algorithm to locate a trough. If a trough is located in the bowel the algorithm moves to measure pulse width. Peak bits, trough bits, sign bits, and bits corresponding to pulse widths are continuously fed into the algorithm to locate a possible bowel pulse. The algorithm performs following condition check,

$$(Max > Threshold1\ AND\ Sign\ bit < 0) AND\ (Min < Threshold2\ AND\ Sign\ bit > 0) AND\ (PW < Threshold3)$$

If the conditions are matched a bowel bit is generated. A successful bowel bit resets all the blocks to enable reading for the next bowel pulse. All the digital gates were designed using pseudo logic gates and transistors forced in subthreshold region of operation. This enables low power implementation but can adversely affect the delay performance. However, for the current application this is an acceptable tradeoff.

5.2.5 Bowel Count Unit

The bowel count unit counts a positive event when all the peaks, troughs, sign bits, and signal widths fall within the experimental threshold limit. A positive bowel event sends a

reset signal to all sub-blocks and acts as a clock to increment an 8 bit counter. The counter is implemented using pseudo-NMOS logic gates and transistors that operate in subthreshold region for low power operation. An off-chip delay unit generates a delay of approximately 1 minute and resets the counter to generate count rate per minute. An external port to sync and reset the counter is also added in the system to enable the communication with peripheral devices.

5.3 Simulation Results

For a regularly sustained (RS) bowel sound the bowel signal frequencies lie close to 500Hz. A simulation has been performed to verify the designed system performance for the RS bowel (Fig. 5.10). The test input signal is a sinusoidal signal with 500mV amplitude, the charge amplifier integrates the charges in the piezoelectric sensor and produces proportional voltage signal. The amplified signal was then filtered in the third order low pass filter which filters out any interfering noise above 1kHz (Fig. 5.10(b)). A digitized output of the RS sound is generated using finite hysteresis schmitt trigger (Fig. 5.10(c)). The peak or, maxima and trough or, minima tracks the signal peak and trough events (Fig. 5.10(d-e)). Once a peak and trough is detected a resetting pulse is generated in the control logic block to charge/discharge the capacitors in the peak and trough detector unit. Sign bit represents that a maxima or minima has been located in the pulse (Fig. 5.10(f)). A voltage corresponding to the bowel pulse width is generated by feeding the digitized signal to the ramp and comparing the ramp voltage with empirical threshold. A bowel bit is generated when the peak trough sign bit and the pulse width all falls within the experimentally determined threshold level (Fig. 5.10(h)). The bowel bits trigger the counter. The counter bits are shown in Fig. 5.10(i-j). The post layout simulation demonstrates that the charge amplifier consumes 3μW of power, the feature extractor, control logic block and algorithm unit consume around 10μW of power and the 8 bit counter consumes 40μW of power. A typical commercial neural network ASICs (such as CM1K, Pattern Recognition Chip with 1024 Neurons in Parallel by CogniMem^{TM} [99] requires upto 300mW power during

operation. Compared to the neural network based feature extractors the developed analog feature extractor consumes much less power (53μW).

5.4 Test Results

The charge amplifier was tested with an external stimulus of 50% duty cycle. The amplitude was 200mV. For the feedback capacitance of 10-360pF the tunable charge gain was 0.015-0.114V/pC (Fig. 5.11, Fig. 5.12). The bowel detector is fabricated in a 0.18μm standard CMOS process and tested with an external stimulus (Fig. 5.13(a)). Peak and trough detector units work as expected and tracks the bowel peak trough events (Fig. 5.13(b-c)). The signal slope dictates the sign bit (Fig. 5.13d). After the thresholding blocks the peak and trough bits were generated (Fig. 5.13(f-g)). The integrated system was then characterized with a previously recorded bowel sound. The bowel sound was measured using manual auscultation using a digital stethoscope, a LABVIEW program working in conjunction with a data acquisition card (Henry *et al.*). The bowel sounds were fed into the input of the feature extractor unit to measure functionality. A LABVIEW program has been designed which work with a NI DAQ card to generate the bowel sounds from the recorded wave file. The raw bowel sounds can be seen in Fig. 5.14(a), and the feature extractor responses to the signals are shown in Fig. 5.14(b-d). When all the conditions specified in the algorithm are matched, a bowel bit is generated, for the remainder of cases either one of the bits fail to comply and rejected in the logic unit giving negative bowel events. Measured positive bowel events were compared with the visually observed 8s of previously bowel recorded data and the accuracy of the detector is calculated as follows,

$$(\text{detected sound} - \text{actual sound})/\,(\text{actual sound}) \times 100\% \qquad (20)$$

The system response demonstrated 85% accuracy (Fig. 5.16(b)). The system is intended to be integrated with flexible piezoelectric sensor (Measurement Specialties LDT series). The

chip occupies 0.96 mm^2 of chip space (Fig. 5.16(a)). The chip components layouts are shown in the following figures, Fig. 5.15, Fig. 5.17, Fig. 5.18, Fig. 5.19, Fig. 5.20.

5.5 Discussion

In this chapter, we have proposed and demonstrated a low power solution to extract bowel features and detect bowel sounds in a silicon chip, and provide continuous physiological feedback of meal instances in an insulin pump. The system consists of a tunable frontend charge amplifier, an analog feature extractor, and a bowel detection and count unit. The implemented system consumes 53µW of power from a 1V power rail and can be realized in a 0.96mm^2 chip space.

Note: Portions of this chapter is published in the following articles:

[95] K. A. Al Mamun, M. H. U. Habib, N. McFarlane, and N. Paul, "A low power integrated bowel sound measurement system." *IEEE International Instrumentation and Measurement Technology Conference International*, pp. 779-783, 2015.

[96] K. A. Al Mamun, and N. McFarlane, "Integrated real time bowel sound detector for artificial pancreas systems," *Sensing and Bio-Sensing Research*, vol. 7, pp. 84-89, 2016.

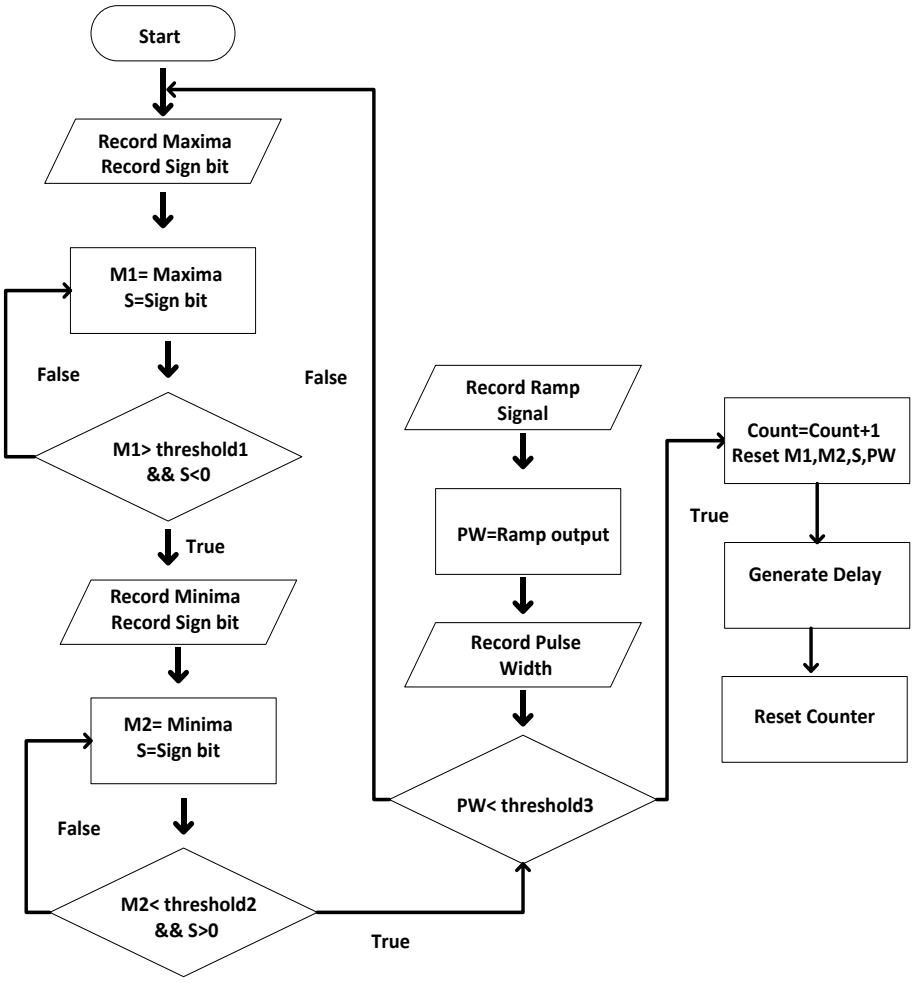

Fig. 5.9. Algorithm for detecting positive bowel events [95].

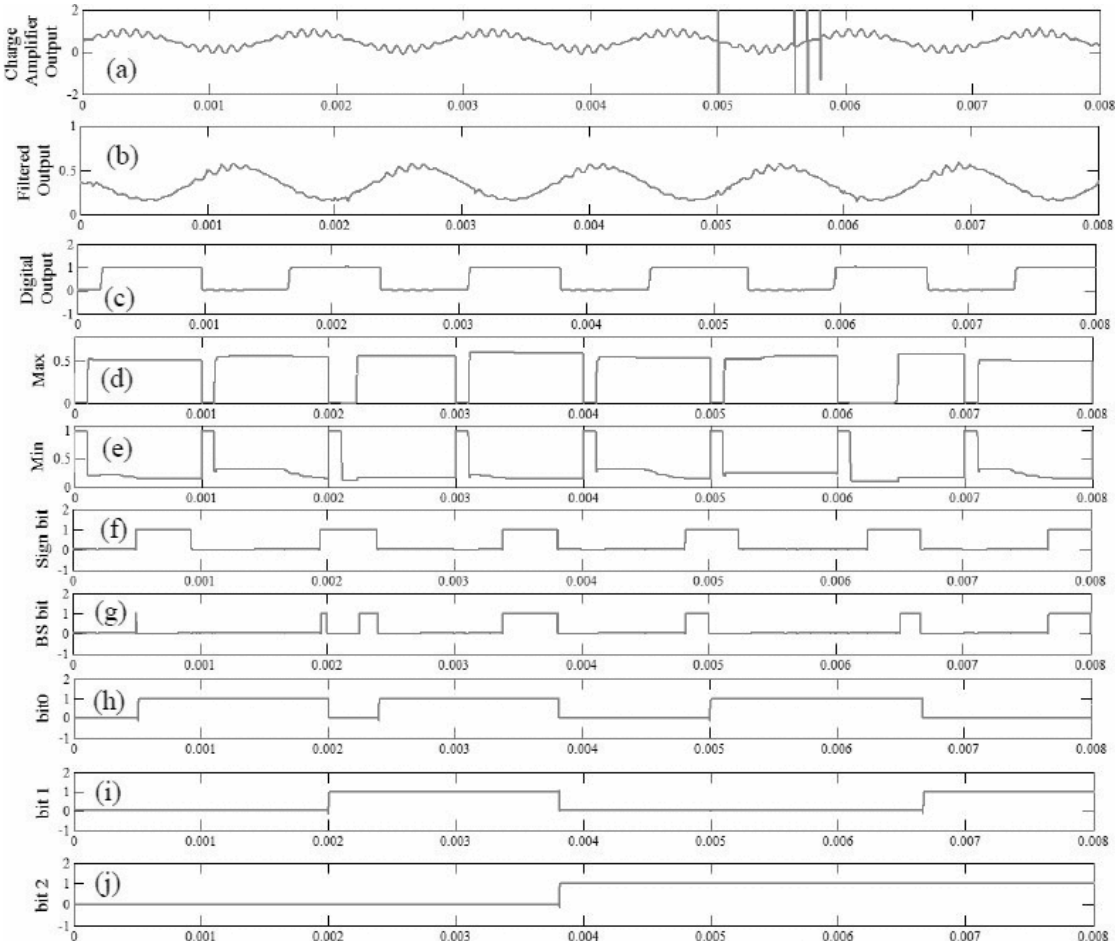

Fig. 5.10. Simulated system response [95].

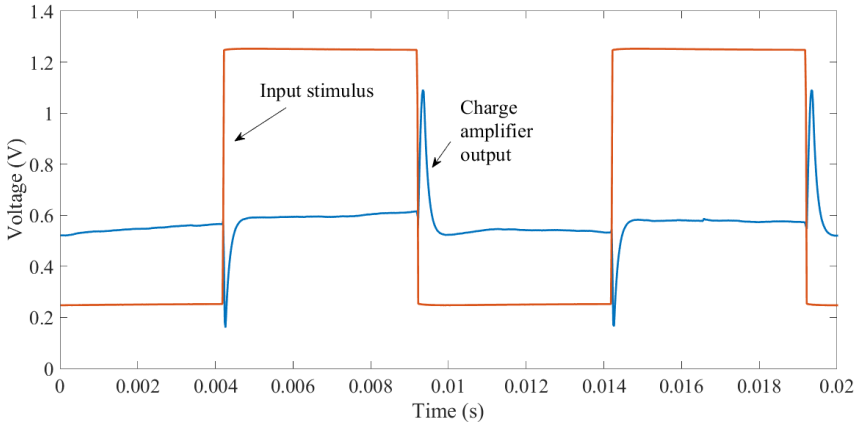

Fig. 5.11. Experimental charge amplifier response for Cf = 360pF.

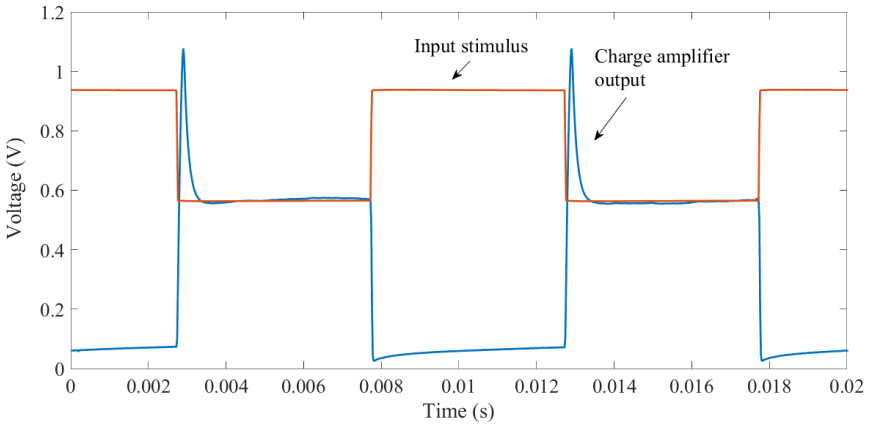

Fig. 5.12. Experimental charge amplifier response for Cf = 10pF.

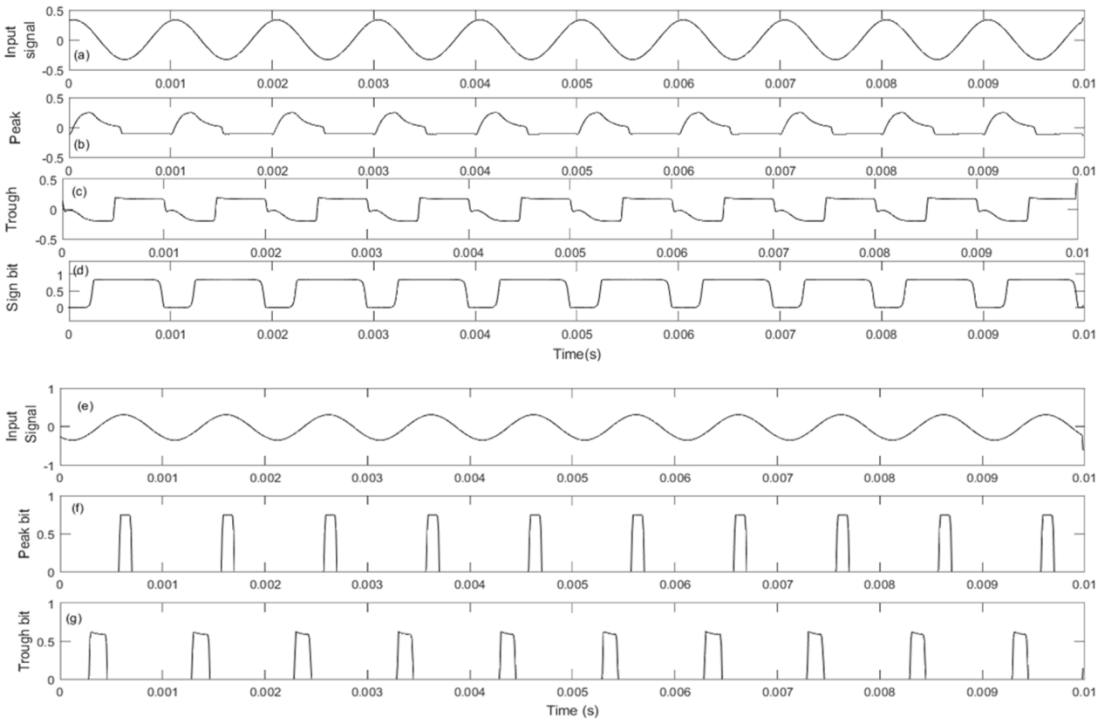

Fig. 5.13. Experimental bowel system characterization using sinusoidal excitation source, (a) Excitation signal, (b) peak, (c) trough, (d) sign bit, (e) excitation signal, (f) peak bit, and (g) trough bit [96].

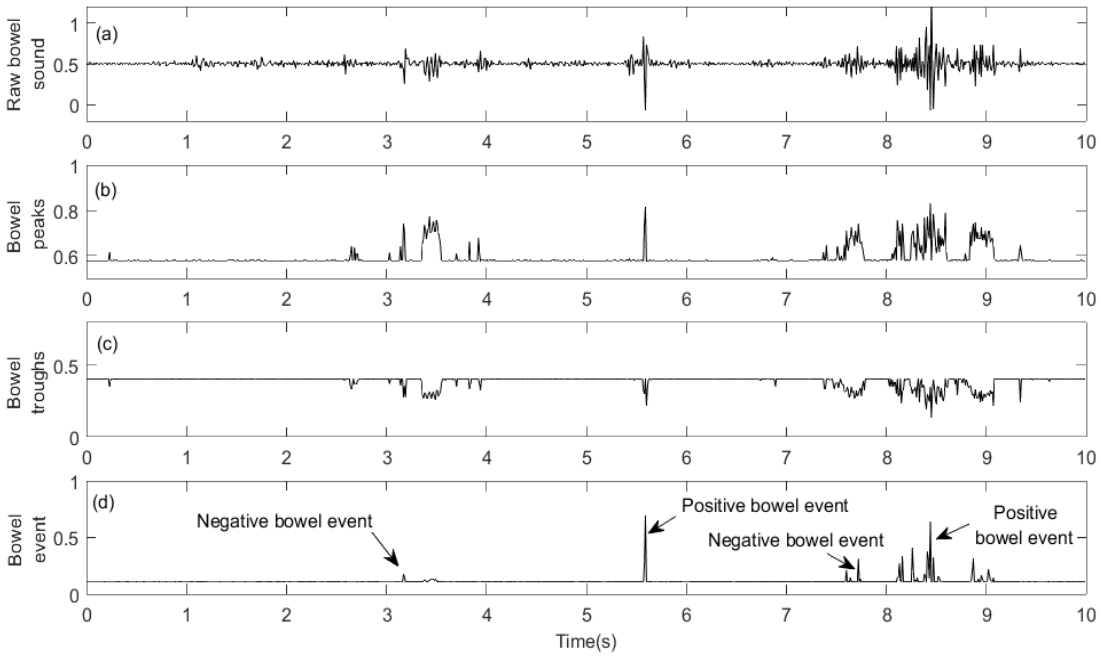

Fig. 5.14. Bowel sound detector system response to raw bowel sounds [96].

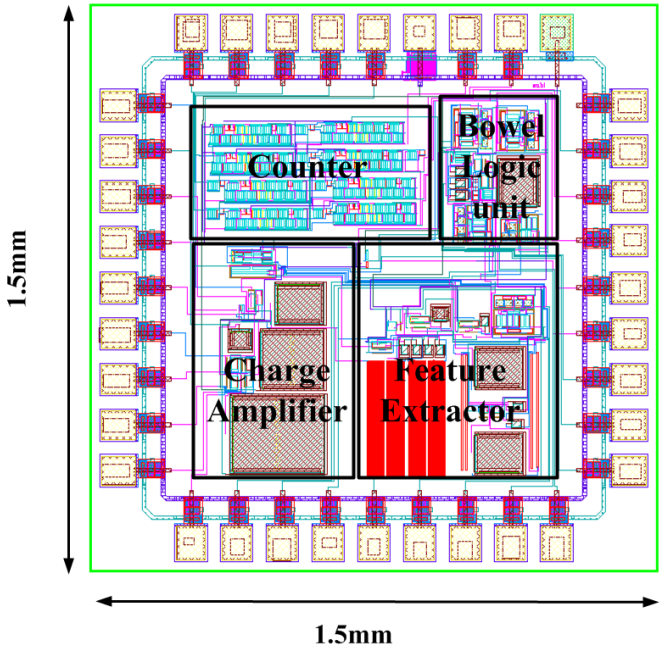

Fig. 5.15. Chip layout of the bowel monitoring system.

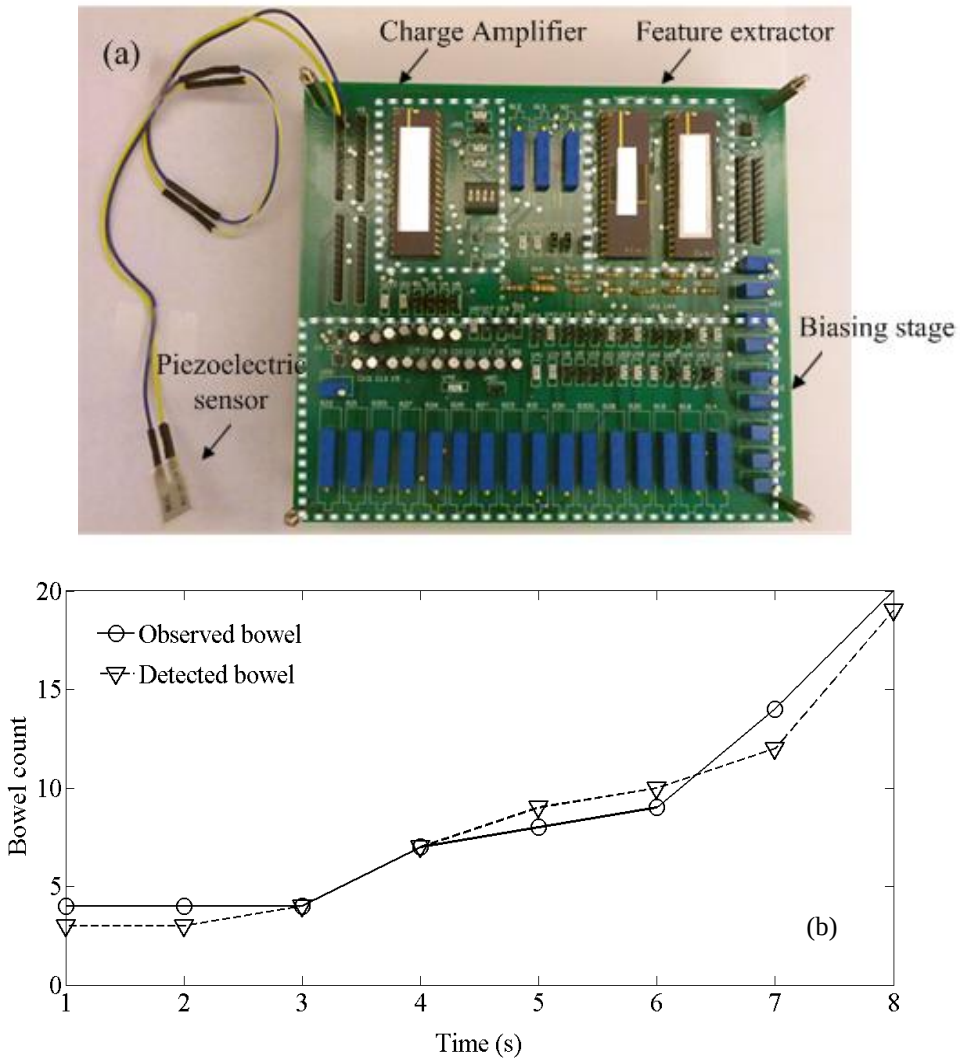

Fig. 5.16. (a) Bowel sound detector system, (b) system response to raw bowel sound showing detection of positive bowel events [96].

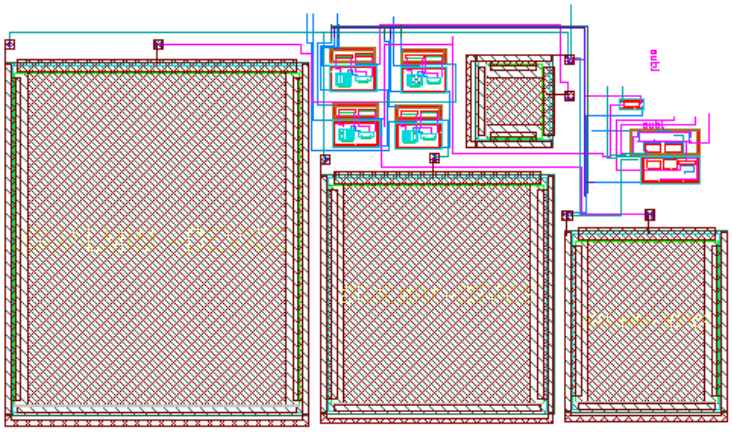

Fig. 5.17. Layout of the tunable charge amplifier

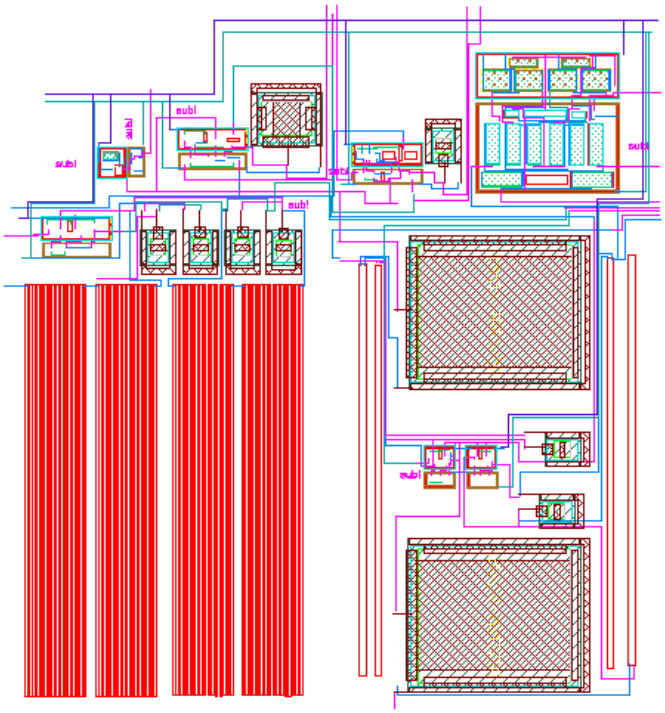

Fig. 5.18. Layout of the feature extractor unit.

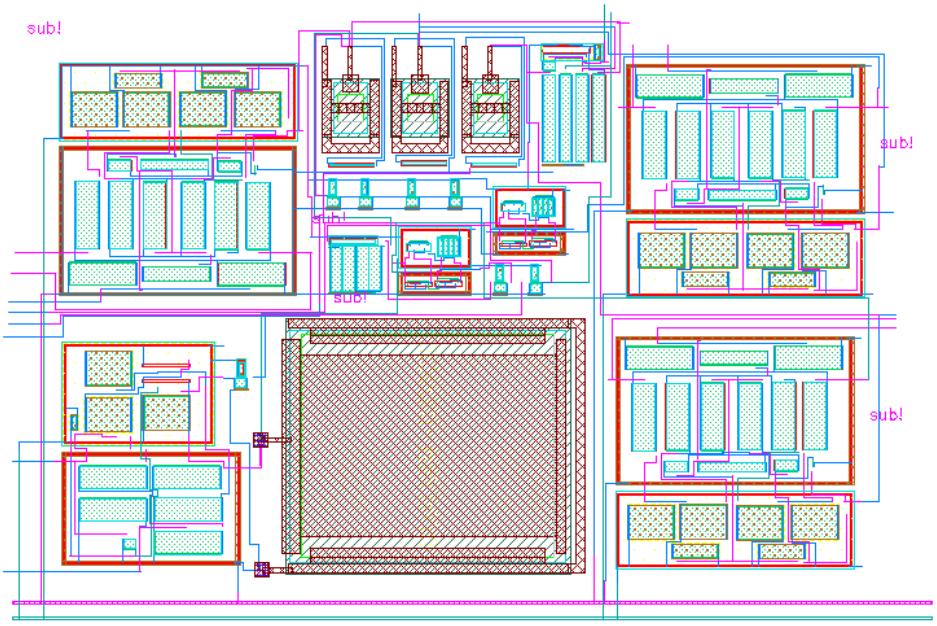

Fig. 5.19. Layout of the bowel logic unit.

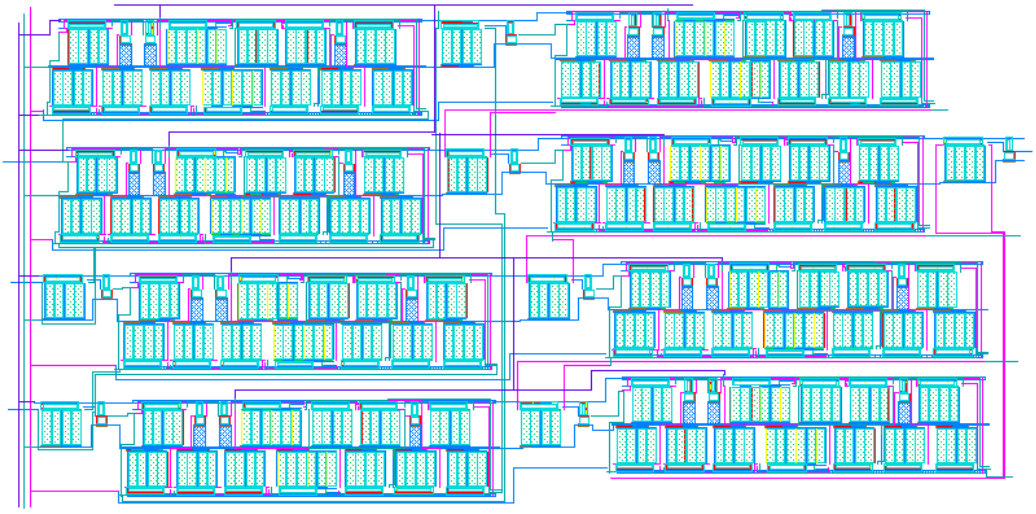

Fig. 5.20. Layout of the counter block.

CHAPTER 6
CONCLUSION

6.1 Original Contributions

Sensing systems suitable for improved diabetic health outcomes have been demonstrated. This dissertation identified key optimizing parameters of the sensors, readout and transmitter for a CMOS/VACNF glucose measurement system and demonstrated the first on-chip 52μW integrated bowel monitoring system. The original contributions of this work are as follows.

A microsensor front end for blood glucose measurement utilizing vertically aligned carbon nanofiber has been designed and implemented. The sensor platform was optimized and experimentally verified for glucose sensing with physiologically relevant levels. Optimization included circuit element models that are of significant value to further simulations and research on vertically aligned carbon nanofibers.

An empirical model of the VACNF sensor system has been presented, and a solution to achieve a robust and biocompatible VACNF microelectrode using SU8 coating has been demonstrated. Added robustness of the structure enables practical use of the vertically aligned carbon nanofibers in everyday use.

A novel solution to achieve low power area efficient potentiostat using a difference-differential transimpedance amplifier and current regulator based potentiostat control has been verified. These circuit topologies enhance the current state of the art in electrochemical sensing and are specifically well suited to VACNF sensors.

The first demonstrated response of a two-chip solution of a CMOS potentiostat with VACNF nanostrutures has been developed and verified with physiologically relevant glucose levels. The integrated two-chip solution significantly advances the state of the art with size, power requirements, sensitivity (200nA/mM) and limits of detection.

Ultra-low power on-chip instrumentation for continuous physiological data monitoring through abdominal bowel sounds has been demonstrated. This first, to the best of our knowledge, integrated sensing system for bowel sound measurements will greatly enhance patient feedback and improve overall diabetic outcomes.

The proposed microelectrode embedded potentiostat system proved the initial hypothesis that a low power portable glucose monitoring system requires nanotechnology approach to reduce the power budget and increase the sensitivity of the sensor that cannot be achieved using a macro sensor. New proposed topologies such as a current regulator based potentiostat potential control unit, and difference-differential transimpedance amplifier, and integration with current starved VCO demonstrates significant advantages in lowering the net power of a glucose monitoring system.

The proposed real time physiological feedback at low power proves that it is not always necessary to utilize computational intensive systems to realize a low power system. Rather an analog feature extractor can reduce the power cost and system complexity by many times. While this work focuses on the design area, the results significantly impacts patient treatment actions, such as the bowel sound detector can be utilized to automatically learn individuals eating instances eliminating the need for the patient to announce that a snack or meal event is about to happen.

6.2 Discussion

There are a number of future paths following the transformative results of this work.

VACNF transfer onto a CMOS chip will enable a complete single chip lab-on-a-CMOS chip solution for the system. The chip integration will allow small form factor implementation which is promising for implantable devices. This also reduces the parasitics increasing overall measurement speed. An alternative to VACNF, carbon nanospikes (CNS), which do not need any catalyst for growth, can be uniformly grown on

a high temperature resistant CMOS chip bonding pad to enable CMOS integration. Further uses of VACNF on CMOS requires tweaks in the fabrication process due to plasma arcing damage of the CMOS chip.

The proposed low power system can be tested in implantable applications. SU8 coating over the integrated system could act as the biocompatible layer necessary for CMOS chip implantation. For implantable applications the protocol for enzyme functionalization would have to be robust to ensure longevity of the adherence of the enzymes to the substrate.

A pseudo closed loop feedback can be added to the open loop difference-differential transimpedance amplifier which can extend the amplifier bandwidth and offer greater resistance to chip-to-chip variations due to PVT. The integrated system can be tested with glucose and other interfering fluids using a flow control system to mimic the blood glucose. The long term stability of the VACNF nanoelectrode in blood fluid needs to be verified.

The sources of low frequency noises place a detection limit of glucose. A major source of such noise is the flicker noise, hence the transimpedance amplifier can utilize a chopper stage to up modulate the flicker noise to a much high frequency and filter out in the subsequent stages. This will improve the limit of detection (LOD) by many times.

The bowel sound chip can be integrated with a flexible body worn piezosensor and used in ambulatory subjects to detect bowels and correlate the bowel count rate with meal, glucose level, and effect of physical stress. The analog feature extractor can be coupled with a neural network to find the types of bowel pattern and matched with intestinal motility.

The bowel detector can also be wirelessly integrated with a CGM system. The work [7] demonstrated that blood glucose control improves when the AP algorithm gets meal notifications. The bowel detector correlating food intake can provide automatic meal

notifications to a CGM and decrease patient interventions for the announcement. Finally the two separated systems can be integrated in a single platform.

REFERENCES

[1] "Standards of medical care in diabetes--2015: summary of revisions," *Diabetes Care,* vol. 38 Suppl, pp. S4, Jan, 2015.
[2] N. Tubiana-Rufi, J.-P. Riveline, and D. Dardari, "Real-time continuous glucose monitoring using Guardian® RT: from research to clinical practice," *Diabetes & Metabolism,* vol. 33, no. 6, pp. 415-420, 2007.
[3] S. K. Garg, H. K. Hoff, and H. P. Chase, "The role of continuous glucose sensors in diabetes care," *Endocrinology and Metabolism Clinics of North America,* vol. 33, no. 1, pp. 163-173, 2004.
[4] Y. C. Kudva, R. E. Carter, C. Cobelli, R. Basu, and A. Basu, "Closed-loop artificial pancreas systems: physiological input to enhance next-generation devices," *Diabetes Care,* vol. 37, no. 5, pp. 1184-1190, 2014.
[5] C. Cobelli, E. Renard, and B. Kovatchev, "Artificial pancreas: past, present, future," *Diabetes,* vol. 60, no. 11, pp. 2672-2682, 2011.
[6] M. Breton, A. Farret, D. Bruttomesso, S. Anderson, L. Magni, S. Patek, C. Dalla Man, J. Place, S. Demartini, and S. Del Favero, "Fully integrated artificial pancreas in type 1 diabetes modular closed-loop glucose control maintains near normoglycemia," *Diabetes,* vol. 61, no. 9, pp. 2230-2237, 2012.
[7] F. J. Doyle, L. M. Huyett, J. B. Lee, H. C. Zisser, and E. Dassau, "Closed-loop artificial pancreas systems: engineering the algorithms," *Diabetes Care,* vol. 37, no. 5, pp. 1191-1197, 2014.
[8] R. A. Harvey, Y. Wang, B. Grosman, M. W. Percival, W. Bevier, D. A. Finan, H. Zisser, D. E. Seborg, L. Jovanovic, and F. J. Doyle, "Quest for the artificial pancreas: combining technology with treatment," *Engineering in Medicine and Biology Magazine, IEEE,* vol. 29, no. 2, pp. 53-62, 2010.
[9] G. L. Coté, R. M. Lec, and M. V. Pishko, "Emerging biomedical sensing technologies and their applications," *IEEE Sensors Journal,* vol. 3, no. 3, pp. 251-266, 2003.
[10] P. He, and L. Dai, "Aligned carbon nanotube–DNA electrochemical sensors," *Chemical Communications,* no. 3, pp. 348-349, 2004.
[11] D. Lee, J. Lee, J. Kim, H. B. Na, B. Kim, C. H. Shin, J. Kwak, A. Dohnalkova, J. Grate, and T. Hyeon, "Simple fabrication of a highly sensitive and fast glucose biosensor using enzymes immobilized in mesocellular carbon foam," *Advanced Materials,* vol. 17, no. 23, pp. 2828-2833, 2005.
[12] O. Niwa, "Electroanalytical chemistry with carbon film electrodes and micro and nano-structured carbon film-based electrodes," *Bulletin of the Chemical Society of Japan,* vol. 78, no. 4, pp. 555-571, 2005.
[13] A. Hirsch, "The era of carbon allotropes," *Nature Materials,* vol. 9, no. 11, pp. 868-871, 2010.
[14] H. W. Kroto, J. R. Heath, S. C. O'Brien, R. F. Curl, and R. E. Smalley, "C 60: buckminsterfullerene," *Nature,* vol. 318, no. 6042, pp. 162-163, 1985.
[15] S. Iijima, "Helical microtubules of graphitic carbon," *Nature,* vol. 354, no. 6348, pp. 56-58, 1991.
[16] T. Hughes, and C. Chambers, *Manufacture of Carbon Filaments,* 1889.

[17] L. Radushkevich, and V. Lukyanovich, "About the structure of carbon formed by thermal decomposition of carbon monoxide on iron substrate," *Journal of Physical Chemistry(Moscow)*, vol. 26, pp. 88-95, 1952.
[18] A. V. Melechko, V. I. Merkulov, T. E. McKnight, M. Guillorn, K. L. Klein, D. H. Lowndes, and M. L. Simpson, "Vertically aligned carbon nanofibers and related structures: controlled synthesis and directed assembly," *Journal of Applied Physics*, vol. 97, no. 4, pp. 041301, 2005.
[19] S.-U. Kim, and K.-H. Lee, "Carbon nanofiber composites for the electrodes of electrochemical capacitors," *Chemical Physics Letters*, vol. 400, no. 1, pp. 253-257, 2004.
[20] J. Jang, J. Bae, M. Choi, and S.-H. Yoon, "Fabrication and characterization of polyaniline coated carbon nanofiber for supercapacitor," *Carbon*, vol. 43, no. 13, pp. 2730-2736, 2005.
[21] Y. L. Yao, and K. K. Shiu, "A Mediator-Free Bienzyme Amperometric Biosensor Based on Horseradish Peroxidase and Glucose Oxidase Immobilized on Carbon Nanotube Modified Electrode," *Electroanalysis*, vol. 20, no. 19, pp. 2090-2095, 2008.
[22] J. Wang, "Modified electrodes for electrochemical sensors," *Electroanalysis*, vol. 3, no. 4-5, pp. 255-259, 1991.
[23] D. S. Jeykumari, and S. S. Narayanan, "Fabrication of bienzyme nanobiocomposite electrode using functionalized carbon nanotubes for biosensing applications," *Biosensors and Bioelectronics*, vol. 23, no. 11, pp. 1686-1693, 2008.
[24] A. P. Periasamy, Y.-J. Chang, and S.-M. Chen, "Amperometric glucose sensor based on glucose oxidase immobilized on gelatin-multiwalled carbon nanotube modified glassy carbon electrode," *Bioelectrochemistry*, vol. 80, no. 2, pp. 114-120, 2011.
[25] Y.-L. Yao, and K.-K. Shiu, "Direct Electrochemistry of Glucose Oxidase at Carbon Nanotube-gold Colloid Modified Electrode with Poly(diallyldimethylammonium chloride) Coating," *Electroanalysis*, vol. 20, no. 14, pp. 1542-1548, 2008.
[26] Y.-C. Tsai, S.-C. Li, and S.-W. Liao, "Electrodeposition of polypyrrole–multiwalled carbon nanotube–glucose oxidase nanobiocomposite film for the detection of glucose," *Biosensors and Bioelectronics*, vol. 22, no. 4, pp. 495-500, 10/15/, 2006.
[27] S. J. Bao, C. M. Li, J. F. Zang, X. Q. Cui, Y. Qiao, and J. Guo, "New nanostructured TiO2 for direct electrochemistry and glucose sensor applications," *Advanced Functional Materials*, vol. 18, no. 4, pp. 591-599, 2008.
[28] P. Holt-Hindle, S. Nigro, M. Asmussen, and A. Chen, "Amperometric glucose sensor based on platinum–iridium nanomaterials," *Electrochemistry Communications*, vol. 10, no. 10, pp. 1438-1441, 2008.
[29] A. Umar, M. Rahman, A. Al-Hajry, and Y.-B. Hahn, "Enzymatic glucose biosensor based on flower-shaped copper oxide nanostructures composed of thin nanosheets," *Electrochemistry Communications*, vol. 11, no. 2, pp. 278-281, 2009.

[30] Y. Xian, Y. Hu, F. Liu, Y. Xian, H. Wang, and L. Jin, "Glucose biosensor based on Au nanoparticles–conductive polyaniline nanocomposite," *Biosensors and Bioelectronics,* vol. 21, no. 10, pp. 1996-2000, 2006.

[31] J. Yuan, K. Wang, and X. Xia, "Highly Ordered Platinum-Nanotubule Arrays for Amperometric Glucose Sensing," *Advanced Functional Materials,* vol. 15, no. 5, pp. 803-809, 2005.

[32] J. Zang, C. M. Li, X. Cui, J. Wang, X. Sun, H. Dong, and C. Q. Sun, "Tailoring zinc oxide nanowires for high performance amperometric glucose sensor," *Electroanalysis,* vol. 19, no. 9, pp. 1008-1014, 2007.

[33] Z. Zhuang, X. Su, H. Yuan, Q. Sun, D. Xiao, and M. M. Choi, "An improved sensitivity non-enzymatic glucose sensor based on a CuO nanowire modified Cu electrode," *Analyst,* vol. 133, no. 1, pp. 126-132, 2008.

[34] K. A. Al Mamun, F. S. Tulip, K. MacArthur, N. McFarlane, S. K. Islam, and D. Hensley, "Vertically Aligned Carbon Nanofiber based Biosensor Platform for Glucose Sensor," *International Journal of High Speed Electronics and Systems,* vol. 23, no. 01n02, 2014.

[35] A. B. Islam, F. S. Tulip, S. K. Islam, T. Rahman, and K. C. MacArthur, "A Mediator Free Amperometric Bienzymatic Glucose Biosensor Using Vertically Aligned Carbon Nanofibers (VACNFs)," *IEEE Sensors Journal,* vol. 11, no. 11, pp. 2798-2804, 2011.

[36] M. L. Weeks, T. Rahman, P. D. Frymier, S. K. Islam, and T. E. McKnight, "A reagentless enzymatic amperometric biosensor using vertically aligned carbon nanofibers (VACNF)," *Sensors and Actuators B: Chemical,* vol. 133, no. 1, pp. 53-59, 2008.

[37] C. P. Deck, and K. Vecchio, "Prediction of carbon nanotube growth success by the analysis of carbon–catalyst binary phase diagrams," *Carbon,* vol. 44, no. 2, pp. 267-275, 2006.

[38] R. L. Vander Wal, T. M. Ticich, and V. E. Curtis, "Substrate–support interactions in metal-catalyzed carbon nanofiber growth," *Carbon,* vol. 39, no. 15, pp. 2277-2289, 2001.

[39] M. Guillorn, T. McKnight, A. Melechko, V. Merkulov, P. Britt, D. Austin, D. Lowndes, and M. Simpson, "Individually addressable vertically aligned carbon nanofiber-based electrochemical probes," *Journal of Applied Physics,* vol. 91, no. 6, pp. 3824-3828, 2002.

[40] G. A. Mabbott, "An introduction to cyclic voltammetry," *Journal of Chemical education,* vol. 60, no. 9, pp. 697, 1983.

[41] S. Fletcher, "Tables of Degenerate Electrical Networks for Use in the Equivalent-Circuit Analysis of Electrochemical Systems," *Journal of The Electrochemical Society,* vol. 141, no. 7, pp. 1823-1826, 1994.

[42] T. E. McKnight, A. V. Melechko, D. W. Austin, T. Sims, M. A. Guillorn, and M. L. Simpson, "Microarrays of vertically-aligned carbon nanofiber electrodes in an open fluidic channel," *The Journal of Physical Chemistry B,* vol. 108, no. 22, pp. 7115-7125, 2004.

[43] K. A. Al Mamun, F. S. Tulip, K. MacArthur, N. McFarlane, S. K. Islam, D. Hensley, and I. I. Kravchenko, "A robust VACNF platform for electrochemical biosensor." *IEEE Sensors conference*, pp. 1-4, 2013.

[44] S. Siddiqui, P. U. Arumugam, H. Chen, J. Li, and M. Meyyappan, "Characterization of carbon nanofiber electrode arrays using electrochemical impedance spectroscopy: effect of scaling down electrode size," *ACS Nano,* vol. 4, no. 2, pp. 955-961, 2010.

[45] P. Joshi, L. Zhang, Q. Chen, D. Galipeau, H. Fong, and Q. Qiao, "Electrospun carbon nanofibers as low-cost counter electrode for dye-sensitized solar cells," *ACS Applied Materials & Interfaces,* vol. 2, no. 12, pp. 3572-3577, 2010.

[46] G. Instruments. "Basics of electrochemical impedance spectroscopy."

[47] R. De Boer, and A. Van Oosterom, "Electrical properties of platinum electrodes: impedance measurements and time-domain analysis," *Medical and Biological Engineering and Computing,* vol. 16, no. 1, pp. 1-10, 1978.

[48] T. Ruzgas, L. Gorton, J. Emnéus, and G. Marko-Varga, "Kinetic models of horseradish peroxidase action on a graphite electrode," *Journal of Electroanalytical Chemistry,* vol. 391, no. 1, pp. 41-49, 1995.

[49] Y. Lin, F. Lu, Y. Tu, and Z. Ren, "Glucose biosensors based on carbon nanotube nanoelectrode ensembles," *Nano letters,* vol. 4, no. 2, pp. 191-195, 2004.

[50] X. Lu, Q. Zhang, L. Zhang, and J. Li, "Direct electron transfer of horseradish peroxidase and its biosensor based on chitosan and room temperature ionic liquid," *Electrochemistry Communications,* vol. 8, no. 5, pp. 874-878, 2006.

[51] K. C. MacArthur, F. S. Tulip, K. Mamun, N. McFarlane, and S. K. Islam, "Fabrication and characterization of vertically aligned carbon nanofibers as a biosensor platform for hypoglycemia." *Lester Eastman Conference on High Performance Devices,* pp.1-4, 2012.

[52] R. Behzad, "Design of analog CMOS integrated circuits," *International Edition*, 2001.

[53] G. Ferrari, F. Gozzini, and M. Sampietro, "A current-sensitive front-end amplifier for nano-biosensors with a 2MHz BW." *IEEE International Solid-State Circuit Conference,* pp. 164-165, 2007.

[54] J. Salvia, P. Lajevardi, M. Hekmat, and B. Murmann, "A 56MΩ CMOS TIA for MEMS applications." *Proceedings of IEEE Custom Integrated Circuits Conference* , pp. 199-202, Sept. 2009.

[55] J. Hu, Y.-B. Kim, and J. Ayers, "A low power 100MΩ CMOS front-end transimpedance amplifier for biosensing applications." *IEEE International Midwest Symposium on Circuits and Systems*, pp. 541-544, 2010.

[56] D. M. Binkley, "Tradeoffs and optimization in analog CMOS design." *Proceedings of International Conference on Mixed Design of Integrated Circuits and Systems*, pp. 47-60, 2007.

[57] K. A. Al Mamun, M. H. U. Habib, and N. McFarlane, "A low-power low-noise transimpedance amplifier for an integrated biosensing platform," Proceedings of *IEEE International Midwest Symposium on Circuits and Systems*, pp. 161-164, 2013.

[58] K. A. Al Mamun, and N. McFarlane, "A CMOS potentiostatic glucose monitoring system for VACNF amperometric biosensors," *IEEE International Symposium on Circuits and Systems,* pp. 477-480, 2015.

[59] M. M. Ahmadi, and G. Jullien, "Current-mirror-based potentiostats for three-electrode amperometric electrochemical sensors," *IEEE Transactions on Circuits and Systems I: Regular Papers,* vol. 56, no. 7, pp. 1339-1348, 2009.

[60] L. Busoni, M. Carla, and L. Lanzi, "A comparison between potentiostatic circuits with grounded work or auxiliary electrode," *Review of Scientific Instruments,* vol. 73, no. 4, pp. 1921-1923, 2002.

[61] H. S. Narula, and J. G. Harris, "A time-based VLSI potentiostat for ion current measurements," *IEEE Sensors Journal,* vol. 6, no. 2, pp. 239-247, 2006.

[62] S. M. Rezaul Hasan, "Stability analysis and novel compensation of a CMOS current-feedback potentiostat circuit for electrochemical sensors," *IEEE Sensors Journal,* vol. 7, no. 5, pp. 814-824, 2007.

[63] S. M. Martin, F. H. Gebara, T. D. Strong, and R. B. Brown, "A fully differential potentiostat," *IEEE Sensors Journal, ,* vol. 9, no. 2, pp. 135-142, 2009.

[64] R. F. Turner, D. Harrison, and H. P. Baltes, "A CMOS potentiostat for amperometric chemical sensors," *IEEE Journal of Solid-State Circuits,* vol. 22, no. 3, pp. 473-478, 1987.

[65] C.-Y. Huang, "Design of a voltammetry potentiostat for biochemical sensors," *Analog Integrated Circuits and Signal Processing,* vol. 67, no. 3, pp. 375-381, 2011.

[66] P.-A. Boutet, and S. Manen, "Low power CMOS potentiostat for three electrodes amperometric chemical sensor," *IEEE Faible Tension Faible Consommation,* pp. 15-18, 2011.

[67] M. Roham, D. P. Daberkow, E. S. Ramsson, D. P. Covey, S. Pakdeeronachit, P. A. Garris, and P. Mohseni, "A wireless IC for wide-range neurochemical monitoring using amperometry and fast-scan cyclic voltammetry," *IEEE Transactions on Biomedical Circuits and Systems,* vol. 2, no. 1, pp. 3-9, 2008.

[68] W.-S. Wang, W.-T. Kuo, H.-Y. Huang, and C.-H. Luo, "Wide dynamic range CMOS potentiostat for amperometric chemical sensor," *Sensors,* vol. 10, no. 3, pp. 1782-1797, 2010.

[69] M. H. Nazari, and R. Genov, "A fully differential CMOS potentiostat," *IEEE International Symposium on Circuits and Systems,* pp. 2177-2180, 2009.

[70] C.-Y. Huang, S.-Y. Zeng, and B.-D. Liu, "Design of a voltammetry potentiostat with wide dynamic current range measurement," *IEEE International Conference on Communications, Circuits and Systems,* vol. 2, pp. 335-338, 2013.

[71] W. Range, "Integrated potentiostat for neurotransmitter sensing," *IEEE Engineering in Medicine and Biology Magazine,* pp. 23, 2005.

[72] A. Gore, S. Chakrabartty, S. Pal, and E. C. Alocilja, "A multichannel femtoampere-sensitivity potentiostat array for biosensing applications," *IEEE Transactions on Circuits and Systems I: Regular Papers,,* vol. 53, no. 11, pp. 2357-2363, 2006.

[73] M. Razzaghpour, S. Rodriguez, E. Alarcon, and A. Rusu, “A highly-accurate low-power CMOS potentiostat for implantable biosensors,” *Proceedings of 2011 IEEE Biomedical Circuits and Systems Conference,* pp. 5-8, 2011.

[74] W.-Y. Chung, A. C. Paglinawan, Y.-H. Wang, and T.-T. Kuo, “A 600 μW readout circuit with potentiostat for amperometric chemical sensors and glucose meter applications,” *IEEE Conference on Electron Devices and Solid-State Circuits*, pp. 1087-1090, 2007.

[75] C. Yang, Y. Huang, B. L. Hassler, R. M. Worden, and A. J. Mason, “Amperometric electrochemical microsystem for a miniaturized protein biosensor array,” *IEEE Transactions on Biomedical Circuits and Systems* vol. 3, no. 3, pp. 160-168, 2009.

[76] K. Murari, M. Stanacevic, G. Cauwenberghs, and N. V. Thakor, “Integrated potentiostat for neurotransmitter sensing,” *IEEE Engineering in Medicine and Biology Magazine,* vol. 24, no. 6, pp. 23-29, 2005.

[77] S. S. Ghoreishizadeh, C. Baj-Rossi, A. Cavallini, S. Carrara, and G. De Micheli, “An integrated control and readout circuit for implantable multi-target electrochemical biosensing,” *IEEE Transactions on Biomedical Circuits and Systems,* vol. 8, no. 6, pp. 891-898, 2014.

[78] J. Kim, and W. Dunbar, “Nanopore-application CMOS potentiostat design with input parasitic compensation,” *Electronics Letters,* vol. 50, no. 8, pp. 578, 2014.

[79] K.-S. Sohn, S.-J. Oh, E.-J. Kim, J.-M. Gim, N.-S. Kim, Y.-S. Kim, and J.-W. Kim, “A Unified Potentiostat for Electrochemical Glucose Sensors,” *Transactions on Electrical and Electronic Materials,* vol. 14, no. 5, pp. 273-277, 2013.

[80] K. Turksoy, E. S. Bayrak, L. Quinn, E. Littlejohn, and A. Cinar, “Multivariable adaptive closed-loop control of an artificial pancreas without meal and activity announcement,” *Diabetes Technology & Therapeutics,* vol. 15, no. 5, pp. 386-400, 2013.

[81] L. Hadjileontiadis, “Wavelet-based enhancement of lung and bowel sounds using fractal dimension thresholding-Part I: Methodology,” *IEEE Transactions on Biomedical Engineering,* vol. 52, no. 6, pp. 1143-1148, 2005.

[82] L. J. Hadjileontiadis, “Wavelet-based enhancement of lung and bowel sounds using fractal dimension thresholding-part II: application results,” *IEEE Transactions on Biomedical Engineering,* vol. 52, no. 6, pp. 1050-1064, 2005.

[83] C. Dimoulas, G. Kalliris, G. Papanikolaou, and A. Kalampakas, “Long-term signal detection, segmentation and summarization using wavelets and fractal dimension: A bioacoustics application in gastrointestinal-motility monitoring,” *Computers in Biology and Medicine,* vol. 37, no. 4, pp. 438-462, 2007.

[84] K. S. Kim, J. H. Seo, S. H. Ryu, M. H. Kim, and C. G. Song, “Estimation algorithm of the bowel motility based on regression analysis of the jitter and shimmer of bowel sounds,” *Computer Methods and Programs in Biomedicine,* vol. 104, no. 3, pp. 426-434, 2011.

[85] R. Ranta, C. Heinrich, V. Louis-Dorr, D. Wolf, and F. Guillemin, "Wavelet-based bowel sounds denoising, segmentation and characterization." *Proceedings of the IEEE Annual International Conference in Engineering in Medicine and Biology Society,* vol. 2, pp. 1903-1906, 2001.

[86] R. Ranta, V. Louis-Dorr, C. Heinrich, D. Wolf, and F. Guillemin, “Digestive activity evaluation by multichannel abdominal sounds analysis,” *IEEE Transactions on Biomedical Engineering*, vol. 57, no. 6, pp. 1507-1519, 2010.

[87] O. Sakata, Y. Suzuki, K. Matsuda, and T. Satake, “Temporal changes in occurrence frequency of bowel sounds both in fasting state and after eating,” *Journal of Artificial Organs*, vol. 16, no. 1, pp. 83-90, 2013.

[88] O. Sakata, Y. Suzuki, K. Matsuda, and T. Satake, “Robust bowel sound recording system for long-term monitoring of digestive activity,” *Journal of Japan Society of Welfare Engineering*, vol. 12, pp. 43-8, 2009.

[89] C. Dimoulas, G. Kalliris, G. Papanikolaou, V. Petridis, and A. Kalampakas, “Bowel-sound pattern analysis using wavelets and neural networks with application to long-term, unsupervised, gastrointestinal motility monitoring,” *Expert Systems with Applications*, vol. 34, no. 1, pp. 26-41, 2008.

[90] N. Henry Jr, N. Paul, and N. McFarlane, "Using bowel sounds to create a forensically-aware insulin pump system." *Usenix Workshop on Health Information Technologies*, 2013.

[91] B. L. Craine, M. Silpa, and C. J. O'Toole, “Computerized auscultation applied to irritable bowel syndrome,” *Digestive Diseases and Sciences*, vol. 44, no. 9, pp. 1887-1892, 1999.

[92] J. Holleman, A. Mishra, C. Diorio, and B. Otis, "A micro-power neural spike detector and feature extractor in. 13μm CMOS." *IEEE Custom Integrated Circuits Conference*, pp. 333-336, 2008.

[93] T. Horiuchi, T. Swindell, D. Sander, and P. Abshier, "A low-power CMOS neural amplifier with amplitude measurements for spike sorting." *IEEE International Symposium on Circuits and Systems*, vol. 4, pp. IV-29-32, 2004.

[94] B. H. Kumar, “A fuzzy expert system design for analysis of body sounds and design of an unique electronic stethoscope (development of HILSA kit),” *Biosensors and Bioelectronics*, vol. 22, no. 6, pp. 1121-1125, 2007.

[95] K. A. Al Mamun, M. H. U. Habib, N. McFarlane, and N. Paul, "A low power integrated bowel sound measurement system," *IEEE International Instrumentation and Measurement Technology Conference International*, pp. 779-783, 2015.

[96] K. A. Al Mamun, and N. McFarlane, “Integrated real time bowel sound detector for artificial pancreas systems,” *Sensing and Bio-Sensing Research*, vol. 7, pp. 84-89, 2016.

[97] K. A. Al Mamun, S.K. Islam, Dale K. Hensley, N. McFarlane , “A Glucose Biosensor Using CMOS Potentiostat and Vertically Aligned Carbon Nanofibers,” *IEEE Transactions on Biomedical Circuits and Systems*, 2016 (Accepted).

[98] Measurment Specialties, "DT Series Elements," MS-5561-C-GARMIN datasheet, Aug. 2014.

[99] Cognimem Technologies, "CM1K Pattern Recognition Chip with 1024 Neurons in Parallel," DS_CM1K datasheet.

VITA

Khandaker A. Al Mamun received the B.Sc. degree in electrical engineering from Bangladesh University of Engineering & Technology, Dhaka, Bangladesh in 2008, and will receive the Ph.D. degree in electrical engineering at the University of Tennessee, Knoxville, USA in 2016.

His research interests include modeling and design of novel microelectronic and optoelectronic devices, microfabrication of nanostructures, low power analog and mixed signal circuit design, sensor ASIC design and system integration.